Device and Material Characterisation of Vertical Cavity Surface Emitting Lasers

Curtis Hentschel

A thesis presented for the degree of

Doctor of Philosophy

December 2022

Abstract

This thesis presents the characterisation of oxide-confined vertical-cavity surface-emitting laser (VCSEL) devices, with circular and elliptical oxide apertures, for miniaturised atomic clock (MAC) applications. The use of elliptical oxide apertures, which doesn't require additional processing steps or electron-beam lithography, as an alternative to surface gratings for polarisation control was investigated. Additionally, the measured power-current, emission wavelength, and beam characteristics of the VCSEL devices were compared to the requirements of the MAC.

2.5 µm diameter circular oxide aperture VCSEL devices met most of the requirements. However, with the epitaxial structure considered in this thesis, the small oxide aperture sizes required to achieve side-mode suppression ratios (SMSR) of 30 dB, resulted in a mean divergence angle of 51.6 ± 0.8°; more than twice the maximum allowed value of 25°. There was also a large variation in the measured orthogonal polarisation suppression ratio (OPSR).

1.5×3.7 µm elliptical oxide aperture VCSEL devices had measured SMSRs that were greater than 30 dB up to 0.5 mW. The mean maximum OPSR was 14.2 ± 0.3 dB, for optical powers between 0.2-0.5 mW, the minimum differed from the maximum by less than 0.4 dB for all the measured devices.

The segmented contact stripe-length method was applied directly on VCSEL material to measure the transverse electric (TE) polarised modal gain spectra, as a function of current density and temperature. The cap thickness was varied to reduce the mirror reflectivity and

suppress lasing in the vertical direction. The TE-polarised modal gain was converted into a material gain by calculating the confinement factor and effective index of the mode. For the structure considered, the threshold material gain was determined to be 1440±140 cm^{-1} at 30 °C. To demonstrate the usefulness of this technique in the optimisation of VCSEL structures, the measured gain-peak wavelength, and its temperature dependence is compared to the lasing wavelength.

Acknowledgements

I would like to thank Prof. Peter Smowton and Dr. Samuel Shutts for their continued supervision and guidance over the past few years. I would like to thank my industrial supervisor Dr. Iwan Davies, and my industrial sponsor IQE plc. for their support in the form of an industrial CASE award. I would also like to thank Dr. John Hadden for always being a friendly and approachable mentor. I would like to thank Dr. Richard Forrest, Josie Travers-Nabialek, and Dr. Dagmar Butkovicova for preparing samples and helping with equipment; Dr. Sara-Jayne Gillgrass for processing samples; and Jack Baker, James Meiklejohn, Dr. Craig Allford, and Dr. David Hayes for various VCSEL related discussions and help with measurements. I would also like to thank Fwoziah, Lydia, Benjamin and the many other current and former members of the optoelectronics group, as well as the wider Physics and Astronomy community at Cardiff, for their support throughout my time here. Finally, I would like to thank Prof. Peter Blood for providing his insights and some very interesting discussions.

Contents

Chapter 1

Introduction

This thesis contains a description of the characterisation of vertical-cavity surface-emitting lasers (VCSELs) for application as the pump source in miniature atomic clocks.

1.1 Motivation

Many applications rely on global navigation satellite systems (GNSS) to provide a precise timing reference. As well as navigation and positioning systems, communication networks often require high synchronisation and are also reliant on GNSS. However, the GNSS timing signal is vulnerable to disruption, and failure over a 5 day period is estimated to cost the UK economy £5.2 billion [1]. The miniaturised atomic clock (MAC) is effectively a compact version of the atomic clocks that are used as the time standard by measurement standards laboratories, but with a timing performance that's two or more orders of magnitude poorer [2]. However, it can maintain an accurate clock signal over several days [2] and has the potential to be mass produced and used in everyday applications, thus providing an alternative timing reference during prolonged GNSS outages.

1.2 Atomic Clocks

To the best of our knowledge, the properties of atoms, including their energy levels, are time and space invariant, making them the ideal frequency standard. Atomic clocks, which operate by tuning to the natural resonances of an atom, can keep time with unparalleled accuracy. There are numerous types of atomic clocks in existence. Microwave atomic clocks generate a clock signal in the microwave regime and are generally based on alkali atoms. They include fountain clocks [3], Cesium (Cs) beam clocks, hydrogen maser clocks, and vapor cell clocks [4]. Of these, fountain clocks, which are currently used to define the International System of Units (SI) second, have the highest performance, with a fractional uncertainty on the order of 10^{-15} [5]. Recent years have also seen significant advances in optical clocks. With uncertainties on the order of 10^{-18}, they can outperform fountain clocks and are eventually expected to replace them as frequency standards [6]. However, many applications do not require atomic clocks with the highest accuracy and stability, and other factors such as the size, cost and power usage can determine their suitability. Commercial atomic clocks are predominantly vapour cell clocks and beam clocks [2].

1.2.1 Vapour Cell Atomic Clocks

Figure 1.1a shows a schematic diagram of a vapour cell atomic clock using Rubidium (Rb). A ^{87}Rb discharge lamp emits light, which is filtered by a cell containing ^{85}Rb. The hyperfine structure of ^{85}Rb differs slightly from ^{87}Rb, such that the longer wavelength hyperfine component of the emission line is more strongly absorbed [7]. The filtered light therefore pumps the ^{87}Rb, contained in a reference vapour cell, to the upper energy hyperfine ground state, as shown in figure 1.1b. The reference vapour cell is placed in a microwave cavity, that's modulated at the ground state hyperfine frequency of 6.8 GHz to induce transitions between the hyperfine ground states [2]. This reduces the population difference between the hyperfine ground states, increasing the absorption. The transmission is monitored by a photodiode and used to lock

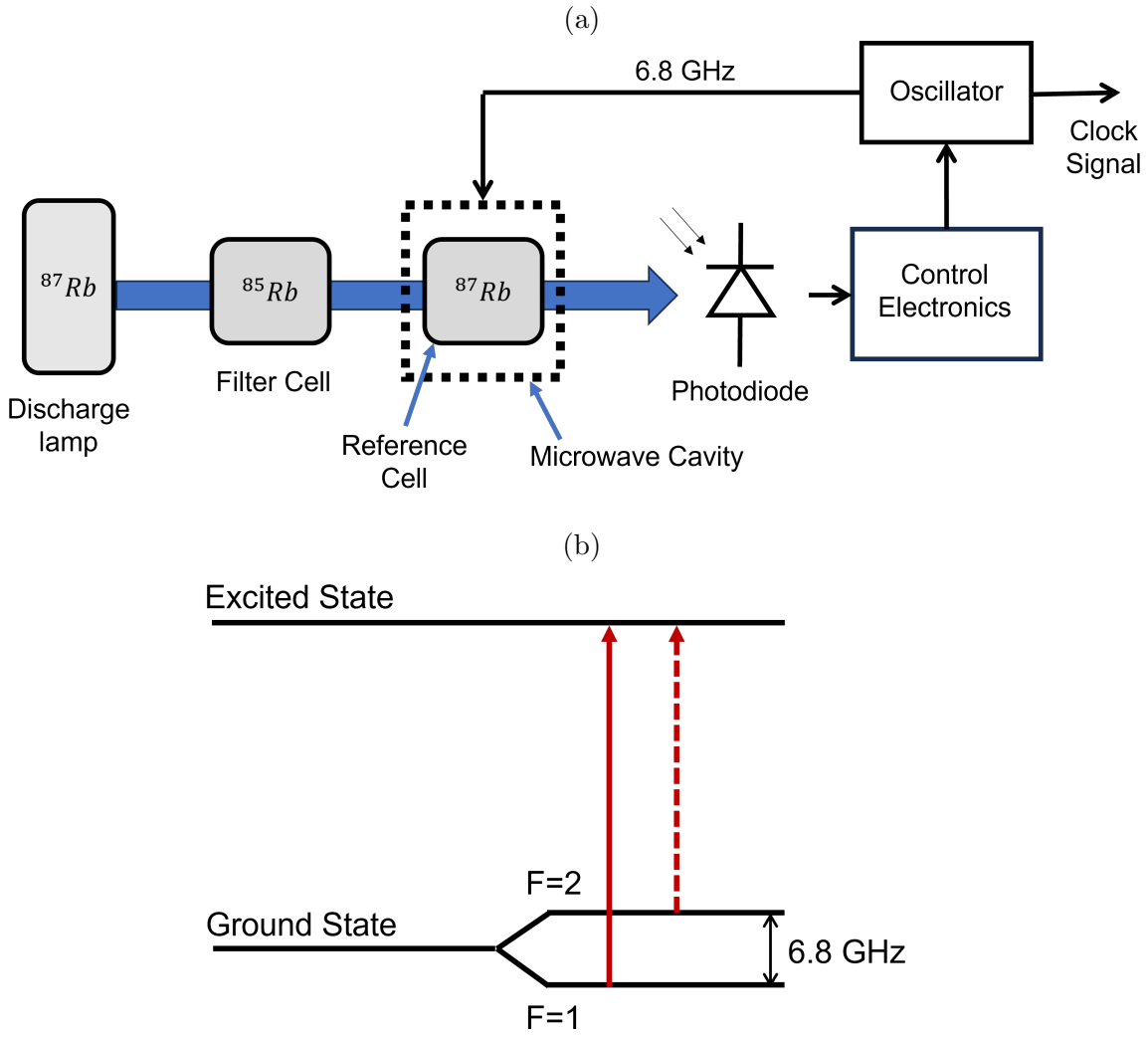

Figure 1.1: (a) Schematic diagram of a vapour cell atomic clock using Rubidium and (b) simplified diagram showing the ^{87}Rb transitions in the reference cell due to the optical emission from the discharge lamp. The solid red arrow shows excitation of the ^{87}Rb atoms from the F=1 ground state to an excited state. The dashed red arrow shows an emission line that is absorbed by the ^{85}Rb filter cell. This leads to an increased population of Rb in the F=2 ground state.

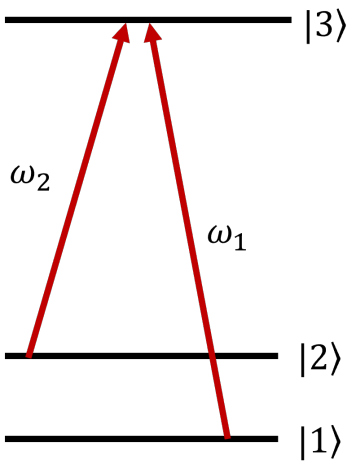

Figure 1.2: Energy level diagram showing states in a Λ configuration, which consists of the two ground states $|1\rangle$ and $|1\rangle$, and the excited state $|3\rangle$. The ground states, $|1\rangle$ and $|1\rangle$, are coupled to state $|3\rangle$ by an optical field with frequencies ω_1 and ω_2, respectively.

the microwave modulation frequency to the ground state hyperfine frequency to generate a clock signal.

With the above implementation of vapour cell atomic clocks, the use of the microwave cavity makes further miniaturisation difficult. Additionally, discharge lamps have a relatively high-power consumption. Miniaturised atomic clocks tend to be compact versions of vapour cell atomic clocks that use laser diodes and are based on coherent population trapping (CPT) which does not require a microwave cavity [2].

1.2.2 Coherent Population Trapping Spectroscopy

CPT can occur when atoms are optically pumped by two coherent beams that meet certain resonance conditions. Figure 1.2 shows a three-level system in a Λ configuration, which consists of two ground states, labelled $|1\rangle$ and $|2\rangle$, and a single excited state $|3\rangle$. The frequency separation between the $|1\rangle$ and $|3\rangle$, and the $|2\rangle$ and $|3\rangle$ states, are ω_1 and ω_2, respectively. Two orthogonal states, known as a dark state and a bright state, can be formed from a superposition of the $|1\rangle$ and $|2\rangle$ states. Under illumination by two coherent optical fields, with frequencies of ω_1 and ω_2, an atom in the bright state can be excited into the $|3\rangle$ state. Eventually, the excited

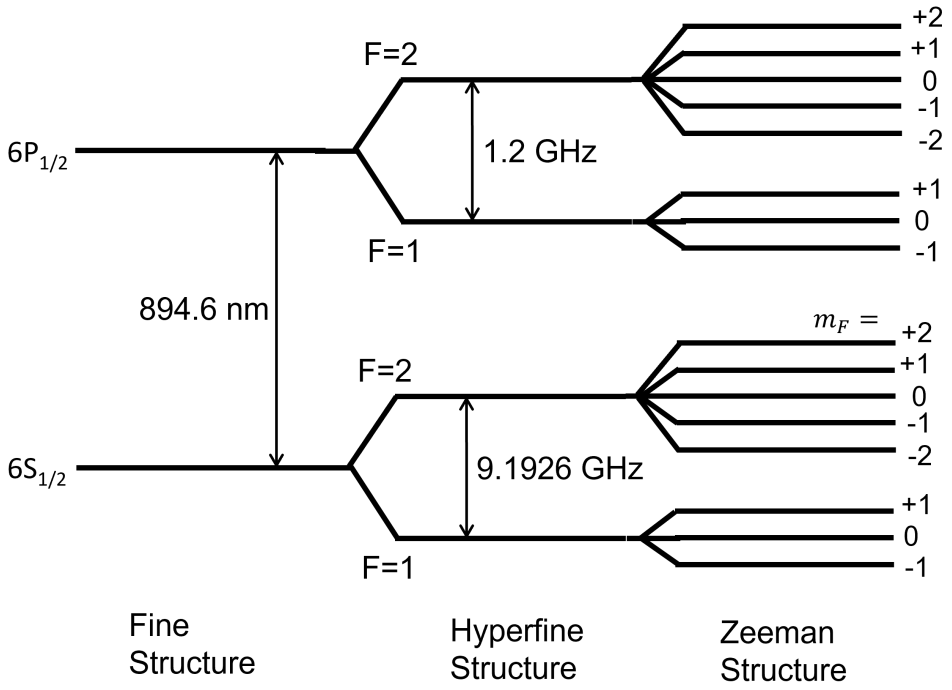

Figure 1.3: Energy level diagram of the Cs D1 transition, which occurs between the $6S_{1/2}$ and $6P_{1/2}$ states. Shown are the fine structure, hyperfine structure, and the Zeeman structure, which is the splitting of the hyperfine levels under a weak magnetic field. The hyperfine and Zeeman levels are labelled with the quantum number, F, that parameterises the coupling of the total orbital angular momentum with the nuclear spin, and its projection, m_F, respectively. The transition wavelength of the Cs D1 transition is 894.6 nm. The hyperfine splitting of the $6S_{1/2}$ and $6P_{1/2}$ states are 9.1926 GHz and 1.2 GHz, respectively.

state atom will relax into either the dark or bright state via spontaneous emission [4][8]. On the other hand, atoms in the dark state do not interact with the coherent optical fields and are effectively trapped in this state [4][8]. Atoms accumulate into this dark state, which leads to a reduction in the absorption .

1.2.3 Miniaturised Atomic Clocks

The VCSELs in this thesis have been designed for MACs that are based on CPT using the Cs D1 transition. Figure 1.3 shows an energy level diagram for the D1 transition, which involve the $6S_{1/2}$ and $6P_{1/2}$ states and has a transition wavelength of 894.6 nm. The hyperfine levels of the $6S_{1/2}$ ground state has a frequency splitting of 9.2 GHz, while the $6P_{1/2}$ excited state has a hyperfine frequency splitting of 1.2 GHz [9].

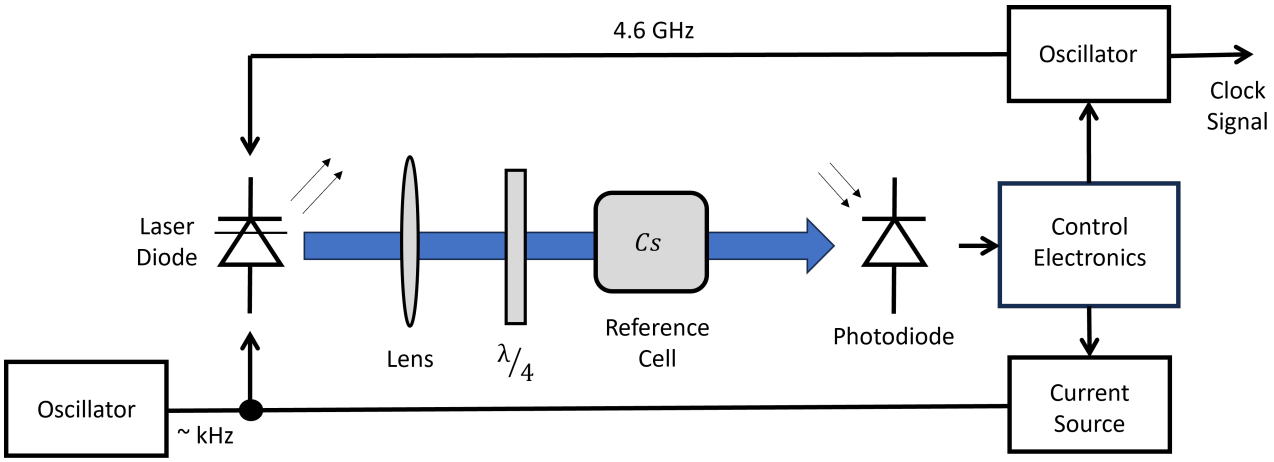

Figure 1.4: Schematic diagram of a miniaturised atomic clock based on coherent population trapping. A laser diode is modulated at 4.6 GHz, half the Cs $6S_{1/2}$ hyperfine splitting frequency of 9.2 GHz, and used to interrogate Cs atoms in a reference cell. The transmission through the cell is monitored by a photodiode, and used to stabilise the RF modulation to generate a stable and accurate clock signal. A low frequency modulation of several kHz is also applied to lock the lasing wavelength to the D1 transition.

The three level Λ system can be formed from the $6S_{1/2}$ $|F = 1, m_F = 0\rangle$ and $|F = 2, m_F = 0\rangle$ ground states, with the $6P_{1/2}$ $|F = 1, m_F = 1\rangle$ excited state; or the $6P_{1/2}$ $|F = 1, m_F = 0\rangle$ and $|F = 2, m_F = 0\rangle$ ground states, with the $6P_{1/2}$ $|F = 2, m_F = 1\rangle$ excited state. The selection rules are such that both ΔF and Δm_F cannot be zero [10]. Therefore, circularly polarised light is necessary to couple the magnetic field insensitive, $m_F = 0$, ground states to the excited state [11].

Figure 1.4, shows a simple schematic diagram of a CPT clock utilising the Cs D1 transition. The linearly polarised emission, of a diode laser. is converted into circularly polarised light, by a quarter waveplate, and used to interrogate Cs atoms contained in a heated reference cell. The diode laser is directly modulated, generating coherent sidebands. When the modulation frequency is half the Cs $6S_{1/2}$ hyperfine splitting frequency [4], the first order sidebands pump the Cs atoms into the dark state. The increased transmission due to CPT is detected by a photodiode and used to stabilise the modulation frequency to generate a 4.6 GHz clock signal. To lock the lasing wavelength to the Cs D1 transition, an additional low frequency modulation, on the order of several kHz, is applied to the laser, causing the emission wavelength

to dither around the transition wavelength. The transmission is detected and used to generate a locking signal.

1.3 The VCSEL

Recent years have seen significant growth in the VCSEL market, particularly sensing applications. Due to their short cavity, compared to standard edge emitting lasers, VCSELs have a narrow emission spectrum and temperature-stable emission wavelength, which enables the use of a narrow-band filter on the detector to improve the signal to noise ratio [12][13]. Additionally, their surface emission make VCSELs ideal for fabricating large arrays, and their low beam divergence allow the use of simple optics, and systems can be made compact [13][14].

VCSELs are also an attractive choice for MACs. A single device can have sub-mA lasing threshold currents due their small active volume, so power consumption can be on the order of 1 mW, especially since high optical powers are not required. The short, single longitudinal mode cavity of VCSELs ensures operation free of mode-hops which cause the lasing wavelength to go out of resonance with the atomic transition and leads to a loss of signal [15]. Additionally, VCSELs can be directly modulated at GHz frequencies, at relatively low optical powers, due to the short photon lifetimes and high photon density within its cavity, as well as a low capacitance owning to its small area. The MAC application places particularly stringent requirements on the VCSEL device that must be met [2][16][17][18]. The specification for the VCSELs in this thesis is summarised in table 1.1.

A single optical frequency, resonant with the D1 transition of Cs is required, so the VCSEL emission must be single mode, with a wavelength of 894.6 nm [2]. A current dependent wavelength tunability provides a way to stabilise the VCSEL to the atomic transition by applying a low frequency current modulation. However, this method of laser frequency stabilisation also places limits on the slope efficiency. A high slope efficiency can shift the position of the optical power minima when the current, and thus wavelength, is swept. A stable linearly polarised

Parameter (units)	Min	Target	Max
Operating Current (mA)	1	2	6
Output Power (mW)	0.2	0.5	
Slope Efficiency (W/A)		0.2	0.4
Emission Wavelength (nm)		894.6	
Current Tuning Coefficient (nm/mA)		0.6	
SMSR (dB)	30	40	
Full-Width Beam Divergence (°)		10	25
3 dB Modulation Bandwidth (GHz)	4	5	10
Linewidth (MHz)		50	100

Table 1.1: MAC VCSEL Specification

optical output enables conversion into circularly polarised light with a quarter-waveplate [16]. Additionally, mode competition between orthogonally polarised modes can cause the VCSEL optical power to fluctuate and introduce additional noise [19]. A low divergence angle simplifies the optics used. The VCSEL must be directly modulated at 4.6 GHz, and a 3 dB bandwidth that's greater than 4 GHz ensures efficient conversion of radio frequency (RF) power into modulation of the VCSEL output. Since absorption by the Cs atoms is wavelength dependent, frequency noise in the VCSEL optical output will be converted to amplitude noise and degrade the CPT signal. Therefore, to minimise additional amplitude noise, the linewidth should be below 100 MHz [9]. Finally, due to their close proximity to the Cs vapour cell, the VCSEL must be operated at a temperature close to the cell temperature of 70 °C.

One of the challenges of using VCSELs is that due to their circular symmetry there is no strong mechanism to fix the polarisation along a particular direction, and the polarision may switch during operation [20]. Sub-micron surface gratings have been used to produce VCSEL devices that are linearly polarised, with no polarisation switching, at a wavelength of 894.6 nm [21][22][23]. However, additional processing steps are required to fabricate the surface grating, and electron-beam lithography is necessary due to the small feature-size [20]. On the other hand, non-circular oxide apertures do not require additional processing steps, and have the potential to produce polarisation stable VCSEL devices [24][25][26].

To ensure the desired specifications are met, the VCSEL epitaxial structure must be tested

and verified. This can be achieved with growth calibrations such as cavity-resonance reflectance and room temperature photoluminescence measurements, combined with the wafer-level testing of fabricated full VCSEL structures, to obtain laser output characteristics. Making the appropriate changes to the epitaxial structure to optimise device performance is challenging. For example, for efficient operation, with a low threshold current, the gain-peak and the cavity resonance wavelength should coincide. This is complicated since each of these parameters has a different temperature dependence. A full understanding of how the optical gain spectrum varies with temperature and current density would enable more rapid optimization at lower cost.

1.4 Previous Work

1.4.1 VCSELs for miniaturised atomic clocks

There have been a number of reports of VCSELs designed to emit at 894.6nm for MAC applications within the literature.

The impact of detuning the gain-peak and the cavity resonance wavelength was studied in [18]. A 3.5 µm active diameter oxide-confined VCSEL, operating at 70 °C, with a threshold current of 0.23 mA and an output power of approximately 1.7 mW at 4 mA was demonstrated. A side-mode suppresion ratio (SMSR) that was greater than 25 dB was achieved for temperatures of 23-110 °C, for a drive current of 1 mA.

In [27], a VCSEL device with a 3 µm diameter surface relief and a 7 µm diameter oxide aperture, achieved a 30 dB single-mode optical power of 0.45 mW at 80 °C, and had a threshold current of 1.94 mA.

The characteristics of normal and inverted surface grating VCSELs were presented in [17][21][22][23]. A 3 µm active diameter, normal grating VCSEL, with a 0.7 µm grating period, operating at 80 °C, was reported in [21] to have a threshold current of 0.2 mA and a maximum output power of approximately 0.55 mW. The average orthogonal polarisation suppression ratio

(OPSR) was 19 dB and an SMSR of 42 dB was measured at 1.8 mA. In [17], a 3.5 µm active diameter, inverted grating, VCSEL device, with a 0.6 µm grating period, was reported to have a full-width at half-maximum (FWHM) divergence angle of 9.6°.

VCSELs that featured a composite cavity, where a low-Q cavity was surrounded by a high-Q cavity, and intra-cavity contacts to reduce optical losses and obtain narrow linewidths was reported in [28]. At 90 °C, an OPSR greater than 15 dB, and an SMSR greater than 35 dB, was measured for a device with a 2.5 µm major diameter rhomboidal oxide aperture with an aspect ratio of 0.8-0.85. The device also had a threshold current of approximately 0.7 mA, and a slope efficiency greater than 0.5 W/A. At 70 °C, the linewidth at 2 mA was 60 MHz.

Triangular holes were etched onto the surface of a VCSEL device to obtain a farfield beam divergemce of approximately 10° and a SMSR of 20 dB [29]. The threshold current was 1 mA, with a maximum optical power of 0.86 mW.

VCSEL devices have also been developed by Sandia National Laboratories, for use in their chip-scale MAC systems [9]. The reported device had a 0.3 mA threshold current, and showed 35 dB single-mode operation with an optical power of approximately 0.4 mW, at an operating current of 1 mA.

Commercially available 894.6 nm emitting VCSELs have also been produced by Vixar inc. [30][31]. The typical characteristics of a device designed for operation at 80 °C and 1.4 mA include a 0.61 mA threshold current, 0.3 mW output power, 0.37 W/A slope efficiency, 20 dB SMSR, and a polarisation extiction ratio of 15 dB.

1.4.2 Gain Characterisation of VCSEL Material

The performance and the manufacturing of VCSELs for application in MACs can likely be improved further through a combination of detailed characterisation and device design. One of the most important parameters to understand is the gain available in a VCSEL.

In semiconductor lasers, the active layers are where the carriers can recombine to generate optical gain. For VCSEL structures, the gain characterisation of the active layers is not as straightforward when compared to their edge emitting counterparts. Single-pass transmission measurements are difficult to apply in the vertical direction, due to the highly reflective distributed Bragg reflectors (DBR) which form the vertical cavity. The Hakki-Paoli technique [32] has been applied in the vertical direction on a 24.5-λ cavity VCSEL [33]. However, this is not possible with few-λ cavity VCSEL structures, which are more widely used, due to their large free spectral range on the order of the optical gain bandwidth. As detailed in section 2.9, the external quantum efficiency depends on the internal optical loss and the mirror loss. If the injection efficiency and the mirror loss is known, the internal optical loss and therefore the threshold gain can be determined from the slope efficiency. The gain-current relation for VCSELs have been determined from measurements of the external quantum efficiency and threshold current, with losses varied by changing the feedback from an external mirror [34], or by changing the internal optical loss by fabricating different area devices [35][36].

It is also possible to measure the gain through the in-plane propagation of light. Test wafers with a nominally identical active region but without the Bragg reflectors can be grown [37][38]. However, there may be differences in the injection efficiency, and is less useful than testing on the very same structure and wafer used for fully operational VCSEL devices.

Despite being designed for vertical emission, the in-plane propagation of light in VCSEL material is possible [39][40][41][42]. In many cases, the separate confinement heterostructure (SCH) effectively forms a multi-layer slab waveguide so that the in-plane mode can propagate with low optical loss [40][41]. In-plane gain measurement techniques can therefore be applied directly on VCSEL material. External efficiency measurements on different length stripe lasers fabricated from VCSEL material have been used to determine the peak-gain current density curve [41]. The in-plane Hakki-Paoli method has also been applied on VCSEL material, although carrier pinning limited the measured gain spectra to sub-threshold current densities [42],

1.5 Thesis Structure

The aim of this PhD is to characterise oxide-confined VCSELs to determine the optimum oxide aperture to not only meet the requirements of the MAC application, but ensure it is tolerant to fabrication variations. Additionally, a technique to characterise the active layers of the VCSELs is investigated, so that design changes to the epitaxial structure can be better informed.

Chapter 2 covers the key terms and concepts covered within this thesis. Chapter 3 describes the experimental setups and techniques used in this thesis. In chapter 4, the device characteristics of oxide-confined VCSELs designed to emit at 894.6 nm are presented. The effect of the oxide aperture dimension on the optical power, wavelength, beam profile is shown and the optimum dimension that meets the specification is discussed. Chapter 5 presents segmented contact measurements that were performed on VCSEL material. Chapter 6 summarises the key results of this thesis and suggests future work.

Chapter 2

VCSEL Fundamentals

This chapter reviews the key terms and concepts that are covered in this thesis.

2.1 Electronic States in a Semiconductor

The key features of the electronic states of a semiconductor crystal arise from its periodic structure. Bloch's Theorem states that solutions to the Schrodinger equation, with a periodic potential, have wavefunctions of the form

$$u(\vec{k}, \vec{r})e^{\vec{k}\cdot\vec{r}} \tag{2.1}$$

where $\vec{r}$ is the position, $\vec{k}$ is the wavevector of the electron and is related to its momentum, and $u(\vec{k}, \vec{r})$ is a Bloch function which has the same translational symmetry as the crystal lattice [43]. Bloch's theorem tells us that the electron wavefunction can be described by a plane wave which is modulated by the periodic potential of the ions on the crystal lattice.

Figure 2.1 shows a simplified diagram of the electronic band structure of a direct gap semiconductor. The highest energy bands that are almost fully occupied in thermal equilibrium are known as the valence (V) band and include the light-hole (LH), heavy-hole (HH), and split-off (SO)

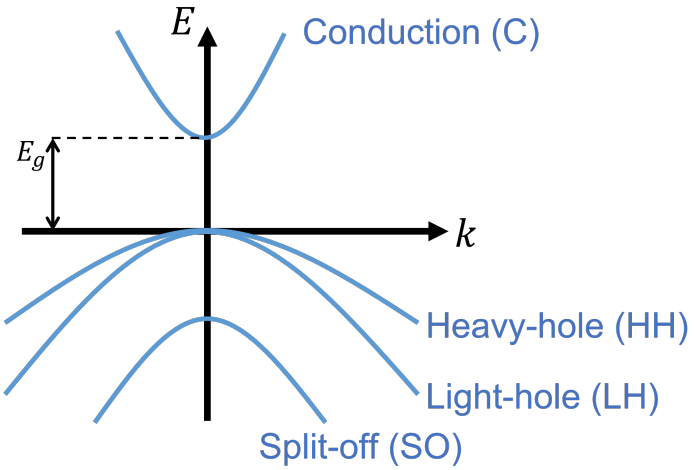

Figure 2.1: A simplified diagram of the electronic band structure, which describes the allowed electron energies, E, as a function of its wavevector, k. Shown are the conduction band and the three valence bands - the heavy-hole, light-hole, and split-off band. The energy difference between the conduction and valence band edge is known as the band gap energy, E_g.

band. The LH and HH bands are usually degenerate at the band-edge, although the degeneracy can be broken by strain or by confinement (e.g in a quantum well (QW)) [44][43]. The next highest energy band is known as the conduction (C) band. The energy difference, E_g, between the edge of the conduction and valence band is known as the band gap energy.

An electron in the valence band can be excited into the conduction band, where it is able to conduct. This leaves behind a vacant state in the valence band known as a hole. Holes are also mobile and carry a positive charge. The complicated interaction of electrons and holes with the crystal lattice can be described using the concept of an effective mass m^*

$$\frac{1}{m^*} = \frac{1}{\hbar^2}\frac{d^2E}{dk^2} \tag{2.2}$$

Under the parabolic band approximation, the effective mass is treated as being constant with the wavevector. This is typically a reasonable approximation to make close to the band edge. Additionally, in most semiconductors, the band structure is anisotropic so that the curvature will be different along different directions in k-space. This means the effective mass will differ depending on the direction.

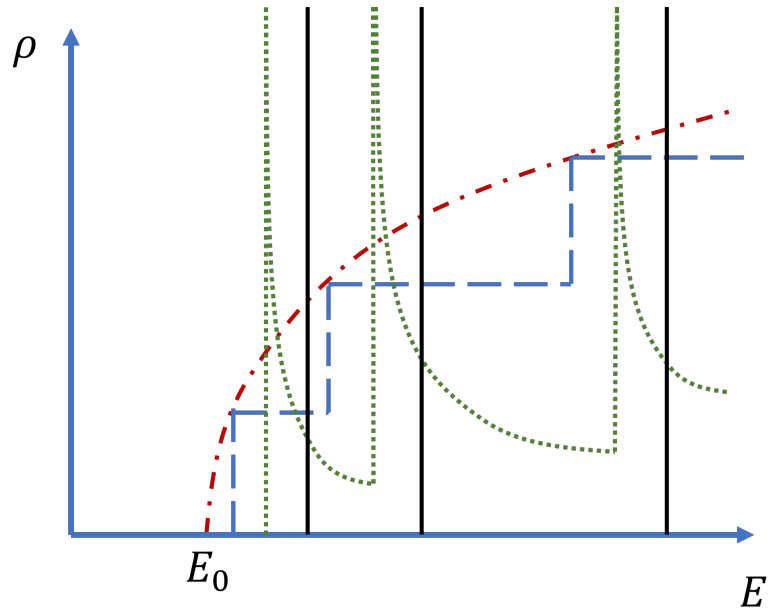

Figure 2.2: The density of states, ρ, as a function of energy, E, for 3 (red dots and dashes), 2 (blue dashes), 1 (green dots), and 0 (black solid) dimensional semiconductors. E_0 is the band-edge energy.

The density of states, ρ, describes the number of modes at a given energy, E, per unit volume. Figure 2.2 shows the density of states as a function of energy for different dimensional materials.

For a bulk semiconductor, the three dimensional density of states is given by

$$\rho_{3\mathrm{D}}(E) = \frac{1}{2\pi^2}\left(\frac{2m^*}{\hbar^2}\right)^{\frac{3}{2}}(E - E_0)^{\frac{1}{2}} \tag{2.3}$$

where E_0 is the band-edge energy.

For a quantum well, the k-vector along the confined direction becomes quantised, so that the conduction and valence bands are split into sub-bands, and the density of states become step-like. The two dimensional density of states for a single sub-band is given by

$$\rho_{2\mathrm{D}}(E) = \frac{m^*}{\pi\hbar^2 d_{\mathrm{QW}}}\Theta(E - E_{\mathrm{n}}) \tag{2.4}$$

where d_{QW} is the width of the quantum well, E_{n} is the band-edge energy for a particular sub-band, and $\Theta(...)$ is the Heaviside step function.

For a quantum wire, carriers are confined along two of the dimensions (in this case, along the x and y direction). The one dimensional density of states is given by

$$\rho_{1\mathrm{D}}(E) = \frac{2}{\pi d_x d_y}\left(\frac{2m^*}{\hbar^2}\right)^{\frac{1}{2}}(E - E_n)^{-\frac{1}{2}} \tag{2.5}$$

where d_x and d_y are the width of the wires.

For a quantum dot, carriers are confined along all dimensions, and the zero dimensional density of states is given by

$$\rho_{0\mathrm{D}}(E) = 2\delta(E - E_n) \tag{2.6}$$

where $\delta(...)$ is the delta function.

2.2 Carrier Distribution

In thermal equilibrium, the probability distribution of electron occupation follows the Fermi-distribution given by

$$f(E) = \frac{1}{1 + e^{\frac{(E-E_\mathrm{F})}{k_\mathrm{b}T}}} \tag{2.7}$$

where E_F is the Fermi energy, E is the energy of the state, k_b is the Boltzman constant and T is the temperature. The function gives the occupation probability of an electron at a particular state with energy E. The Fermi energy is defined as the energy where the occupation probability is 50% and is determined by the carrier density. Holes are unoccupied electron states, so its probability distribution is given by $1 - f(E)$. In certain situations, such as under electrical injection, the system will not be in thermal equilibrium. The distribution in quasi-equilibrium can be described using separate Fermi energies for the electrons and holes.

2.3 Optical Gain

Optical gain occurs through a process known as stimulated recombination. An incident photon with a particular energy interacts with an excited state, inducing a transition to a lower state that emits a photon with the same energy and phase. In a bulk semiconductor and along the plane of quantum wells, transitions occur between states with the same wavevector due to momentum conservation. This is known as the k-selection rule [43]. The optical gain at a particular photon energy $\hbar\omega$ is given by

$$g(\hbar\omega) = |M_{\mathrm{T}}|^2 \rho_{\mathrm{r}}(\hbar\omega) \left[f_2(E_2(\hbar\omega)) - f_1(E_1(\hbar\omega)) \right] \tag{2.8}$$

where $E_2(\hbar\omega)$ and $E_1(\hbar\omega)$ are the electron and hole energies, respectively, for a given transition energy. $|M_{\mathrm{T}}|^2$ is the transition matrix element defined below in section 2.3.1. $\rho_{\mathrm{r}}(\hbar\omega)$ is the reduced density of states and gives the density of transition pairs at a given transition energy. Assuming the k-selection rule, ρ_{r} for transitions between a valence band and the conduction band can be expressed in terms of the conduction band, ρ_{c}, and valence band, ρ_{v}, density of states

$$\frac{1}{\rho_{\mathrm{r}}(\hbar\omega)} = \frac{1}{\rho_{\mathrm{c}}(E_2(\hbar\omega))} + \frac{1}{\rho_{\mathrm{v}}(E_1(\hbar\omega))} \tag{2.9}$$

2.3.1 Transition Matrix Element

The transition matrix element $|M_{\mathrm{T}}|^2$ describes the strength of the interaction of the field with the states involved in the transition [43].

$$|M_{\mathrm{T}}|^2 = |\langle u_{\mathrm{c}} | \hat{e} \cdot \hat{p} | u_{\mathrm{v}} \rangle|^2 \, |\langle F_2 | F_1 \rangle|^2 \tag{2.10}$$

where $|\langle F_2 | F_1 \rangle|^2$ is the overlap integral of the envelope functions, and for bulk semiconductor, this leads to the k-selection rule. $\hat{e}$ the polarisation direction of the light, and $|\langle u_{\mathrm{c}} | \hat{e} \cdot \hat{p} | u_{\mathrm{v}} \rangle|^2$ is the momentum matrix element. The dependence of the transition matrix element on the

	$\parallel$	$\perp$
C-LH	$1/2$	$2/3$
C-HH	$1/6$	0

Table 2.1: C-LH and C-HH momentum matrix element relative to the bulk momentum matrix element $|M|^2$, for light polarised parallel ($\parallel$) or perpendicular ($\perp$) to the quantum well plane.

electric field polarisation, comes from the symmetry of the valence and conduction band Bloch functions.

In bulk material, there is no preferred direction for the electron wavevector, so that averaging over all directions leads to no polarisation dependence. For a particular polarisation, for both the C-LH and the C-HH transitions, the transition strength is $1/3|M|^2$, where $|M|^2$ is the bulk momentum matrix element [43][44].

In QWs, confinement leads to a non-zero wavevector component along the confined direction, which leads to a polarisation dependence. Depending on whether the light is polarised parallel or perpendicular to the QW plane, the C-LH and C-HH transition strengths are different. Table 2.1 gives transition strengths, at the band edge where there is no valence band mixing, relative to the bulk momentum matrix element [43][44].

2.4 Non-radiative Recombination

Within the gain region, the carriers can recombine radiatively or non-radiatively. Non-radiative recombination processes are detrimental to device performance, as they do not contribute to the optical emission, and instead, facilitate the conversion of energy into heat.

2.4.1 Shockley-Read-Hall Recombination

The presence of defects and impurities in the crystal lattice can produce an electronic state with an energy level that is within the energy gap of the semiconductor. This electronic state is known as a trap state and is localised at the defect or impurity. As shown in figure 2.3, it

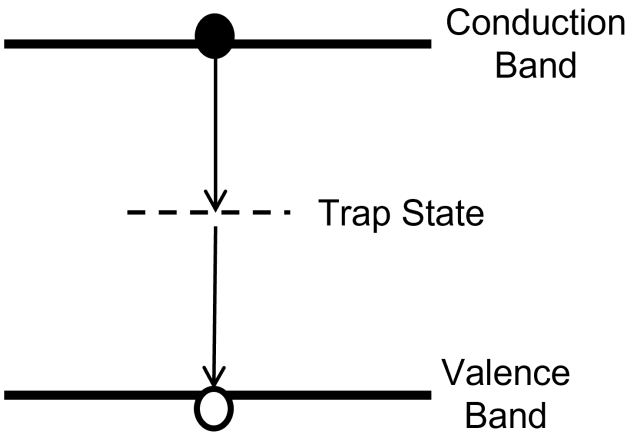

Figure 2.3: Diagram showing the Shockley-Read-Hall recombination pathway. A conduction electron is captured by a trap state located within the energy gap, before being released into the valence band where it recombines with a hole. Energy from the transition is dissipated as heat.

provides a transition pathway where carriers recombine non-radiatively in a process known as Shockley-Read-Hall (SRH) recombination [45][46]. An empty trap state captures an electron from the conduction band before being released into the valence band where it recombines with a hole. Instead of photon emission, energy is transferred to lattice phonons and is dissipated as heat. Trap states that have energy levels close to the centre of the energy gap are known as deep traps, and have particularly high recombination rates.

In the high injection regime, which typically applies to semiconductor lasers, the recombination rate R_{SRH} is given by

$$R_{SRH} = \frac{N}{\tau_p + \tau_n} \tag{2.11}$$

where N is the carrier density, and τ_n and τ_p are the electron and hole SRH recombination lifetimes, respectively. τ_n and τ_p are given by $\frac{1}{c_n N_t}$ and $\frac{1}{c_p N_t}$, respectively, where N_t is the trap density, c_n is the electron capture rate, and c_p is the hole capture rate. The SRH recombination rate increases approximately linearly with carrier concentration and is proportional to the trap density, which is dependent on the quality of the crystal grown. The crystal quality can be very high with modern growth processes, so the SRH recombination rate can be relatively low [43].

2.4.2 Auger Recombination

Auger recombination is an impact ionisation process where the recombination energy of an electron hole pair is transferred to another electron or hole [43]. The excited carrier eventually relaxes, and the energy is dissipated as heat. Figure 2.4 shows three possible Auger recombination process. The CCCH process involves the collision of two conduction electrons, where one electron is excited up the conduction band and the other recombines with a heavy hole. For the CHSH process, a conduction band electron recombines with a heavy hole, and the energy is transferred to an electron in the split-off band, which is excited into the heavy hole band. For the CHLH process, a conduction band electron recombines with a heavy hole, and an electron in the light hole band is excited into the heavy hole band.

The recombination rate is proportional to N^2P for the CCCH process, and proportional to NP^2 for the CHSH and CHLH process. Here, N is the electron density, and P is the hole density. At high injection rates commonly seen in diode lasers, $N \approx P$, and the Auger recombination rate is proportional to N^3 [43]. Auger processes have an associated activation energy due to energy and momentum conservation, and the recombination rate increases exponentially with temperature [43]. The activation energy for the CHSH Auger process is proportional to the energy difference between the bandgap and split-off band energies. Therefore, the CHSH process severely limits the radiative efficiency in materials with a band gap energy comparable to the split-off energy. For the CCCH and CHLH processes, the activation energy is proportional to the bandgap energy, so the recombination rates are high for narrow bandgap material. In wide bandgap materials (below 1 µm), the band-to-band Auger recombination rate is reduced, and instead, phonon assisted Auger recombination, which has lower rates, tends to dominate [44].

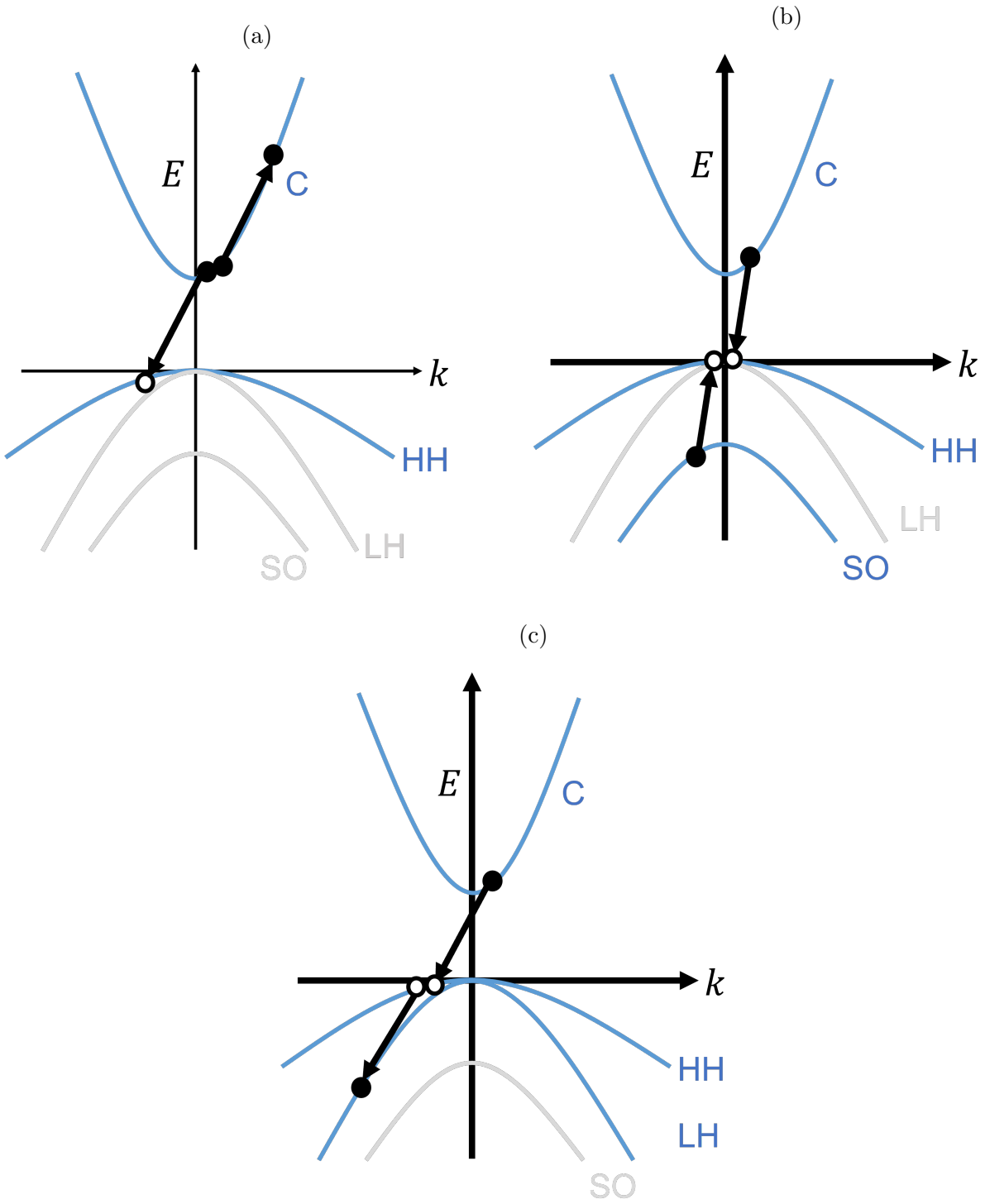

Figure 2.4: Diagram showing three possible Auger recombination process, where (a) the CCCH process involves 3 conduction states and a heavy hole state, (b) the CHSH process involves a conduction state, two heavy hole states, and a split-off state, and (c) the CHLH process involves a conduction state, two heavy hole states, and a light hole state. The conduction (C), heavy hole (HH), light hole (LH), and split-off (SO) are shown. Bands that are relevant to a particular Auger process are blue, while the rest are grey.

2.5 Carrier Injection

Optical gain requires population inversion where the carriers are more likely to be in the conduction band rather than the valence band so that an incident photon is more likely to induce stimulated emission rather than absorption. This cannot occur in thermal equilibrium, but it is possible to move the system away from thermal equilibrium by the electrical or optical injection of carriers.

Diode lasers typically employ a p-i-n diode structure to inject electrons and holes into the conduction and valence band, respectively. A p-i-n structure is formed by sandwiching intrinsic semiconductor material between p-doped and n-doped semiconductor material. The majority carrier population in p-doped semiconductor is holes, while for n-doped semiconductor the majority is electrons. The dopant determines whether a semiconductor becomes p- or n-type. Group IV elements can act as both a donor or acceptor for III-V semiconductors, depending on whether the dopant replaces the group III or V element [47].

Figure 2.5 shows the energy band diagram of an n-doped and p-doped semiconductor of the same material, before (figure 2.5a) and after (figure 2.5b) being combined to form a p-n homojunction. In p-doped semiconductor, the majority carrier population is holes, while for n-doped semiconductor the majority is electrons. The dopant determines whether a semiconductor becomes p- or n-type. Group IV elements can act as both a donor or acceptor for III-V semiconductors, depending on whether the dopant replaces the group III or V element [47]. The Fermi-level is close to the conduction band in the n-doped material and the valence band in the p-doped. Figure 2.5b shows the resulting energy band of an unbiased p-n homojunction, formed by combining the two pieces, under thermal equilibrium. In thermal equilibrium, the Fermi-level is the same for both holes and electrons, and line up across the junction. Electrons and holes recombine at the junction, depleting carriers across a region known as the depletion region, leaving behind negatively and positively charged ions on the p- and n-side, respectively. Due to the charged ions in the depletion region, there is an inbuilt electric

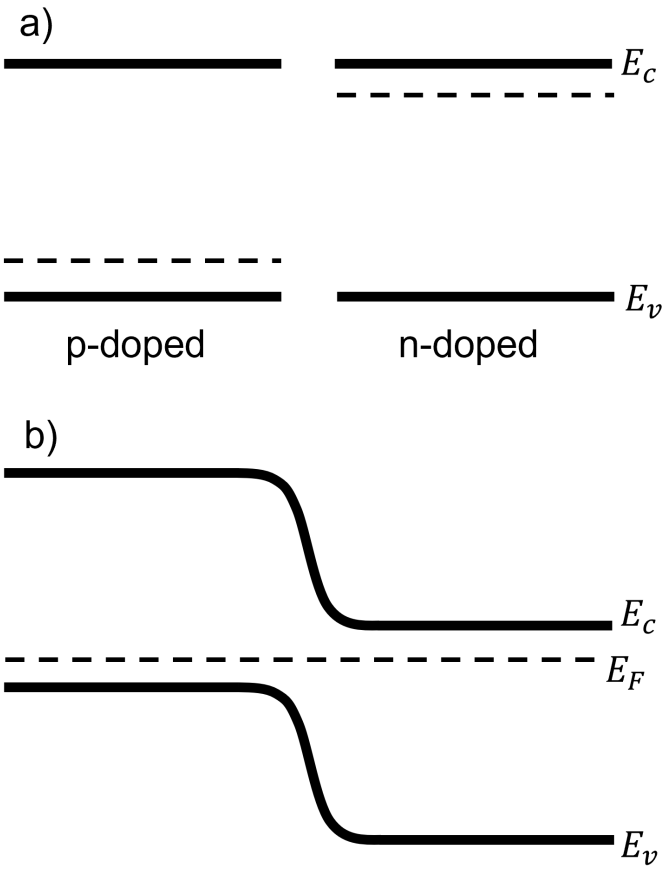

Figure 2.5: Diagram showing the spatial variation of the conduction (E_c) and valence (E_v) band-edge energies, and the Fermi energy (E_F) for (a) spatially separate p- and n-doped semiconductor of the same species, and (b) the resulting unbiased p-n homojunction that forms after combining the two. The solid lines show the band-edge, while the dashed lines show the Fermi level.

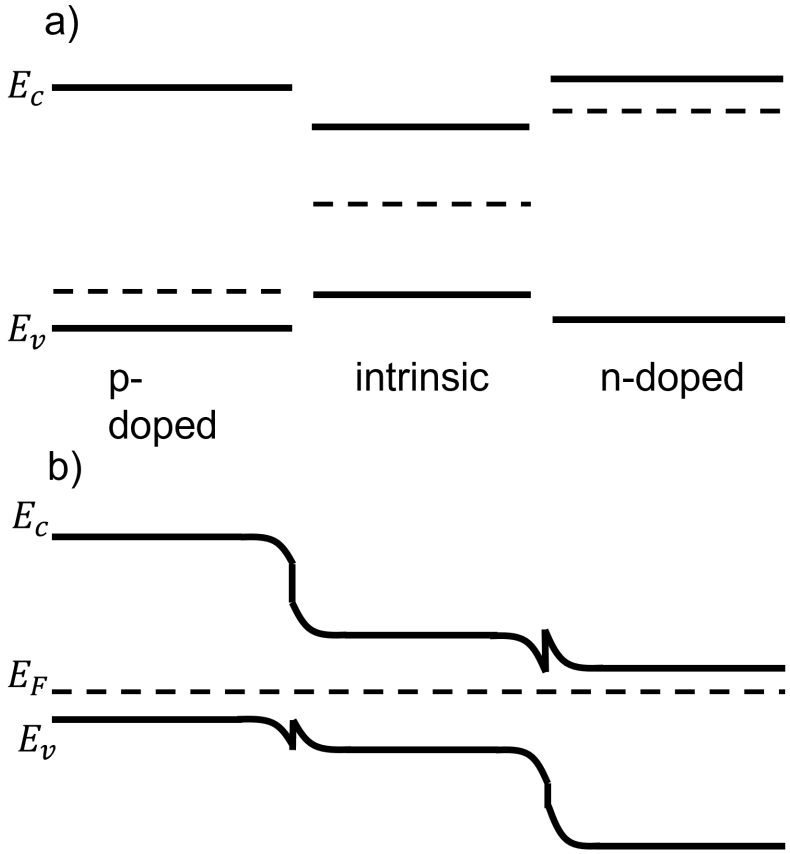

Figure 2.6: Diagram showing the spatial variation of the conduction (E_c) and valence (E_v) band-edge energies, and the Fermi energy (E_F) for (a) spatially separate p-type, intrinsic, and n-type semiconductor, and (b) the resulting unbiased p-i-n double heterostructure that forms after combining the three. Here, the p- and n-doped material are of the same species, while the intrinsic material is a semiconductor with a narrower bandgap. The solid lines show the band-edge, while the dashed lines show the Fermi level.

field that causes the bands to bend, effectively acting as a potential barrier.

Figure 2.6 shows the energy band diagram of an unbiased p-i-n double heterostructure (DH), which consists of a smaller bandgap intrinsic material sandwiched by a larger bandgap p- and n-doped material. There is an electric field across the p-i and i-n interface, where the carriers recombine. Misalignment of the energy bands leads to band discontinuities at the interface. The DH has significant advantages over simple p-n junctions for optoelectronic devices. Due to the narrower bandgap energy, electrons and holes are confined to the intrinsic material, when forward biased, improving the recombination efficiency. Additionally, the refractive index is typically higher for narrow band gap material, and as will be explained in section

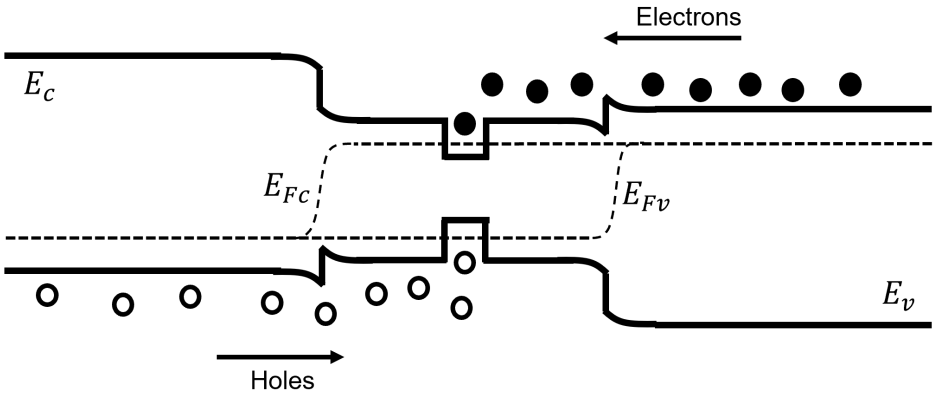

Figure 2.7: Diagram showing the spatial variation of the conduction (E_c) and valence (E_v) band-edge energies for a forward biased separate confinement heterostructure (SCH). Here, the SCH is formed by surrounding a narrow bandgap intrinsic layer, with a wider bandgap intrinsic layer on each side. The intrinsic region is then sandwiched by wide bandgap, p- and n-doped layers on the the left and right side, respectively. The SCH is forward biased and not in thermal equilibrium. The electron and hole population are described by the separate quasi-Fermi energies E_{Fc} and E_{Fv}, respectively. Electrons (closed circles) are injected from the n-doped semiconductor, while holes (open circles) are injected from the p-doped semiconductor.

2.7, this confines light to the intrinsic material, where optical losses due to doping are reduced, and improves the overlap with the gain generating layers.

Figure 2.7 shows the energy band diagram of a simple p-i-n separate confinement heterostructure (SCH) under forward bias. The SCH is similar to a DH but contains separate active layers (such as quantum well or quantum dot layers) within the intrinsic region. The application of a forward bias reduces the barrier height due to carrier depletion at the interface, allowing a current to flow. Under forward bias, the Fermi-levels of the electron and hole population are no longer the same, and separate quasi-Fermi levels are used instead.

2.6 Free carrier absorption

In conductors, optical losses can occur when free carriers that are driven by an oscillating electric field are scattered by impurities. Free carrier absorption (FCA) can be significant in semiconductor material with high doping densities.

Equation 2.12 gives the absorption coefficient for FCA, α_{FCA}, derived from classical Drude theory [48]

$$\alpha_{\mathrm{FCA}} = \frac{Ne^3\lambda^2}{4\pi^2\mu m^{*2} n\varepsilon_0 c^3} \tag{2.12}$$

where N is the free carrier density, e is the charge of an electron, λ is the wavelength, μ is the carrier mobility, m^* is the effective mass of the carrier, n is the refractive index of the material, ε_0 is the dielectric constant and c is the speed of light in free space. Equation 2.12 shows a linear and quadratic dependence on the carrier density and wavelength, respectively. Experimental measurements show that the FCA is proportional to the doping concentration [36][49][50][51]. However, in the near-infrared region, a very weak λ dependence has been observed for n-doped GaAs, while a λ^3 dependence has been observed for p-doped GaAs [36].

2.7 Waveguides

A dielectric waveguide is formed by surrounding a high refractive index core with a low refractive index cladding and uses total internal reflection to guide light along the waveguide with low optical loss. As a result of the confinement, the electromagnetic (EM) wave solutions within the waveguide are discretised. These solutions are known as optical modes.

2.7.1 Slab Waveguides

One of the simplest types of waveguides is the slab waveguide, and figure 2.8 shows an example of a symmetric 3-layer slab waveguide, where the refractive index varies along the y-axis only and the propagation direction is along the z-axis. The guided modes of a slab waveguide can be categorised into transverse electric (TE) and transverse magnetic (TM) polarised modes. The TE mode has a non-zero E_{x} with $E_{\mathrm{y}} = E_{\mathrm{z}} = 0$. The TM mode has $E_{\mathrm{x}} = 0$ with a non-zero E_{y} and E_{z}, although typically E_{z} is small compared to E_{y} [52].

The propagation of light is altered within the waveguide, as the confinement introduces a wavevector component that's perpendicular to the direction of propagation. The components

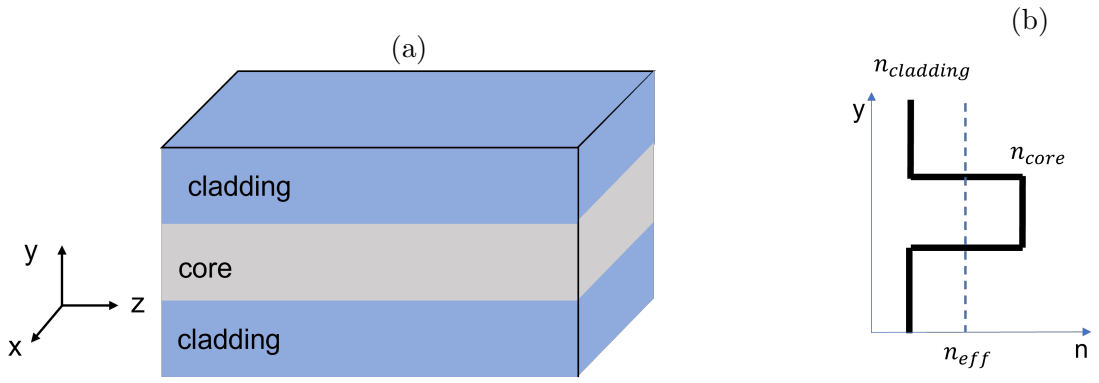

Figure 2.8: (a) Schematic diagram of a 3-layer slab waveguide and (b) the refractive index profile along the y-axis. The dashed line shows the effective index n_{eff} of a single guided mode.

of the wavevector in a given layer i of the slab waveguide have the relation

$$n_{\text{i}} k_0^2 = k_{\text{ti}}^2 + \beta^2 \tag{2.13}$$

where n_{i} k_0 gives the magnitude of the wavevector in a particular layer with a refractive index n_{i}. $k_0 = 2\pi/\lambda$ is the wavevector in free space, and λ is its wavelength in free space. k_{t} is the transverse component of the wavevector, along the direction perpendicular to the plane of the slabs. β is the component of the wavevector along the propagation direction, and is known as the propagation constant. It describes the phase relationship as the mode propagates. Modes can also be described by an effective index n_{eff}, which is related to the propagation constant by

$$\beta = n_{eff} k_0 \tag{2.14}$$

Guided modes have an effective index value between the cladding and core refractive index value. The number of guided modes in a 3-layer slab waveguide depends on the core width and the refractive index contrast of the core and cladding material. There are fewer guided modes when the core width is reduced and the refractive index contrast is lower.

The relationship between the frequency (or angular frequency ω) and the propagation constant in a waveguide is known as its dispersion relation. The group velocity of a mode is related to

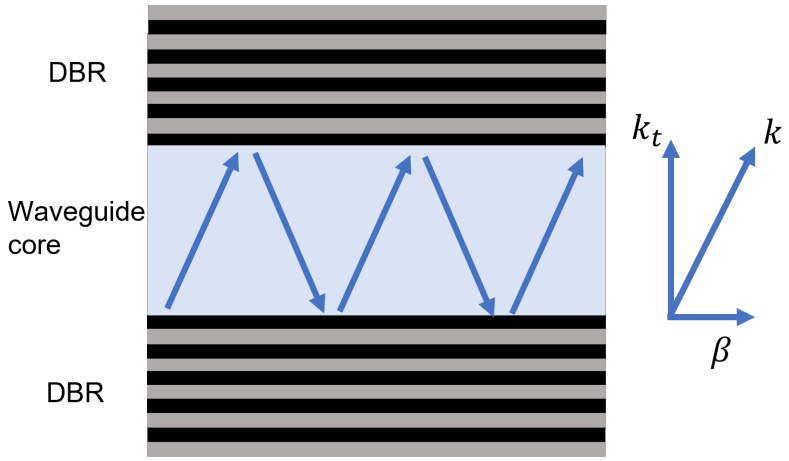

Figure 2.9: Basic structure of a Bragg reflector waveguide formed by highly reflecting DBR mirrors. The components of the wavevector of the mode in the core layer are shown, where β is the propagation constant, k_t is the transverse component, and k is the magnitude.

the 1st derivative of the dispersion curve and is given by

$$v_{\text{group}} = \frac{d\omega}{d\beta} = \frac{\text{c}}{n_{\text{group}}} \tag{2.15}$$

2.7.2 Bragg Reflector Waveguide

Bragg reflector waveguides are a multi-layer slab waveguide where highly reflective mirrors are used to guide the light. At wavelengths just below the vertical cavity resonance wavelength, these waveguides are highly dispersive and the modes can have a significantly reduced in-plane group velocity [53][54]. As such, these modes are sometimes referred to as slow light modes. Figure 2.9 shows the typical structure of a Bragg reflector waveguide.

The structure is similar to that of a vertical-cavity surface-emitting laser (VCSEL) and effectively forms a vertical cavity. The transverse component of the wavevector in the core layer of the waveguide, k_{tc}, is determined by the vertical resonance condition so that

$$k_{\text{tc}} = \frac{2\pi n_{\text{core}}}{\lambda_{\text{v}}} \tag{2.16}$$

where λ_v is the vertical cavity resonance wavelength. Neglecting material dispersion, the transverse wavevector component is constant with wavelength. Using equation 2.16 and 2.14 in equation 2.13, a dispersion relation for the slow light waveguide can be derived [53]

$$\frac{n_{\text{eff}}}{n_{\text{core}}} = \sqrt{1 - \left(\frac{\lambda}{\lambda_v}\right)^2} \tag{2.17}$$

It can be seen that real values for n_{eff} are only possible for wavelengths shorter than the cavity resonance wavelength. Since the transverse component is fixed in size and determined by the vertical resonance condition, for wavelengths longer than the vertical cavity resonance, the transverse component is larger than the total wavevector and the propagation constant is purely imaginary.

2.7.3 Material and Modal Gain

The modal gain can be defined as the fractional increase in energy, contained within an optical mode, per unit length. The material gain is a material property and is the gain experienced by a mode confined entirely within the gain medium and whose propagation is not affected by guiding [44]. The per unit length material gain, g and the per unit length modal gain G is related by

$$G = \Gamma g \tag{2.18}$$

where Γ is known as the confinement factor, which is the ratio of the modal and material gain. In a dielectric waveguide the confinement factor can be expressed as [55]

$$\Gamma = \frac{\frac{1}{2}\varepsilon_0 c n_{\text{act}} \iint_{\text{active}} |\vec{E}|^2 \, dx \, dy}{\frac{1}{2} \iint Re(\vec{E} \times \vec{H}^*) \cdot \hat{z} \, dx \, dy} \tag{2.19}$$

where n_{act} is the refractive index of the active layer, $\vec{E}$ is the electric field and $\vec{H}$ is the magnetic field. The denominator is an integral of the component of the Poynting vector along the propagation direction, over the cross-section of the waveguide, and gives the total power flow of the mode.

For the TE polarised mode in a multi-layer slab waveguide, this can be expressed as

$$\vec{S} = \frac{1}{2} Re(\vec{E} \times \vec{H}^*) \cdot \hat{z} = \frac{\beta}{2\omega\mu_0} |\vec{E}(y)|^2 \tag{2.20}$$

This expression is valid when there is material dispersion. Here, it is important to note that the propagation constant or effective index relates the power flow to the electric field. By definition, the group velocity relates the power flow to the internal energy of the mode. Using equation 2.20, equation 2.19 simplifies to [43][52]

$$\Gamma = \frac{n_{\text{act}}}{n_{\text{eff}}} \Gamma_0 \tag{2.21}$$

where Γ_0 is the conventional confinement, which is the electric field overlap with the gain material. For a multi-layer slab waveguide, this can be expressed as

$$\Gamma_0 = \frac{\int_{\text{active}} |\vec{E}(y)|^2 \, dy}{\int_{\text{mode}} |\vec{E}(y)|^2 \, dy} \tag{2.22}$$

2.8 VCSEL Structure

Unlike edge emitting lasers (EELs), VCSELs have a vertical optical cavity, so that emission of the lasing mode is perpendicular to the wafer surface [56][57]. Figure 2.10 shows a schematic diagram of a typical oxide-confined top-emitting VCSEL structure, similar to the devices presented in this thesis. Due to its vertical structure, the cavity can be defined epitaxially, with top and bottom distributed Bragg reflectors (DBRs) forming the mirrors. Optical gain is typically generated by QWs that are positioned at the anti-node of the standing wave profile within the cavity (as shown in figure 2.11), so that coupling to the optical mode is maximised. Ring contacts are used for current injection in the top DBR so that light can be emitted out of the top mirror.

DBRs consist of alternating layers of high and low refractive index material that each have

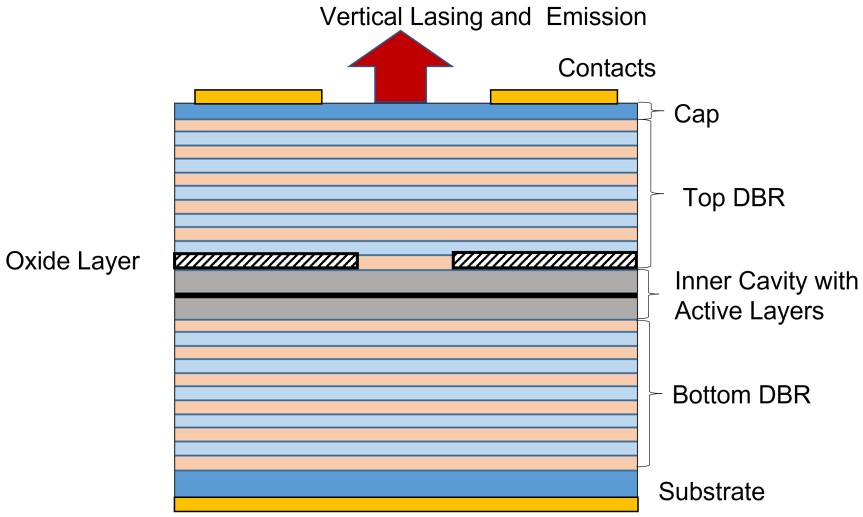

Figure 2.10: Schematic diagram of a typical oxide-confined top-emitting VCSEL structure. The inner cavity containing the active layers are sandwiched between top and bottom distributed Bragg reflectors. A high Aluminium concentration AlGaAs layer is positioned just above the cavity, and can be oxidised to form an oxide aperture. A bottom planar contact, and a top ring contact provide current injection, and optical emission is via the top surface from within the ring.

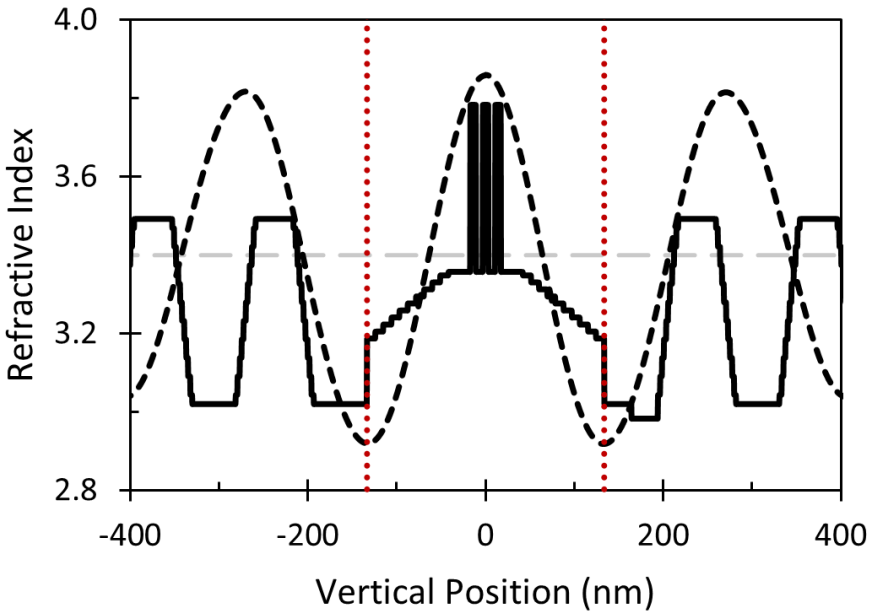

Figure 2.11: Refractive index profile (black solid) of a 1-λ cavity VCSEL, showing the inner cavity, containing three quantum well (QW) layers, and two distributed Bragg reflector pairs on either side. For the purposes of simulating the electric field, the graded regions have been discretised. The electric field profile (black dashes) is superimposed and shows the central anti-node positioned at the QW layers. The horizontal grey dashed line corresponds to $|\vec{E}| = 0$, and the red dotted lines mark the boundaries of the cavity.

a 1/4-λ optical thickness. Due to the short length of the gain material, a very high mirror reflectivity is necessary to ensure mirror losses are low enough for low threshold current lasing to occur [58]. By having a large number of mirror pairs, a mirror reflectivity $> 99\%$ can be obtained, with the maximum achievable reflectivity limited by internal optical losses. The bottom DBR has a higher number of DBR layers compared to the top, so that light is emitted from the top and reflections at the substrate contact interface don't affect the VCSEL characteristics.

As the VCSEL cavity is defined epitaxially, the cavity length can be made very short (as short as 1/2-λ). The longitudinal mode spacing can be of the same order as the gain and DBR reflectivity bandwidth so that only a single longitudinal mode lases. Unlike EELs, the lasing wavelength is determined by the vertical cavity rather than the gain-peak wavelength. The cavity-resonance wavelength has a lower temperature dependence compared to the gain-peak wavelength, determined largely by the temperature dependence of the refractive index and bandgap, respectively. Therefore, the emission wavelength of a VCSEL is typically considered to be more temperature stable. On the hand, the threshold current has a strong temperature dependence due to the detuning of the cavity resonance and gain-peak wavelength.

The large number of interfaces contained within the DBR mean the series resistance of a VCSEL is higher than EELs. The mirrors are highly doped to reduce the series resistance of the device, but this can also increase the optical losses due to FCA. Modulation doping of just the interface can reduce the barrier potential, and thus the resistance, while keeping optical losses low [59][60]. The use of a double mesa structure with intracavity contacts can lower the device resistance by reducing the number of interfaces traversed by the current. This also reduces FCA in the DBR layers, as a high doping concentration is no longer necessary to ensure the series resistance stays low.

The oxide aperture is formed by oxidising a thin, high Al concentration, AlGaAs layer, located just above the active layer, in a humid H_2O/N_2 mixture [61][62]. The resulting AlO_x material has a lower refractive index and is an insulator, so that the aperture provides both optical

and current confinement for improved transverse overlap of the mode with the gain region.

2.8.1 Transfer Matrix method

The transfer matrix method is commonly used to describe the propagation of an EM wave through a one-dimensional (1D) multilayer structure, and can determine the key characteristics of VCSEL structures, such as its cavity resonance wavelength and mirror reflectivity [43][20][63]. The electric field of a linearly polarised EM wave, in a homogenous medium in 1D, can be written as a superposition of the forwards and backwards propagating solutions.

$$E(z) = E^{+}\exp(\tilde{\beta}z) + E^{-}\exp(-\tilde{\beta}z) \tag{2.23}$$

where E^{+} and E^{-} are the complex electric field amplitudes of the forwards and backwards propagating wave, z is the position along the propagation direction, and $\tilde{\beta}$ is the complex propagation constant. In a homogeneous medium, no guiding is present so that $\tilde{\beta}$ can be expressed using the complex refractive index of the material $\tilde{n}$

$$\tilde{\beta} = \tilde{n}k_0 \tag{2.24}$$

The real part of $\tilde{n}$ is the refractive index of the material, while the imaginary part of $\tilde{n}$ is related to the Beer-Lambert law, per unit length, absorption coefficient α of the material by

$$\Im(\tilde{n}) = \frac{\alpha\lambda}{4\pi} \tag{2.25}$$

The imaginary part of $\tilde{n}$ is defined so that a positive α leads to the electric field of the forward propagating wave decaying along the positive z-direction. A negative α, instead, leads to amplification and describes a material gain (i.e $g = -\alpha$).

For light propagation across an interface, the relation between the fields, in each material at

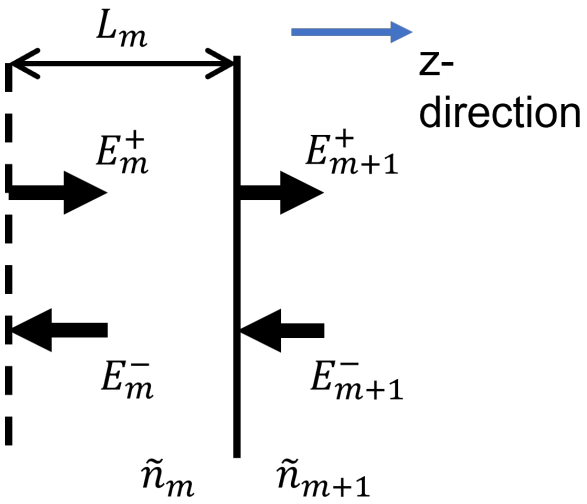

Figure 2.12: Diagram showing the forwards and backwards propagating electric field in layers m and m+1 described by the matrix equation 2.28. It is assumed the layers are stacked along the propagation direction, and are invariant in the transverse direction.

the interface, can be determined from the standard interface conditions for EM fields [64]

$$\hat{n} \times (\vec{E}_1 - \vec{E}_2) = 0 \tag{2.26}$$

$$\hat{n} \times (\vec{H}_1 - \vec{H}_2) = J_s \tag{2.27}$$

where J_s is the surface current density, with the subscript denoting the material. $\hat{n}$ is a unit vector along the direction normal to the plane of the interface, so that these conditions are for the field components tangential to the interface. Similar interface conditions exist for the components of the electric and magnetic field vectors that are normal to the interface. Since only dielectric material is being considered, the surface current density is zero. Then, for the 1D, linearly polarised, EM wave considered here, when the wave propagation is normal to the interface, both the electric and magnetic field is tangential to the interface. From equations 2.26 and 2.27, this leads to both the electric field E and its 1^{st} derivative $\frac{dE}{dz}$to be continuous across the interface [20].

The relation between the complex electric-field amplitude of the forwards and backwards propagating waves in adjacent layers m and m+1, as shown in figure 2.12, can be expressed

in matrix form as

$$\begin{bmatrix} E^{+}_{\mathrm{m+1}} \\ E^{-}_{\mathrm{m+1}} \end{bmatrix} = T_{\mathrm{m}} \begin{bmatrix} E^{+}_{\mathrm{m}} \\ E^{-}_{\mathrm{m}} \end{bmatrix} \tag{2.28}$$

with

$$T_{\mathrm{m}} = \begin{bmatrix} \frac{1}{2}(1+\frac{\tilde{n}_{\mathrm{m}}}{\tilde{n}_{\mathrm{m+1}}})e^{i\tilde{\beta}_{\mathrm{m}}L_{\mathrm{m}}} & \frac{1}{2}(1-\frac{\tilde{n}_{\mathrm{m}}}{\tilde{n}_{\mathrm{m+1}}})e^{-i\tilde{\beta}_{\mathrm{m}}L_{\mathrm{m}}} \\ \frac{1}{2}(1-\frac{\tilde{n}_{\mathrm{m}}}{\tilde{n}_{\mathrm{m+1}}})e^{i\tilde{\beta}_{\mathrm{m}}L_{\mathrm{m}}} & \frac{1}{2}(1+\frac{\tilde{n}_{\mathrm{m}}}{\tilde{n}_{\mathrm{m+1}}})e^{-i\tilde{\beta}_{\mathrm{m}}L_{\mathrm{m}}} \end{bmatrix} \tag{2.29}$$

where L is the thickness of a layer, and the subscript denotes the layer. To describe propagation through multiple layers, the transfer matrices can be multiplied as below

$$\begin{bmatrix} E^{+}_{\mathrm{m+1}} \\ E^{-}_{\mathrm{m+1}} \end{bmatrix} = T_{\mathrm{m}} \cdot T_{\mathrm{m-1}} \ \ldots \ T_2 \cdot T_1 \begin{bmatrix} E^{+}_{1} \\ E^{-}_{1} \end{bmatrix} \tag{2.30}$$

The reflection coefficient of the multi-layer structure, at the interface between layer m and m+1, can be defined as the ratio of the electric field of the forwards and backwards propagating EM wave

$$r = \frac{E^{+}_{\mathrm{m+1}}}{E^{-}_{\mathrm{m+1}}} \tag{2.31}$$

with $E^{+}_{1} = 0$. The reflectivity is given as $R = r^{*}r$. With the matrix defined as in equation 2.29, the reflection coefficient for the structure at the interface between layer 1 and 2 requires layer 1 to have zero thickness, and $E^{-}_{\mathrm{m+1}} = 0$. The lasing wavelength, threshold gain, and electrical field profile are determined by the boundary condition [63]

$$E^{+}_{1} = E^{-}_{\mathrm{m+1}} = 0 \tag{2.32}$$

which simply states that there is no incoming light in layers 1 and m+1 which surround the VCSEL structure. Solutions which satisfy this condition are only possible when there is gain within the structure [63].

Equations that describe the lasing wavelength and threshold gain conditions for the VCSEL structure can also be derived. Here, the VCSEL structure is split into top and bottom sections,

and the complex reflection coefficient at the split is calculated separately for each section.

For sustained laser oscillation, the electric field after one round-trip must be the same as the initial electric field E_0. This requirement is expressed by

$$r_{\text{top}} r_{\text{bot}} E_0 = E_0 \tag{2.33}$$

where r_{top} and r_{bot} is the reflection coefficient of the top and bottom mirror. Gain can be included implicitly via the imaginary part of the refractive index in the gain layers, in which case, equation 2.33 is a restatement of the boundary condition 2.32. Alternatively, we can include the gain of the active layers, g_{act}, explicitly so that we get the approximate equation

$$r_{\text{top}} r_{\text{bot}} \exp(\Gamma_{\text{enh}} g_{\text{act}} L_{\text{act}}) = 1 \tag{2.34}$$

where the exponential term describes the round-trip gain due to the active layers which have a total thickness of L_{act}. The factor of 2 due to the light traversing the active layers twice is cancelled by a factor of $\frac{1}{2}$ that appears as the gain term is from the Beer-Lambert law which describes the change in intensity. Γ_{enh} is an enhancement to the coupling of the active layers with the electric field due to standing wave effects and is given by

$$\Gamma_{\text{enh}} = \frac{\int_{\text{active}} |E^+(z) + E^-(z)|^2 \, dz}{\int_{\text{active}} |E^+(z)|^2 + |E^-(z)|^2 \, dz} \tag{2.35}$$

Taking the argument of equation 2.34, gives the phase condition at the lasing wavelength

$$\arg(r_{\text{top}} r_{\text{bot}}) = 2m\pi \tag{2.36}$$

where m is an integer. From the modulus of equation 2.34, the threshold condition can be found [44]

$$\Gamma_{\text{enh}} g_{\text{act}} L_{\text{act}} = ln \left(\frac{1}{\sqrt{R_{\text{top}} R_{\text{bot}}}} \right) \tag{2.37}$$

2.9 Power-Current Characteristics

The optical power-current ($P_{\text{opt}} - I$) relationship, above the threshold current, I_{th}, is given by[20][43]

$$P_{\text{opt}} = \eta_{\text{ext}} \frac{\hbar\omega}{e} (I - I_{\text{th}}) \tag{2.38}$$

where the external efficiency, η_{ext}, gives the fraction of the current above threshold that's converted into photons which are coupled out of the cavity. The external efficiency multiplied by $\hbar\omega/e$ is known as the slope efficiency. The external efficiency is given by

$$\eta_{\text{ext}} = \eta_{\text{i}} \frac{\alpha_{\text{m}}}{\alpha_{\text{m}} + \alpha_{\text{i}}} \tag{2.39}$$

where η_{i} is the injection efficiency that gives the fraction of current that is converted into photons inside the cavity, α_{i} is the internal optical loss and α_{m} is the mirror loss. This expression assumes that the number of photons extracted out of the cavity is significantly higher on one side of the cavity. For VCSELs, size dependent losses, such as scattering due to the oxide aperture, are often written separately to α_{i}. The mirror loss can be written as

$$\alpha_{\text{m}} = \frac{1}{L} \ln\left(\frac{1}{r_1 r_2}\right) \tag{2.40}$$

where r_1 and r_2 are the reflection coefficients of the mirrors, and L is the length of the cavity. In VCSELs, an effective cavity length is used due to an additional wavelength dependent phase shift by the DBRs [20][43].

For edge emitters, it is possible to vary the mirror loss by fabricating multiple devices with different cavity lengths. Using equations 2.39 and 2.40, the inverse external efficiency can plotted as a function of cavity length to determine the injection efficiency and internal optical loss. Some considerations that can impact the measurement are discussed in [65]. A brief overview of this method applied to VCSEL structures is given in section 1.4.2.

2.10 Thermal Effects in a VCSEL

A VCSEL device under continuous wave (CW) operation, will see its internal temperature increase due to the power dissipated within the device. The total dissipated power $P_{\text{dissipated}}$ can be expressed as [20]

$$P_{\text{dissipated}} = IV - P_{\text{opt}} = IV_0 + I^2 R_{\text{series}} - P_{\text{opt}} \tag{2.41}$$

where V is the voltage across the top and bottom contacts of the VCSEL, V_0 is the voltage across the diode, and R_{series} is the series resistance of the device. The total electrical power, IV, supplied to the device can be separated into the power dissipated by the series resistance, $I^2 R_{\text{series}}$, and the power transferred to recombination processes in the diode, IV_0, which have a quadratic and linear dependence on current respectively. A portion of the power transferred to recombination process is converted into useful optical power that is emitted out of the VCSEL, and therefore, does not contribute to the heating. For devices with a low series resistance, at low currents, the dissipated power will have an approximately linear dependence on current.

The internal temperature increase ΔT for a given dissipated power can be described by a thermal resistance R_{thermal}[20]

$$R_{\text{thermal}} = \frac{\Delta T}{P_{\text{dissipated}}} \tag{2.42}$$

The thermal resistance is higher for smaller oxide aperture devices as the AlO_x is a poor thermal conductor and the temperature increase is larger for smaller oxide aperture devices. It is possible to determine the thermal resistance through experimental measurements of the wavelength. The temperature dependence of the refractive index causes the cavity resonance wavelength to shift with the operating temperature and dissipated power. The thermal resistance can be determined by measuring the wavelength shift with heat-sink temperature, where the power dissipation is negligible (e.g by operating the VCSEL in pulsed-mode at low injection current), and the wavelength shift with power dissipation, keeping the heat-sink temperature

constant.

At high injection currents, the leakage current and non-radiative recombination increases, due to the high internal temperature, which reduces the injection efficiency. Additionally, the gain-peak and cavity resonance wavelength can become detuned. Higher current densities are required to maintain the threshold gain, reducing the slope of the P-I curve. When the slope efficiency becomes negative, this is known as thermal rollover.

2.11 Transverse Modes of Oxide Confined VCSELs

The oxide aperture can have a significant effect on the transverse modes of a VCSEL. The degree of guiding by the oxide aperture depends on the overlap of the oxide layer with the electric field profile of the vertical mode. The refractive index of the oxide layer is lower than that of the AlGaAs, so typically leads to the vertical cavity resonance wavelength being lower in the oxidised region. As explained in section 2.7.2, in-plane propagation of slow light modes, that occur in the VCSEL structure due to the vertical cavity-resonance, can only occur for wavelengths shorter than vertical cavity-resonance wavelength. Therefore, at wavelengths between the cavity-resonance wavelength in the oxidised and unoxidised region, the in-plane component of the wavevector will be real in the unoxidised region, and imaginary in the oxidised region. As a result, this leads to confinement of the mode within the unoxidised region.

2.11.1 Effective Index Method

A number of models exist to calculate the optical modes of a VCSEL, and a comprehensive comparison of these methods can be found in [66]. Of these, the effective index approximation for VCSELs [67][68] is a simple method routinely used to calculate the transverse modes of oxide confined VCSELs. In the effective index approximation, it is assumed that the optical modes of the VCSEL cavity are linearly polarised and are therefore solutions of the scalar wave equation. When the aperture size is large, this is usually a reasonable approximation [69].

The electric field solutions $E(\rho, \phi, z)$ are assumed to have a separable form

$$E(\rho, \phi, z) \approx E_0 F(\rho, \phi) G(z) e^{i\omega t} \tag{2.43}$$

where $F(\rho, \phi)$ and $G(z)$ are normalised functions that contain the transverse and longitudinal dependence respectively. For each region i, they each satisfy their own eigenvalue equation as shown below

$$\left(\frac{\partial^2}{\partial z^2} + \varepsilon_{\mathrm{i}}(z) k_{\mathrm{zi}}^2 \right) G_{\mathrm{i}}(z) = 0 \tag{2.44}$$

$$\left(\nabla_{\mathrm{t}}^2 + k_{\mathrm{ti}}^2 \right) F_{\mathrm{i}}(\rho, \phi) = 0 \tag{2.45}$$

where k_{t} and k_{z} are the transverse and longitudinal components of the k-vector respectively. Equation 2.44 is routinely solved using the transfer matrix method described in section 2.8.1. The transverse and longitudinal k-vector components have the relation

$$k_{\mathrm{ti}}^2 = \langle \varepsilon_{\mathrm{i}} \rangle \left(\frac{\omega^2}{c^2} - k_{\mathrm{zi}}^2 \right) \tag{2.46}$$

In the case of a circular oxide aperture VCSEL, the transverse modes of a VCSEL can be approximated by the linearly polarised (LP) modes [68], which are the approximate modes of an optical fibre with circular symmetry. They are a superposition of the HE and EH modes when $n_{\mathrm{clad}} \approx n_{\mathrm{core}}$ [70].

2.11.2 Single-mode VCSELs

Many applications require single mode emissions, and generally the degree of side mode suppression and the optical power that's coupled into a single mode are used as measures of single-modeness. To achieve single-mode emission with an oxide aperture VCSEL, the higher order modes must have high radiation loss, with only the fundamental mode guided. This can be achieved by positioning the oxide aperture layer close to a node, which reduces the guiding; and by making the oxide diameter small, pushing higher order modes beyond cut-off, further reducing

the number of modes that are guided. Through careful optimisation, an approximately 3.5 µm oxide aperture diameter VCSEL, emitting at 840 nm, was reported to have a single-mode (>30 dB) optical output power of 4.8 mW [71]. For VCSELs emitting at 894.6 nm, >30 dB of single-mode emission at an optical output of 0.6 mW has been demonstrated with an oxide aperture diameter of 3.5 µm. This design also featured an extended cavity for linewidth reduction [72]. Single-mode emission >35 dB, and a maximum optical output power >2 mW was also reported with a 2.5 µm diameter rhomboidal oxide aperture. This design also utilised a composite Bragg mirror for higher output coupling while obtaining a relatively narrow linewidth of 20 MHz at 20 °C [28].

However, there are number of disadvantages associated with this approach. The weak guiding by the oxide aperture means the optical modes are more susceptible to thermal lensing, where the guiding of the mode is affected by temperature induced refractive index increase. The small diameter oxide aperture diameter also increases the thermal and electrical resistance of the VCSEL and leads to greater current induced self-heating. Thermal rollover occurs at lower currents, limiting the maximum optical output power. Additionally, at the dimensions required for single-mode emission, the fundamental mode wavelength becomes quite sensitive to the oxide aperture size [66]. Variations in the oxidation rate across a wafer due to changes in the composition or temperature during the oxidation process will contribute to poorer uniformity of the emission wavelength. Where there are stringent wavelength requirements, such as the case with VCSELs for atomic sensors, this will reduce the yield. Diffraction losses will also be higher for the fundamental mode, and will increase the threshold current density, further shifting the lasing wavelength.

A number of alternative techniques exist, to produce single-mode devices. A surface relief can introduce an additional mode dependent loss, and allows the oxide aperture to be made larger, despite it being able to support multiple modes [73]. If the reflectivity of the mirror is low enough, etching off material from the top layer, so that reflections at the semiconductor air interface are in anti-phase, will significantly increase the mirror loss (see section 5.7.1).

Since different modes have different intensity profiles, if the surface relief is of the right dimensions, this will selectively increase the loss of higher order modes, while keeping the loss of the fundamental mode low enough to ensure preferential lasing. The thickness range of the anti-phase layer to achieve higher mirror loss is rather narrow, and a more tolerant design is the inverted surface relief [74]. Since the layer thickness can be defined more accurately epitaxially, the initial top layer is grown such that the reflections are in anti-phase, and a core region is etched so that reflections are in-phase. With this approach, using a 3 µm diameter surface relief, and a 5 µm oxide aperture diameter, a maximum power of 6.5 mW with >30 dB of higher order mode suppression has been reported for an 850 nm VCSEL [75].

2.11.3 Polarisation

Most circular oxide aperture VCSELs have transverse modes that are (almost) linearly polarised [20]. However, due to the circular symmetry, there is no strong mechanism to fix the polarisation along a particular direction, and switching between orthoganally polarised states can occur during operation [20].

For VCSELs grown on (100) substrates, there is a tendency for the polarisation of the modes to align along or close to the [011] and the [$0\bar{1}1$] axis [76][77]. It was shown in [76], that due to anistropy in the elasto-optic tensors, residual strain causes the principle axes of the refractive index ellipsoid to be orientated close to the [011] and the [$0\bar{1}1$] axes. This birefringence breaks the degeneracy of the orthogonally polarised modes, so that they have slightly different frequencies [78].

A number of approaches such as anisotropic cavity geometries [79], photonic crystal air holes [80], and elliptical surface reliefs [26][81] have been reported in the literature to improve the polarisation stability of VCSELs. Surface gratings, which are etched onto the topmost semiconductor layer and introduce a polarisation dependent loss, are widely used for polarisation control in VCSELs [82][83]. The grating performance depends on the grating depth and period, and

whether the initial cap thickness produce reflections that are anti-phase (inverted design) or in-phase (normal design) relative to the DBR reflection. Grating periods that are larger than the emission wavelength causes diffraction, which increases the optical losses and introduce side lobes in the far-field profile. It was reported in [84], that inverted grating designs have improved tolerance to grating depth variations, and reduced power in side lobes. When the grating period is much smaller than the VCSEL emission wavelength, the grating acts like a birefringent material and there is no significant increase in the optical losses or degradation of the beam quality [85][86], However, electron beam lithography is typically required to define the grating due to its small feature size [20].

Elliptical and non-circular oxide apertures have also been used as a method to produce stable, linearly polarised VCSEL devices [24][25]. It was shown in [26] that elliptical oxide apertures introduce a birefringence, that increases with the aspect ratio, and leads to a difference in gain between the two orthogonally polarised modes. The birefringence is larger for smaller oxide aperture sizes.

2.11.4 Beam Profile

The beam emitted by a VCSEL device (and lasers in general) diverges in free space. When the beam is emitted from the device the wavefronts are approximately planar, and this regime is known as the near-field. The point where the beam is narrowest is known as the beam waist. As the emitted beam diverges, the wavefronts develop a curvature which become spherical in the far-field [43]. In the paraxial approximation, the near-field and far-field beam profiles are related by a Fourier transform [43]. The variance σ^2 of the spatial intensity profile of an arbitrary beam at difference positions along the propagation direction z has a simple relation [87][88]

$$\sigma^2 = \sigma_0^2 + \lambda^2 \sigma_s^2 (z - z_0)^2 \tag{2.47}$$

where σ_0^2 and z_0 are the variance of the spatial intensity profile and the position, respectively, at the beam waist. σ_s^2 is the variance of the angular intensity profile, where s is related to the

emission angle θ by $s = \sin(\theta)/\lambda \approx \theta/\lambda$, and the paraxial approximation is typically assumed. σ_0 and σ_s have a reciprocal relationship. The exact relation depends on the beam profile, so that a real beam can be characterised by the beam propagation factor (BPF), which is commonly known as M^2

$$\sigma_0 \sigma_s = \frac{M^2}{4\pi} \tag{2.48}$$

The ideal Gaussian beam has the minimum $M^2 = 1$, and has the lowest divergence angle for a given beamwidth.

2.12 Conclusion

This chapter covered the key concepts required to understand the basic design and operating characteristics of VCSEL devices. An important part of any laser is the generation of optical gain within its active region. This depends on the electronic states and carrier distribution within the semiconductor, and the interaction strength between the optical field and the electronic states. A population inversion is also required, and this can be achieved with a p-i-n structure, although doping can introduce additional optical losses due to free carrier absorption. Additionally, non-radiative recombination processes are also present in the active layers, and this can effect the radiative efficiency.

In this thesis, an in-plane technique is used to characterise the optical gain within the VCSEL material. The in-plane propagation of light in Bragg reflector waveguides and slab waveguides were described, and the relation between the material gain and modal gain was given.

VCSELs are a type of semiconductor laser where optical emission occurs perpendicular to the wafer surface. To achive this, a short, vertical cavity can be defined epitaxially using top and bottom DBRs. Most VCSEL devices also feature an oxide aperture, which is formed by oxidising a high Al concentration AlGaAs layer, and used for lateral current and optical confinement. The oxide aperture has a major impact on the optical power, wavelength, and polarisation characteristics of a VCSEL device. Simple methods to calculate key VCSEL

characteristics were also outlined. The threshold gain and longitudinal modes can be determined using the transfer matrix method, while the transverse modes can be approximated using the effective index method.

Chapter 3

Measurement Setup

3.1 Introduction

In this thesis, vertical-cavity surface-emitting laser (VCSEL) devices, and the epitaxial material the devices were fabricated from, are characterised. In chapter 5, the optical gain generated by the active layers within the VCSEL material are characterised using a stripe length method known as the segmented contact technique. The first part of this chapter introduces the relevant background theory and the experimental set up for the segmented contact method. In chapter 4, the impact of the oxide aperture dimensions on the device performance, for a given epitaxial material, is investigated. The application place requirements on the threshold current, optical power, emission spectrum, polarisation, and beam divergence of the VCSEL device. The remaining parts of this chapter describe the experimental setups and methodology used to measure these characteristics.

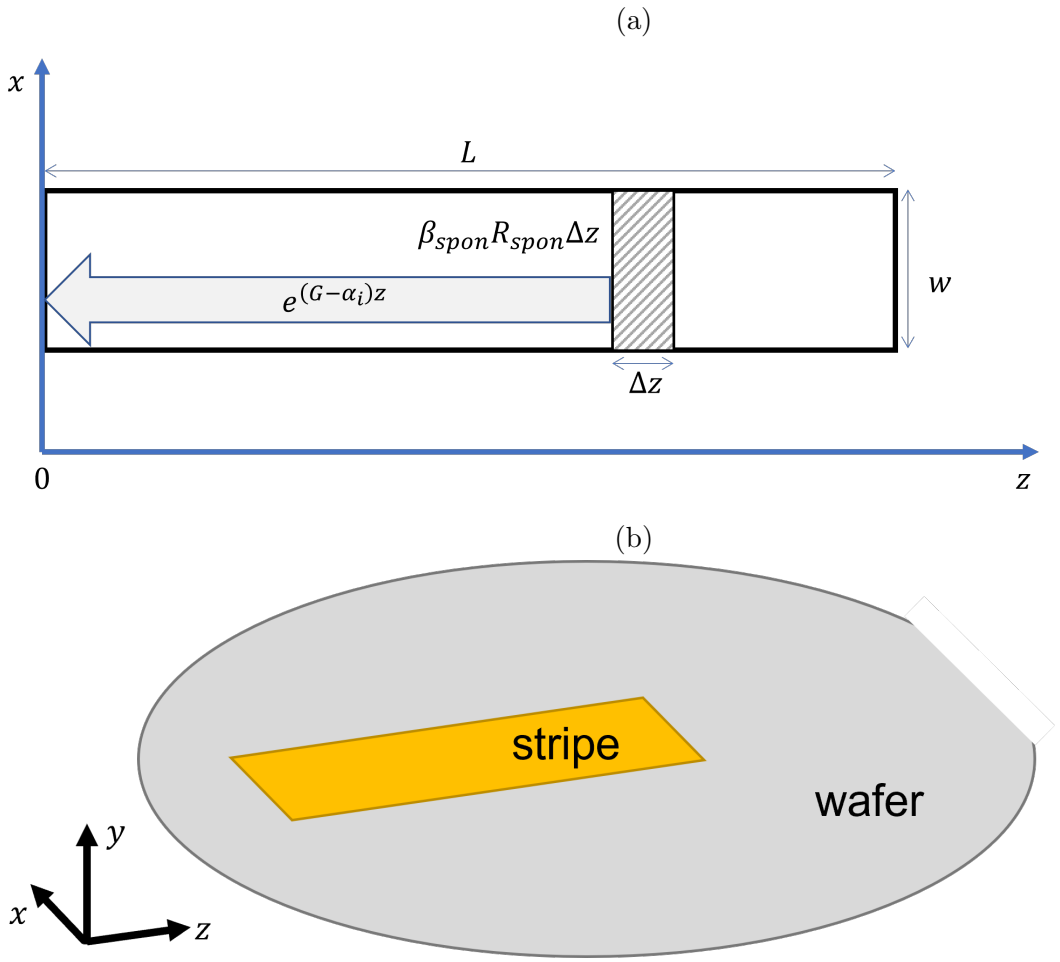

Figure 3.1: Diagram showing (a) how the spontaneous emission coupled into the mode is amplified across the stripe, and (b) the orientation of the stripe relative to the wafer. The $x - z$ plane corresponds to the wafer plane, and the growth direction is along the y-axis. L and w is the length and width of the pumped stripe, respectively. R_{spon} is the spontaneous emission rate from a small length element Δz, and β_{spon} gives the fraction of the spontaneous emission that's coupled into the slab waveguide mode propagating along the negative z direction. G is the modal gain, and α_i is the internal optical loss. The front facet of the stripe is positioned at z=0. For (b), the size of the stripe is not to scale and has been enlarged for clarity.

3.2 Segmented Contact Technique

3.2.1 Stripe-Length Gain Measurement Theory

Variable stripe-length methods, where the single-pass amplified spontaneous emission (ASE) over known lengths is measured, offer a direct way of determining the optical gain coefficient. Figure 3.1 shows the ASE, measured at the facet, from a small length element in a uniformly pumped stripe of length L. The stripe can be pumped either optically or electrically. Typically, the stripe utilises a slab waveguide structure so that a fraction, β_{spon}, of the spontaneous emission generated is coupled into the guided mode, which is then amplified as it propagates along the stripe to the facet. An expression for the ASE rate, I, at the facet due to a small length element Δz at position z is given by [44]

$$I(z) = (\beta_{\text{spon}} R_{\text{spon}} \Delta z) \exp[(G - \alpha_{\text{i}})z] \tag{3.1}$$

where β_{spon} is the fraction of the spontaneous emission coupled into the guided mode, R_{spon} is the spontaneous emission rate, and $(G - \alpha_{\text{i}})$ is the net modal gain where G is the modal gain due to the active layer, α_{i} is the internal optical mode loss due to absorption by free carriers and scattering by irregularities at interfaces.

By integrating equation 3.1 over the entire length of the stripe, the total measured ASE intensity (equation 3.2) can be found where C accounts for back reflection at the front facet and any coupling losses

$$\begin{aligned} I(L) &= C\beta_{\text{spon}} R_{\text{spon}} \int_0^L \exp[(G - \alpha_{\text{i}})z]\, dz \\ &= C\beta_{\text{spon}} R_{\text{spon}} \frac{\exp[(G - \alpha_{\text{i}})L] - 1}{G - \alpha_{\text{i}}} \end{aligned} \tag{3.2}$$

By measuring the ASE of different length stripes, the modal gain at a given current density can be found by fitting equation 3.2 to the data. For long lengths, the photon density will

become high, and the stimulated emission rate comparable to the electrical injection rate, so that the gain will start to saturate.

The segmented contact technique is a variation of the standard stripe-length method [89][90]. Instead of multiple stripes of different lengths, a single stripe with multiple segments is fabricated so that the effective length can be altered by changing the number of sections that are pumped. This has the advantage that the stripe only needs to be aligned once.

For the two-section measurement, two adjacent sections are electrically pumped individually and then simultaneously which effectively doubles the stripe length. The in-plane ASE spectra is measured and the net modal gain can be calculated using equation 3.3 [90]

$$G - \alpha_{\mathrm{i}} = \frac{1}{L} \ln\left(\frac{I_{\mathrm{meas}}(1+2)}{I_{\mathrm{meas}}(1)} - 1 \right) \tag{3.3}$$

where L is the length of a single segmented contact section, and $I_{\mathrm{meas}}(...)$ is the measured ASE with the pumped section denoted within the brackets. The zero-bias modal absorption due to the active layers A can be calculated using equation 3.4 [90]

$$A + \alpha_{\mathrm{i}} = \frac{1}{L} \ln\left(\frac{I_{\mathrm{meas}}(1)}{I_{\mathrm{meas}}(2)} \right) \tag{3.4}$$

Electrical isolation should be high enough to ensure sections adjacent to the pumped section are not pumped. Otherwise, this can alter the length of the pumped stripe. The intercontact resistance can be increased by etching the highly doped cap layer between sections. The gaps between the sections should be large enough so that the sections can be driven independently, but small enough so that current spreading can ensure the current density profile is uniform. Alternatively, ion implantation could be used to increase the resistivity of regions between the sections, but is not the method used for the devices fabricated in this thesis.

3.2.2 Current Compensation

When the electrical isolation between each section is poor, regions beyond the pumped section may be pumped. To prevent this, adjacent sections can be grounded so that carriers are drawn to the contacts rather than pumping adjacent sections. Additionally, light travelling in the reverse direction will be absorbed by the grounded section and this can prevent round-trip amplification from occurring.

However, to ensure each section is pumped with the correct current, it is necessary to compensate for the leakage current [91]. By fitting a linear curve below turn-on, the resistance of the leakage path can be determined, so that for a given voltage, the leakage current can be calculated and accounted for. It is important to minimise (or correct for) the series resistance of the cables in the measurement setup which can increase the measured voltage and otherwise lead to the leakage current being overestimated.

3.2.3 Collection Geometry

$$\Theta_{\max} = \tan^{-1}\left(\frac{(1-\varepsilon)w/2}{L_{\max}}\right) \tag{3.5}$$

The collection geometry can have a significant impact on the measured gain spectra. Collection of light that has passed through unpumped regions should be avoided, by collecting ASE from a narrow region at the centre of the stripe. Additionally, as shown in figure 3.2, due to the finite width of the stripe, the path length of light rays with internal angles greater than $\Theta_{\max}$, given by equation 3.5, cannot be increased by increasing the stripe length [92]. The intensity of a double length stripe is underestimated and leads to a downward shift in the gain spectra. The downward shift increases with increasing optical gain and can therefore cause a compression of the measured gain. Although the difference in shift can be reduced when the intensity is measured across the entire stripe width, this also reduces $\Theta_{\max}$.

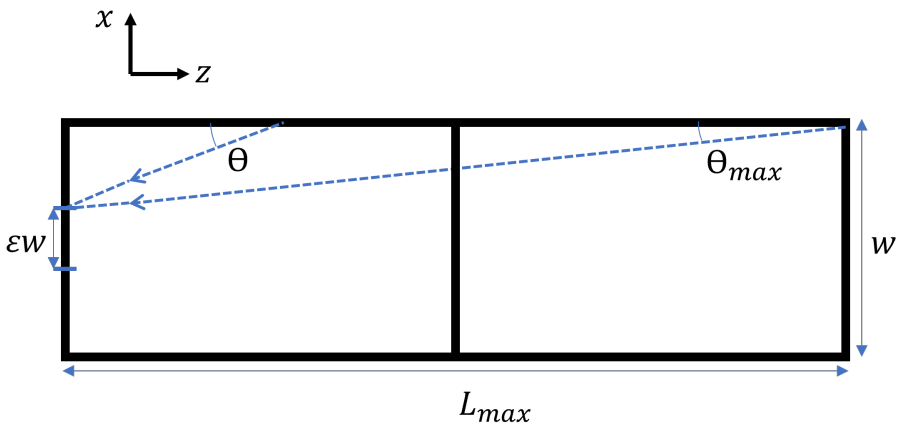

Figure 3.2: Top-down view of a simplified double-length segmented contact showing the maximum internal angle, Θ_{max}, for a collected ray to have been able propagate over the entire length of the double-section stripe. w is the stripe width, εw is the collection width, L_{max} is the length of the double-section stripe, and Θ is the internal angle of a ray that is unable to propagate the entire length.

3.2.4 Segmented Contact Setup

The experimental setup was set up as shown in figure 3.3. The sample was mounted onto a copper mount that was fixed to a 6-axis stage which has three translational and three rotational degrees of freedom. A lens was then used to couple light into the Andor Kymera spectrometer by imaging the front facet of the segmented contact stripe onto the slits. To reduce the collection of partially amplified light, an aperture was placed in front of the lens, limiting the full width collection angle to approximately 4°. A linear polariser was positioned between the lens and the spectrometer slits to select the TE polarised light. The ASE spectra was measured using a 256×1024 pixel Andor iStar charge-coupled device (CCD) camera, which features an image intensifier. The camera software allows selection of particular tracks and was used to ensure the collected ASE was from a narrow region at the centre of the stripe. The camera was gated with the ASE measured between 500-850 ns of the 1 µs pulse.

Figure 3.4 shows a schematic diagram of the segmented contact stripes. Fabrication of segmented contact samples was carried out by Dr. Sara-Jayne Gillgrass. The samples featured Cr/Au (20/300 nm) p-contacts, 292 µm long and 100 µm wide with an 8 µm spacing, that was patterned

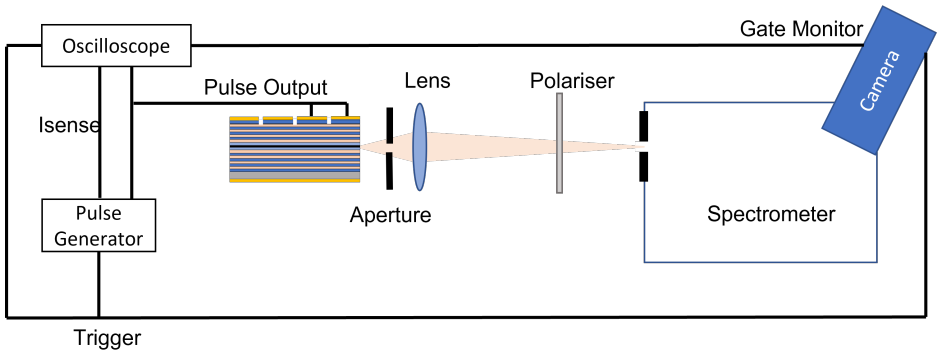

Figure 3.3: Schematic diagram showing the setup used for the segmented contact technique. The in-plane emission from the segmented contact stripe is free-space coupled into a spectrometer with a lens. An aperture is placed before the lens to limit the collection angle, and a polariser is used to select the TE polarised light.

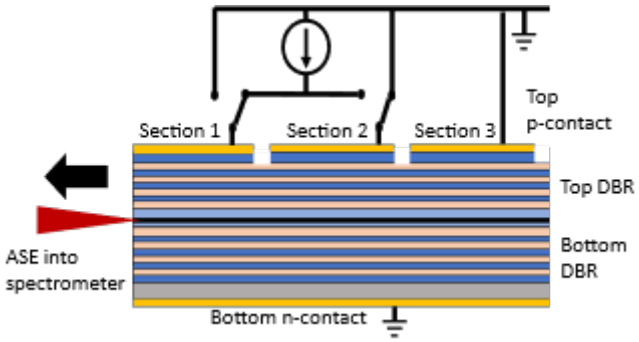

Figure 3.4: Schematic diagram of a segmented contact stripe fabricated on VCSEL material, showing three individual sections, defined by segmented p-contacts that are 292 µm long and 100 µm wide, with an 8 µm spacing. For the gain measurement, sections are electrically pumped with a current source. A switch box allows individual or multiple sections to pumped, and ensure any unpumped section are grounded. Light propagation occurs along the plane of the wafer and optical emission occurs at the facet of section 1. Figure from [93].

and annealed on GaAs cap layer. The cap and several Bragg layers were then wet etched, using the contacts as the mask, to increase the electrically resistance between each section. AuGe/Ni/Au contacts were deposited on the n-side, followed by a second annealing step. Wafer sections containing 2 or 4 stripes, that were 10 sections long, were cleaved and mounted onto a copper block on a gold 16-pin TO-header. The front 4 sections were each wire-bonded to separate pins, to allow them to be electrically driven independently. For the back 6 sections, multiple sections were wire-bonded to a single pin to allow for grounding as required.

3.3 VCSEL Device Characterisation

3.3.1 Temperature dependent measurements

For temperature dependent measurements, a copper mount was put into thermal contact with a ceramic heater plate using thermal paste, so that the sample could be heated from room temperature up to 80 °C. A thermistor, that was covered in thermal paste, was embedded in a hole within the copper mount, in close proximity to the sample. The heater plate was controlled by a Thorlabs proportional-integral-derivative temperature controller. 3D-printed washers, fabricated from a material with poor thermal conductivity, were used to thermally isolate the temperature mount from the translation stages. To eliminate any temperature offset due to the separation of the sample and the thermistor, the setup was calibrated using two calibrated platinum resistance thermometers (PT100) that had been epoxied onto a gold 16-pin TO-header.

3.3.2 Power-Current-Voltage

The optical power was measured using a Thorlabs Integrating sphere. The VCSEL devices were electrically driven with either a CW2401 Keithley or a low current, in-house current source that could be operated in either pulsed or continuous wave (CW) mode. The minimum pulse width the in-house current source could reliably output was 10 µs. The voltage was

only measured when the Keithley was used.

Multi-section devices were pumped with an in-house pulsed current source using a 1 µs pulse width and with either a 1 kHz or 5 kHz repetition frequency. This current source could output pulses with peak currents on the order of 1 A, and is different to the current source used to drive VCSEL devices. Due to the impedance mismatch, a large voltage spike was present at the start of the pulse. To avoid this spike, voltage and current values are taken after 500 ns, averaged over a 250-300 ns window.

The threshold current was determined from the peak position of the 2nd derivative of the P-I curve after smoothing the data with a linear Savitzky-Golay filter.

3.3.3 Wavelength

The emission wavelength of VCSEL devices was measured using an Ando optical spectrum analyser. An AR-coated lens was used to couple light into a multi-mode fibre with a graded 62.5 µm core which provided a minimum wavelength resolution of 0.1 nm.

3.3.4 Side-Mode Suppression-Ratio

An integrating sphere with an output port was used to collect the light and remove any spatial dependencies. The light output from the integrating sphere was free space coupled into the spectrometer with a CCD camera. Assuming the width of the modes are the same, the height will be proportional to the mode power. Due to broadening of the mode-widths by the spectrometer, this is likely to be a reasonable assumption. Ideally, single-mode VCSELs will lase at the fundamental transverse mode. A side mode suppression ratio (SMSR), defined as the logarithm of the ratio of the highest mode power and the 2nd highest mode power, was used to evaluate the single-mode performance of the device. With the settings used, a maximum SMSR of approximately 35 dB could be detected due to noise.

3.3.5 Polarisation

An anti-reflection (AR)-coated lens with a numerical aperture of 0.5 was used to collimate the VCSEL optical emission into an integrating sphere. A linear polariser was then positioned between the lens and the integrating sphere. The polariser was aligned so that the transmission was maximised at a given current, and a P-I curve was taken. The polariser was then rotated 90° and and a P-I curve was taken again. The orthogonal polarisation suppression ratio (OPSR) was defined as the logarithm of the ratio of the measured optical power, for the two orthogonal polarisations at a given current. The linear polariser had an extinction ratio of 30 dB, so that an OPSR of 20 dB would have an error of 0.4 dB.

3.3.6 Near-field

The near-field was obtained by using a microscope objective to project an image onto a GXCAM-U3-5 CMOS camera. The camera response is split into 256 levels. At levels above 150, the camera response becomes significantly non-linear, so ND filters were used to limit the maximum intensity of the near-field imaged onto the camera. A 50× microscope objective, with a numerical aperture of 0.42, was used to measure the nearfield of VCSEL devices. A 4× microscope objective, with a numerical aperture of 0.1, was used to image the vertical spontaneous emission profile of the multi-section devices (see section 5.4), that was used to estimate the current density profile at low current density.

3.3.7 Far-field

The far-field was characterised by a turn-table set-up originally built by Dr. Stella Elliot and refurbished by Dr. Richard Forrest. A VCSEL device is positioned at the centre while an integrating sphere with a 150 µm wide slit rotates around the device.

From the measured far-field profile, the variance σ_θ^2, and thus the $4\sigma_\theta$ beam divergence, was calculated using a converging 2nd moment method [94]. For a Gaussian far-field profile, the

$4\sigma_\theta$ beam divergence is equivalent to the $1/e^2$ full-width beam divergence.

3.3.8 Semi-automatic Wafer Prober

Some device measurements were performed using a semi-automatic wafer prober. A wafer or wafer piece is held in place by a vacuum, on a thermal chuck that can heat the sample from room-temperature to 200 °C, and acts as the ground for bottom n-contact devices. Tungsten tipped probes are used to power individual devices. The prober can translate the wafer in the $x - y$ direction, so that once aligned, different devices can be probed automatically. An integrating sphere can be installed for calibrated optical power measurements, with an output port that can be fibre coupled to a CCD spectrometer for wavelength measurements.

3.4 Conclusion

In this chapter, the experimental techniques that were used to characterise VCSEL material and devices were described. The segmented contact technique which is used to measure in-plane modal gain, and the experimental setups used to measure the power-current-voltage, wavelength, near-field and far-field were presented.

Chapter 4

Characterisation of VCSEL Devices for MACs

4.1 Introduction

This chapter characterises oxide-confined vertical-cavity surface-emitting laser (VCSEL) devices that were designed for use in miniaturised atomic clocks (MACs) that utilise Cesium (Cs) vapour cells. The MAC application has stringent requirements which are summarised in table 1.1. The VCSEL emission must be single-mode and linearly polarised, with no polarisation switching. While this has been achieved with surface grating VCSELs [17][21][22], they require additional processing steps and electron-beam lithography due to the small feature-size of the gratings. Non-circular oxide apertures, which require no additional processing steps, can introduce an anisotropy to ensure preferential lasing of a particular polarisation direction [24][25][26][28]. Here, by varying the shape and size of the VCSEL mesa, the shape and size of the oxide aperture is varied, and its influence on device performance is studied. The measured characteristics of the devices are compared to the requirements of the application to determine the optimum oxide dimension.

The cavity-resonance wavelength of the VCSEL epitaxial structure was shorter than intended by approximately 4-6 nm. While this might be acceptable for typical VCSEL applications which don't require such a tight specification on emission wavelength, for MAC applications, multiple calibration runs and systematic changes are required to meet the target wavelength. Although the intended device operating temperature for this application is 60-80 °C, alignment with the gain peak wavelength was predicted to occur below 0 °C, as shown in figure 4.7. Therefore, to evaluate the device performance with different oxide aperture geometries, unless otherwise specified, measurements are typically performed at room temperature (23 ± 1 °C) which was the lowest temperature that was convenient to access with the measurement tools.

4.2 Sample

The epitaxial structure was designed by Dr. Sam Shutts and wafers were grown by Compound Semiconductor Centre (CSC) Limited. Devices were fabricated by Sivers Photonics.

In this chapter, devices that were grown on a GaAs substrate, with a 1-λ thick cavity that contained three 5 nm thick $In_{0.082}Ga_{0.918}As$ quantum well (QW) layers within a graded AlGaAs separate confinement heterostructure (SCH), are considered. 20 and 34 $Al_{0.12}Ga_{0.88}As/Al_{0.9}Ga_{0.1}As$ distributed Bragg reflector (DBR) pairs, with graded interfaces, formed the p-doped top and n-doped bottom mirrors respectively. A 30 nm thick $Al_{0.98}Ga_{0.02}As$ layer, which could be oxidised to form an oxide aperture, was positioned just below the top DBR.

Devices had either a circular or an elliptical shaped mesa, to determine the impact of elliptical oxide apertures on the polarisation stability of the VCSEL optical output. Elliptical mesas had aspect ratios of 1.1, 1.3 and 2 (with circular mesas having an aspect ratio of 1). The minor diameter was varied from 20-30 µm in 1 µm steps. For elliptical mesa devices, the minor and major diameters were orientated along the [011] and [0$\bar{1}$1] axis. Over the wafer, the designs were repeated multiple times.

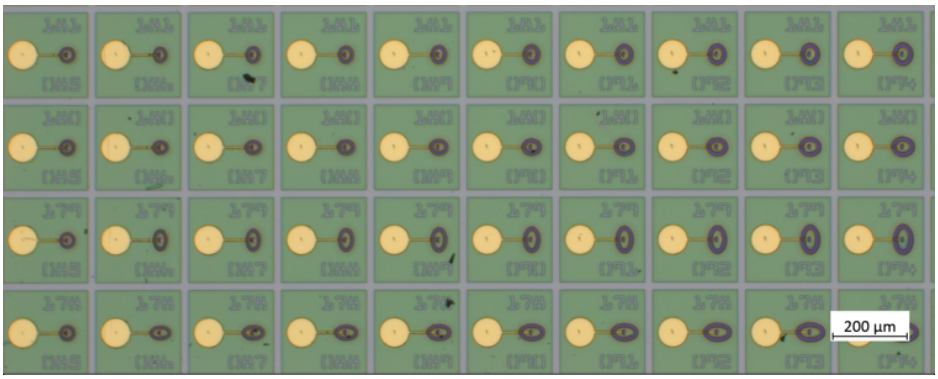

Figure 4.1: Microscope image showing a wafer section of fully fabricated VCSEL devices with a variety of mesa shapes and sizes. The leftmost column shows 25 µm diameter circular mesa devices. The remaining columns show elliptical mesa devices with minor diameters ranging from 20-28 µm, increasing in 1 µm steps from left to right. The bottom two rows show elliptical mesas with an aspect ratio of 2, and the top two rows show elliptical mesas with an aspect ratio of 1.3. For each aspect ratio, there are two rows, with the mesa orientated orthogonally.

Figure 4.1 shows a microscope image of a section containing 25 µm diameter circular mesa devices and 20-28 µm minor diameter elliptical mesa devices with aspect ratios of 1.3 and 2.

4.2.1 Oxide Aperture Geometry

Figure 4.3 shows the series conductance (or the reciprocal of the resistance) determined from I-V curves obtained by Dr Dave Hayes. The voltage was swept up to 2.5 V with a current compliance limit of 10 mA. The series conductance was found from the slope calculated using 3 datapoints at the highest measured voltages below the current compliance limit. Therefore, for the smallest and largest oxide aperture devices, the conductance values obtained may not have converged to the value at infinity, as either the voltage or current limit had been reached. The series conductance dependence on oxide aperture area A_{oxide} was described using an equation of the form [95]

$$G_{\text{series}} = \frac{1}{R_{\text{series}}} = \frac{1}{R_{\text{DBR}} + r_{\text{oxide}}/A_{\text{oxide}}} \tag{4.1}$$

where R_{series} is the series resistance, and R_{DBR} and r_{oxide} are fitting parameters. For large oxide aperture areas, the conductance is no longer limited by the oxide aperture but rather

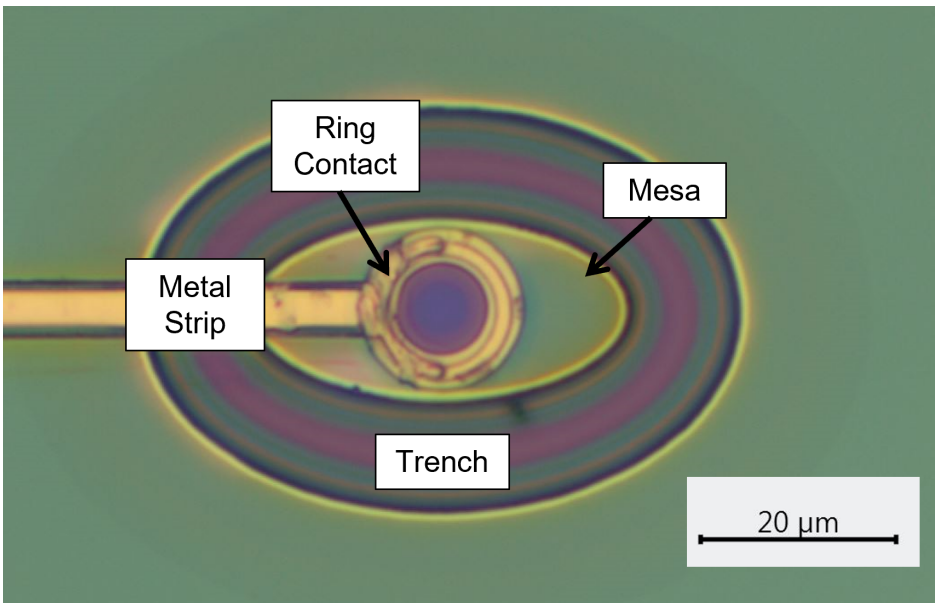

Figure 4.2: Microscope image of a 20 µm minor diameter, elliptical mesa device with an aspect ratio of 2. The mesa is defined by a trench etch. Ring contacts on the top surface are used to pump the device. A metal strip connects the ring contacts to the bond pad (out of frame) on the left. The device can be seen in figure 4.1 with co-ordinates (x=86, y=178).

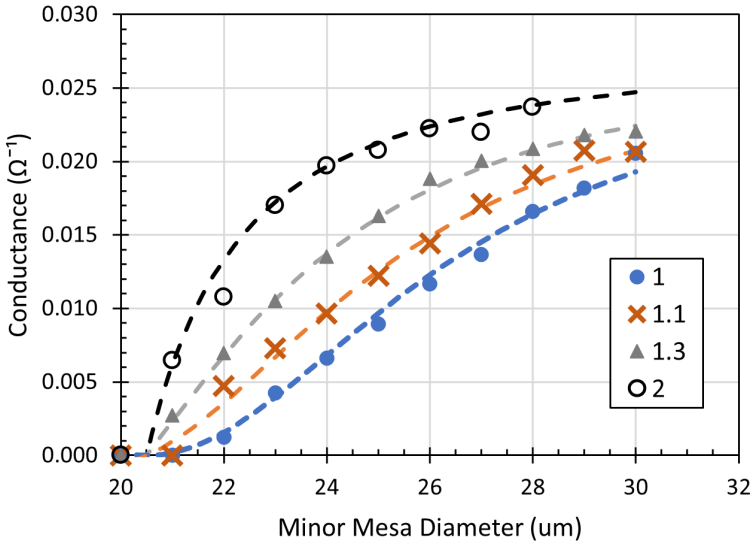

Figure 4.3: Series conductance plotted as a function of minor mesa diameter for mesa aspect ratios of 1 (blue circle), 1.1 (orange cross), 1.3 (grey triangle), and 2 (open circle), and corresponding fits to the data using equation 4.1.

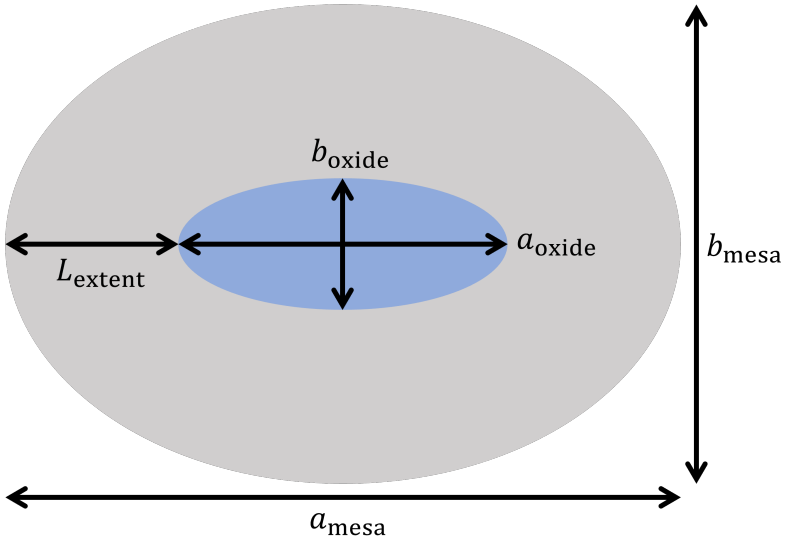

Figure 4.4: Schematic diagram showing the mesa and oxide aperture dimensions, where L_{oxide} is the oxidation extent, a_{mesa} and b_{mesa} are the mesa major and minor diameters, respectively, and a_{oxide} and b_{oxide} are the oxide aperture major and minor diameters, respectively.

by the contact area and the material, and tends to $1/R_{\text{DBR}}$.

For 1.3 and 2 aspect ratio mesa devices, the conductance goes to approximately zero when the minor mesa diameter is 20 µm due to a fully closed oxide aperture. This indicates the oxidation extent is 10.3 $\pm$ 0.3 µm, and is the value used to determine the oxide aperture diameter in the following chapter. On the other hand, for 1 and 1.1 aspect ratio mesa devices, this occurs when the diameter is 21 µm. It has previously been reported that the oxidation rate increases slightly, when the oxide aperture is about to close up [96][97][98]. For small oxide apertures with aspect ratios close to 1, this may mean the actual oxide aperture is smaller than the nominal value. Despite this, a reasonable fit to the data in figure 4.3 could be obtained with equation 4.1, where an oxidation extent of 10.3 µm was an input to the fit, and fitting parameters of $R_{\text{DBR}} = 37\ \Omega$, $r_{\text{oxide}} = 1058\ \Omega\mu\text{m}^2$ were used.

Figure 4.4 is a schematic diagram showing the oxide aperture dimensions of an elliptical mesa device. For a given mesa dimension, the oxide aperture dimension is determined by the oxidation extent. Neglecting devices with closed or almost closed oxide apertures, the oxidation extent is approximately the same for all devices on the wafer. Therefore, apart from circular oxide

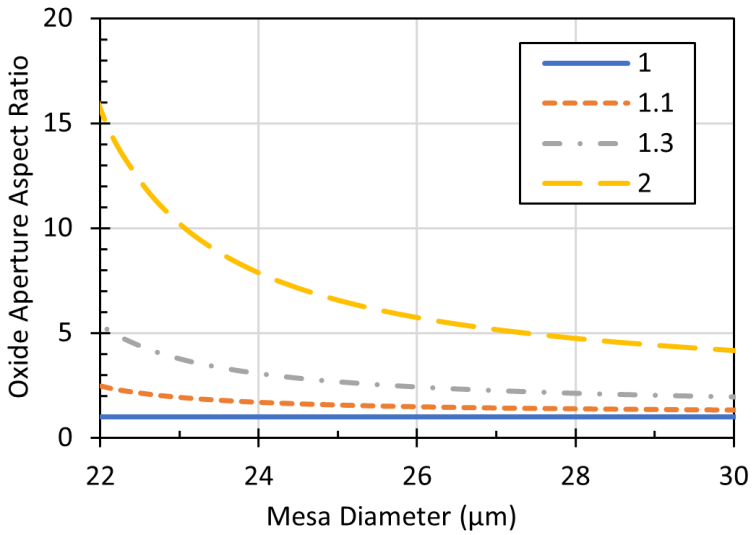

Figure 4.5: Oxide aperture aspect ratio as a function of mesa diameter for mesa aspect ratios of 1 (solid blue), 1.1 (short dash orange), 1.3 (dot/dash grey), and 2 (long dash grey). The oxide aperture aspect ratio was calculated for a given mesa diameter, using an oxidation extent of 10.3 µm

apertures, the aspect ratio of the oxide aperture differs from that of the mesa, and varies with the mesa diameter. This can be seen in figure 4.5, which shows the calculated oxide aperture aspect ratio for a given mesa diameter, assuming an oxidation extent of 10.3 µm. For smaller devices, the oxide aperture aspect ratio becomes significantly larger than the mesa aspect ratio.

A geometric mean oxide aperture diameter, d_{oxide}, given by equation 4.2, is used in this chapter.

$$d_{\text{oxide}} = \sqrt{a_{\text{oxide}} b_{\text{oxide}}} \tag{4.2}$$

where a_{oxide} and b_{oxide} are the major and minor diameters of the oxide aperture, respectively. The geometric mean diameter is proportional to the square root of its area, so devices with differing aspect ratios can be compared whilst accounting for any size dependent scaling of device characteristics.

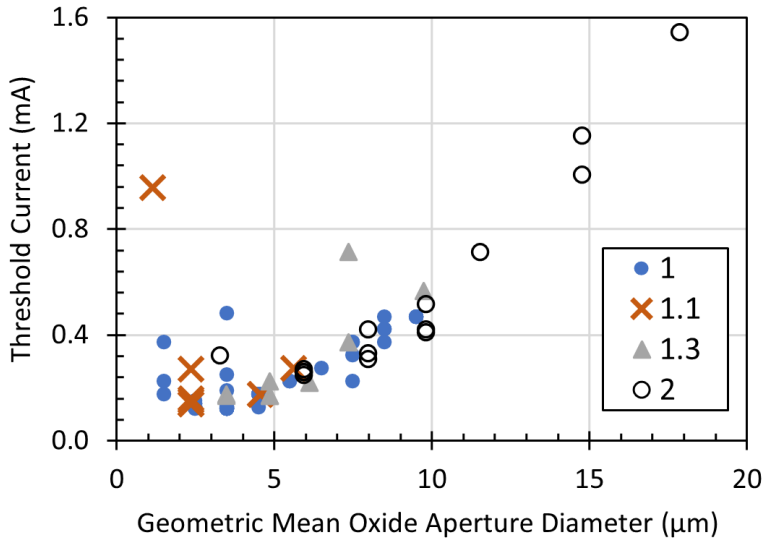

Figure 4.6: Threshold current as a function of geometric mean oxide aperture diameter for mesa aspect ratios of 1 (blue circle), 1.1 (orange cross), 1.3 (grey triangle), 2 (open circle)

4.3 Lasing Threshold

Figure 4.6 shows the measured threshold current as a function of geometric mean oxide aperture diameter. The minimum threshold value of 0.12 $\pm$ 0.01 mA was measured for a nominally 2.5 µm and 3.5 µm oxide diameter device. For large oxide apertures, the threshold current scales with the pumped area and increases quadratically with the geometric mean diameter. However, when the oxide aperture diameter is on the order of a few microns, self-heating and higher optical losses increase significantly, and the threshold current increases as the oxide aperture diameter is reduced. Regardless of the aspect ratio, within the scatter, the threshold current appears to have the same dependence on the geometric mean oxide aperture for the majority of datapoints. This suggests that for a given oxide aperture area, optical losses don't vary significantly with the oxide shape. Additionally, for larger area devices that are multi-mode, the overlap of the mode with the active area is likely to be close to one regardless of the aperture shape.

Figure 4.7 shows the temperature dependence of the threshold current for two circular mesa devices. Typically, there is a temperature where the the threshold current is a minimum due

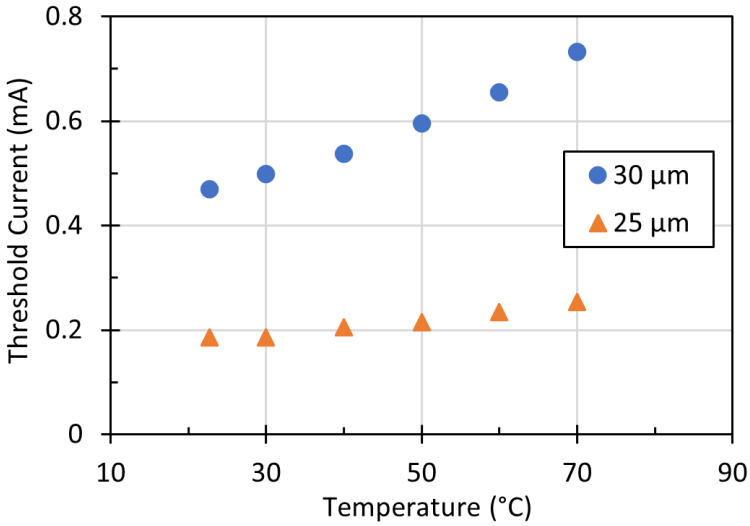

Figure 4.7: Threshold current as a function of temperature for two circular mesa devices with mesa diameters of 30 µm (blue circle) and 25 µm (orange triangle). These correspond to oxide diameters of 9.5 µm and 4.5 µm respectively. The devices were operated CW. The solid lines show the 2nd order polynomial fits to the data.

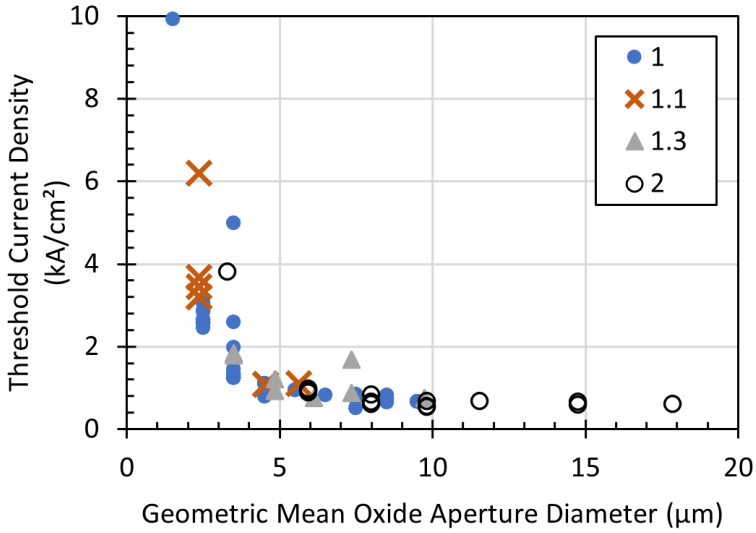

Figure 4.8: Threshold current density as a function of geometric mean oxide aperture diameter for mesa aspect ratios of 1 (blue circle), 1.1 (orange cross), 1.3 (grey triangle), 2 (open circle)

to alignment of the vertical cavity mode with the gain-peak. However, for both devices, the threshold current monotonically increases with temperature and no minima can be seen. This suggests that either the alignment of the gain-peak wavelength and cavity resonance wavelength occurs at temperatures below room temperature, or that non-radiative recombination processes, which have a strong temperature dependence, dominate the threshold current. Given that the emission is below 1 µm, it is likely to be the former.

Figure 4.8 shows the measured threshold current density as a function of the geometric mean oxide aperture diameter. The active area is taken to be equal to the oxide aperture area and it is assumed that current spreading is negligible due to the proximity of the oxide layer with the active layers. There is a much greater uncertainty for smaller devices where fluctuations in the oxide diameter have a proportionally much larger effect on the area. With increasing oxide aperture diameter, the threshold current density tends to a value of approximately 0.6 kA/cm^2. For oxide aperture diameters below 4.5 µm, the threshold current density increases significantly. It is likely that the increase is due to greater scattering losses and self-heating.

4.4 Optical Power

Figure 4.9 shows a power-current curve of a 21 µm minor diameter, elliptical mesa device with an aspect ratio of 1.1. Thermal rollover is when the optical output power "rolls over" due to the self-heating. It was evaluated by taking the maximum measured optical power, and for the device shown, the thermal rollover power was 0.53 mW and occurred at 3.85 ± 0.05 mA.

Figure 4.10 shows the optical output power at thermal rollover. Devices with mesa aspect ratios of 1, 1.1, and 1.3 appear to lie on the same linear curve. On the other hand, devices with a mesa aspect ratio of 2 do not lie on this curve, and have lower optical powers due to the ring contacts blocking the emission. A linear curve with a slope of 1.05 ± 0.05 mW/µm was obtained from an empirical fit to the 1, 1.1, and 1.3 mesa aspect ratio device data. The fit indicates that devices with geometric mean oxide diameters of 2 µm have maximum optical

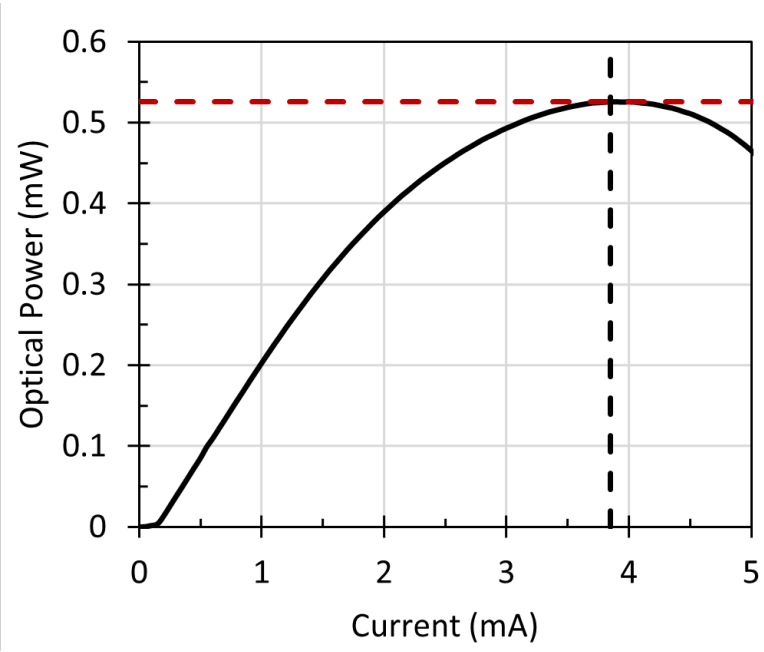

Figure 4.9: Power-current curve for a 21 µm minor diameter, elliptical mesa device with an aspect ratio of 1.1. The nominal oxide aperture dimension is 1.5×3.7 µm, which corresponds to a geometric mean diameter of 2.1 µm. The device had a threshold current 0.15 ± 0.05 mA. The thermal rollover power (horizontal red dashes) was measured to be 0.53 mW, and occurred at a current (vertical black dashes) of 3.85 ± 0.05 (mA).

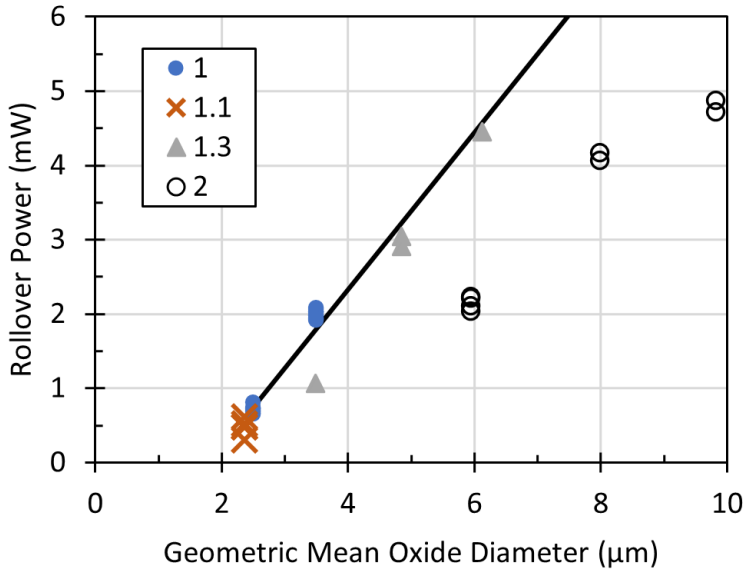

Figure 4.10: Optical output power at thermal rollover as a function of geometric mean oxide diameter for mesa aspect ratios of 1 (blue circle), 1.1 (orange cross), 1.3 (grey triangle), 2 (open circle). The solid black line is an empirical fit, with a linear curve, to the 1, 1.1, and 1.3 mesa aspect ratio device data.

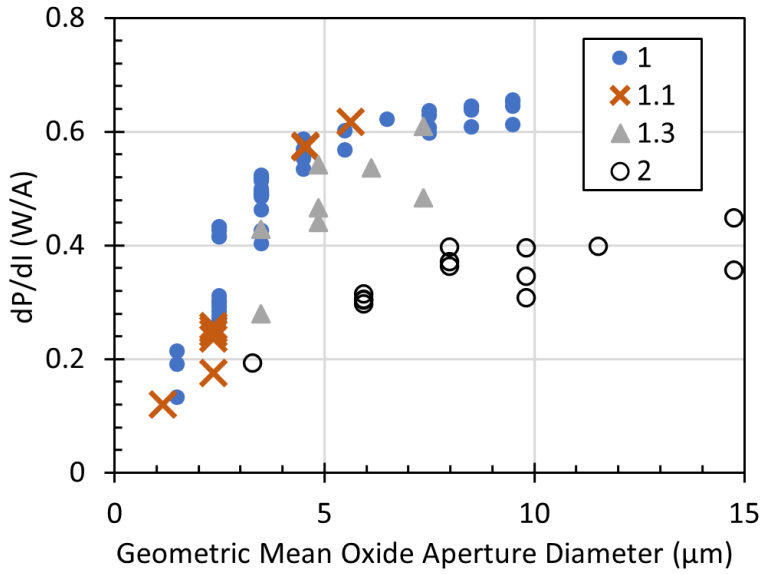

Figure 4.11: Slope efficiency as a function of geometric mean oxide aperture diameter for mesa aspect ratios of 1 (blue circle), 1.1 (orange cross), 1.3 (grey triangle), 2 (open circle). The slope efficiency values shown are the maximum measured value just above the threshold current. Devices were operated continuous wave.

powers of 0.2 mW.

Figure 4.11 shows the slope efficiency as a function of geometric mean oxide aperture diameter. Assuming constant injection efficiencies and mirror losses, the slope efficiency gives an indication of the additional optical loss, with higher optical losses leading to lower slope efficiencies (see section 2.9). Since these devices were operated in continuous wave (CW), self-heating effects will also reduce the slope efficiency. For circular oxide apertures, it is clear the slope efficiency increases with increasing aperture size, and the mean slope efficiency is 0.18 ± 0.02 W/A for a nominally 1.5 µm oxide diameter, and 0.56 ± 0.01 W/A for a nominally 4.5 µm oxide diameter. The rate at which the slope efficiency increases reduces with increasing oxide aperture diameter, and the mean slope efficiency value is 0.64 ± 0.01 W/A for a nominally 9.5 µm circular oxide diameter. For 2.5 µm and 3.5 µm oxide diameters, there appears to be two distinct distributions which correspond to devices from two different regions. Devices from one region has mean slope efficiencies of 0.424 ± 0.004 W/A and 0.520 ± 0.001 W/A, for 2.5 µm and 3.5 µm oxide diameters, respectively, while devices from the other region have

values of 0.287 ± 0.006 W/A and 0.477 ± 0.009 W/A, for 2.5 µm and 3.5 µm diameter oxide apertures, respectively. Devices from one region have a lower slope efficiency than the other, and this is likely due to a slightly smaller oxide aperture diameter. The fact that the mean slope efficiency values lie at around the mid-point of values of smaller and larger devices from the other region suggests it is smaller by approximately 0.5 µm which is within the expected uncertainty. For all other circular oxide diameters, devices are from the region with a higher external efficiency.

The figure appears to indicate that the 1.3 mesa aspect ratio devices have slightly lower slope efficiencies. Devices with a mesa aspect ratio of 2 have much lower slope efficiencies that tends to a value of 0.38 ± 0.01 W/A, as the metal contact is partially blocking the emission (as shown in figure 4.12).

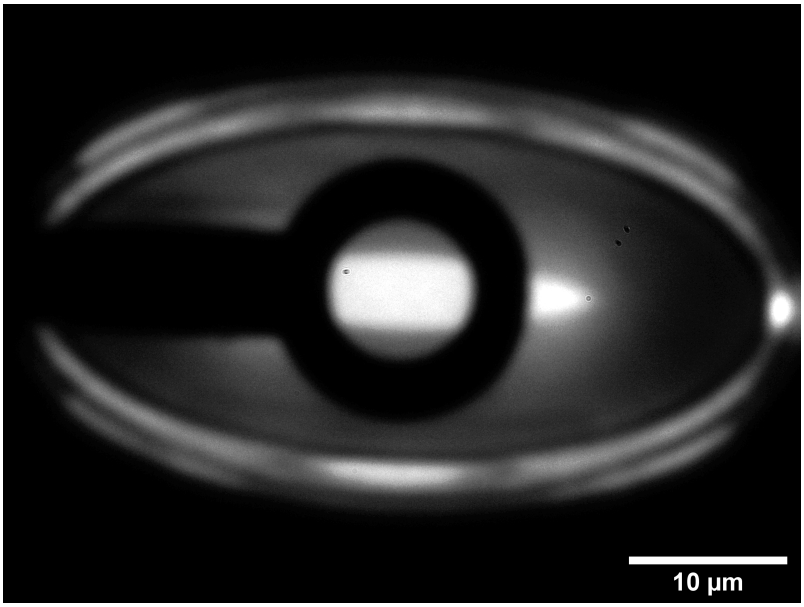

Figure 4.12: Sub-threshold near-field of a 25 µm minor diameter, elliptical mesa VCSEL device with an aspect ratio of 2. The nominal oxide aperture dimensions are 4.5×29.5 µm. The outline of the elliptical mesa can be seen due to light scattered out of the edge of the mesa. Spontaneous emission from the pumped region, determined by the elliptical oxide aperture. An annular shadow can be seen due to the metallic ring contact partially blocking the emission. The contrast has been increased.

As shown in table 1.1, a slope efficiency below 0.2 W/A is desirable, with a maximum limit of 0.4 W/A. For this epi-structure, this can be achieved with a geometric mean oxide aperture

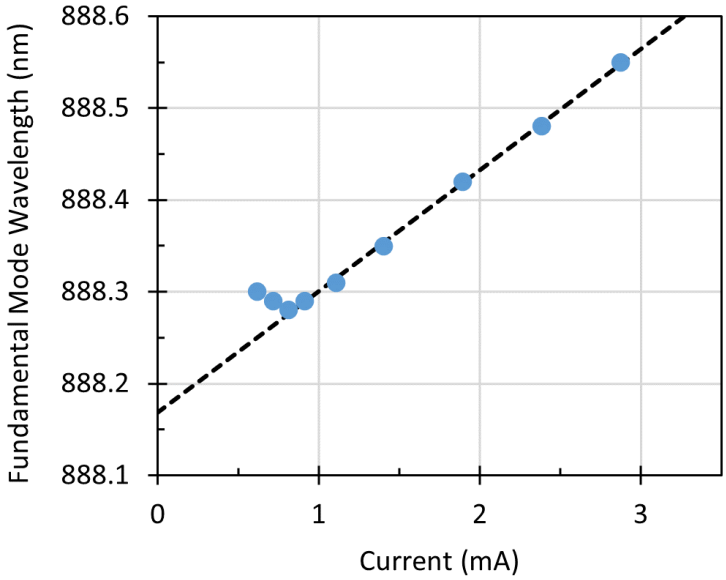

Figure 4.13: Fundamental mode wavelength as a function of current for an elliptical mesa VCSEL with a 26 µm minor diameter and an aspect ratio of 2.

diameter of 3 µm. The slope efficiency will reduce with increasing current as it approaches thermal rollover, so depending on the operating conditions, a slope efficiency of below 0.4 W/A could be achieved with a larger aperture.

4.5 Emission Spectra

Figure 4.13 shows the fundamental mode wavelength as a function of injection current for a 26 µm minor mesa diameter elliptical device. Below threshold, the wavelength shifts due to a combination of self-heating induced refractive index change and carrier induced refractive index change. The blueshift indicates the carrier induced refractive index effect is dominant. At the lasing threshold and above, the carrier density in the active region clamps, and only the temperature induced redshift is seen. The current tuning coefficient was determined from the slope of a linear fit to the measured wavelength above threshold. The y-intercept should give the fundamental mode wavelength without the presence of self-heating effects, at 23 °C. As mentioned in section 2.10, the temperature shift (and thus the wavelength shift) is proportional to the power dissipated by the device. For small injection currents, the total power dissipated

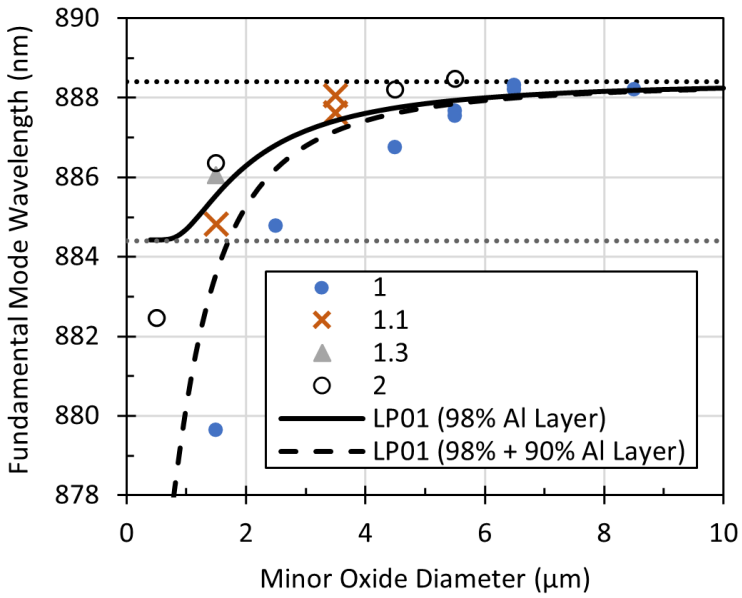

Figure 4.14: Wavelength of the fundamental mode as a function of the minor mesa diameter for mesa aspect ratios of 1 (blue circle), 1.1 (orange cross), 1.3 (grey triangle), 2 (open circle). The wavelength was determined from the y-intercept of a linear fit similar to that shown in figure 4.13. The horizontal dotted lines show the cavity-resonance wavelengths of 884.4 nm and 888.4 nm in the oxidised and unoxidised regions, respectively. The wavelength shift of 4 nm due to the oxidation of the $Al_{0.98}Ga_{0.02}As$ layer was calculated using the transfer matrix method. The LP01 fundamental mode wavelength was calculated using the effective index method (see section 2.11.1). The solid black line shows the calculated LP01 mode wavelength if only the $Al_{0.98}Ga_{0.02}As$ layer was oxidised, while the dashed black line shows the calculated LP01 mode wavelength if an adjacent $Al_{0.90}Ga_{0.10}As$ layer was also oxidised.

will be dominated by recombination at the diode junction and the wavelength will vary linearly with current. For smaller devices, which have higher series resistances, the resistive power dissipation will increase at a faster rate, so that the current dependent wavelength shift will become non-linear at lower currents.

Figure 4.14 shows the fundamental mode wavelength as a function of the minor oxide aperture diameter. For the circular oxide aperture devices, the lasing wavelength appears to tend to a value of 888.2 ± 0.1 nm at large aperture diameters, and the wavelength blueshifts with decreasing oxide aperture diameter. For a 1.5 µm diameter oxide aperture, the fundamental mode wavelength is 879.3 ± 0.1 nm, a blueshift of almost 9 nm. The acceptable tolerance for the emission wavelength is much larger (e.g. ±5-10 nm) in typical VCSEL applications

compared to atomic sensors where the atomic transitions are probed. To ensure the target lasing wavelength of 894.6 nm is obtained, this blueshift needs to be compensated for by shifting the vertical cavity-resonance wavelength of the epitaxial structure to a longer wavelength (in addition to correcting for the wavelength shift due to the growth). For small oxide aperture diameters, a large variation in the lasing wavelength might also be expected, reducing the yield.

Also shown are wavelengths simulated using the effective index method (see section 2.11.1). The horizontal dotted lines show the vertical cavity resonance wavelengths that were used in the effective index method. When just the 30 nm thick, 98 % Al concentration, AlGaAs layer was oxidised, values of 888.4 nm and 884.4 nm were used for the unoxidised and oxidised region, respectively. The transfer matrix method outlined in section 2.8.1 was used simulate the cavity resonance blueshift due to oxidation. A vertical cavity resonance wavelength of 886.0 nm and 882.0 nm was calculated for the unoxidised and oxidised region, respectively, at room temperature, giving a blueshift of 4 nm. This simulated room temperature vertical cavity resonance wavelength, for the unoxidised region, did not give good agreement with the measured wavelength values for large oxide aperture diameter devices. This is expected as deviations of several nm in the cavity resonance wavelength, due to composition and thickness variations, are typical. Therefore, the simulated vertical cavity resonance wavelengths were shifted by +2.4 nm, and it was assumed that the 4 nm blueshift due oxidation of the 98 % Al concentration layer remained the same. The black solid line shows the fundamental LP01 mode wavelength that was then calculated using the effective index method. If the mode is simply guided by an oxide aperture that's formed by partial oxidation of the $Al_{0.98}Ga_{0.02}As$ layer, 4 nm would be the maximum expected blueshift. However, the measured blueshift for the smallest device is much larger, and this is attributed to the additional oxidation of an adjacent 30.5 nm thick $Al_{0.90}Ga_{0.10}As$ layer. The transfer matrix method gave a vertical cavity resonance wavelength of 872.4 nm (before applying the +2.4 nm shift), giving a blueshift of 13.6 nm. The black dashed line gives the corresponding LP01 mode wavelength, and better

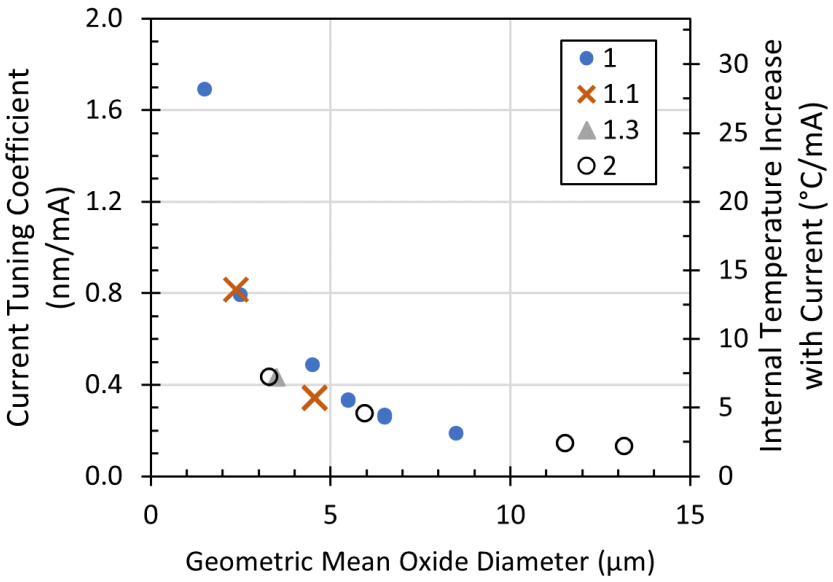

Figure 4.15: Current tuning coefficient (left axis) as a function of the geometric mean oxide aperture for mesa aspect ratios of 1 (blue circle), 1.1 (orange cross), 1.3 (grey triangle), 2 (open circle). Also shown is the corresponding internal temperature increase (right axis) with current.

agreement with the measured fundamental mode wavelengths for the circular oxide aperture devices is seen.

A similar blueshift of the fundamental mode wavelength with decreasing aperture size is also seen for the elliptical mesa devices. However, the blueshift is smaller, as the major aperture diameter is larger for a given minor diameter, so the mode is less confined.

Figure 4.15 shows the current tuning coefficient of the fundamental mode wavelength. The plot indicates that the aperture shape does not have a significant effect on the current tuning coefficient. For a geometric mean oxide aperture diameter of 13.2 µm, which corresponds to a 5.5×31.5 µm aperture, the temperature tuning coefficient is 0.13 nm/mA. This increases with decreasing oxide aperture size, and a value of 1.72 nm/mA is seen for a circular oxide diameter of 1.5 µm. The plot suggests that a geometric mean oxide aperture diameter of approximately 3 µm would give the ideal current tuning coefficient of 0.6 nm/mA specified in table 1.1.

Pulsed temperature dependent wavelength measurements give a temperature tuning coefficient of 0.06 nm/°C. For a 1.5 µm oxide aperture device, the internal temperature increase with current is approximately 28 °C/mA. Therefore, for the smallest devices, the self-heating is quite severe which limits the performance.

Figure 4.16 shows the measured side-mode suppression ratio (SMSR). At 0.2 mW, the 1.5x3.7 µm devices show greater than 30 dB single-mode operation. When the major diameter is increased to 8.1 µm, the device no longer exhibits single mode behaviour. The sample did not contain any devices with a major diameter between 3.7 µm and 8.1 µm so the dimensions at which point the devices no longer operate in single-mode can't be resolved in more detail. There was also no circular 1.5 µm oxide diameter devices that could have their SMSR characterised before device failure. For the 2.5 µm minor diameter devices, all but one of the 8 measured 2.5×2.5 µm aperture devices had an SMSR greater than 30 dB. For the 3.5 µm minor diameter devices, out of the 12 3.5×3.5 µm devices measured, only one exhibited an SMSR that was greater than 30 dB, with a minimum value of 26 ± 3 dB

Some of the 2.5×2.5 µm and the 1.5×3 µm aperture devices could not output 0.5 mW before reaching thermal rollover. However, those that could had an SMSR that was greater than 30 dB. The 3.5×3.5 µm circular oxide aperture devices showed a large variation in the measured SMSR, with values between 11 ± 3 dB and 29 ± 3 dB.

There were no devices that exhibited greater than 30 dB SMSR that could output optical powers of 1 mW. There is still a large variation in the SMSR of the circular 3.5 µm devices, which had measured values between 9 ± 3 dB and 28 ± 3 dB, and suggests 3.5 µm is at the boundary of circular oxide diameter values where single-mode performance can be obtained. All other devices characterised were multi-mode.

Table 1.1 specifies that a SMSR greater than 30 dB, with a minimum optical power of 0.2 mW, is required for the MAC application. This could be achieved with 2.5 µm and 3.5 µm diameter circular oxide apertures and 1.5×3.7 µm elliptical oxide apertures, although some of the 2.5 µm

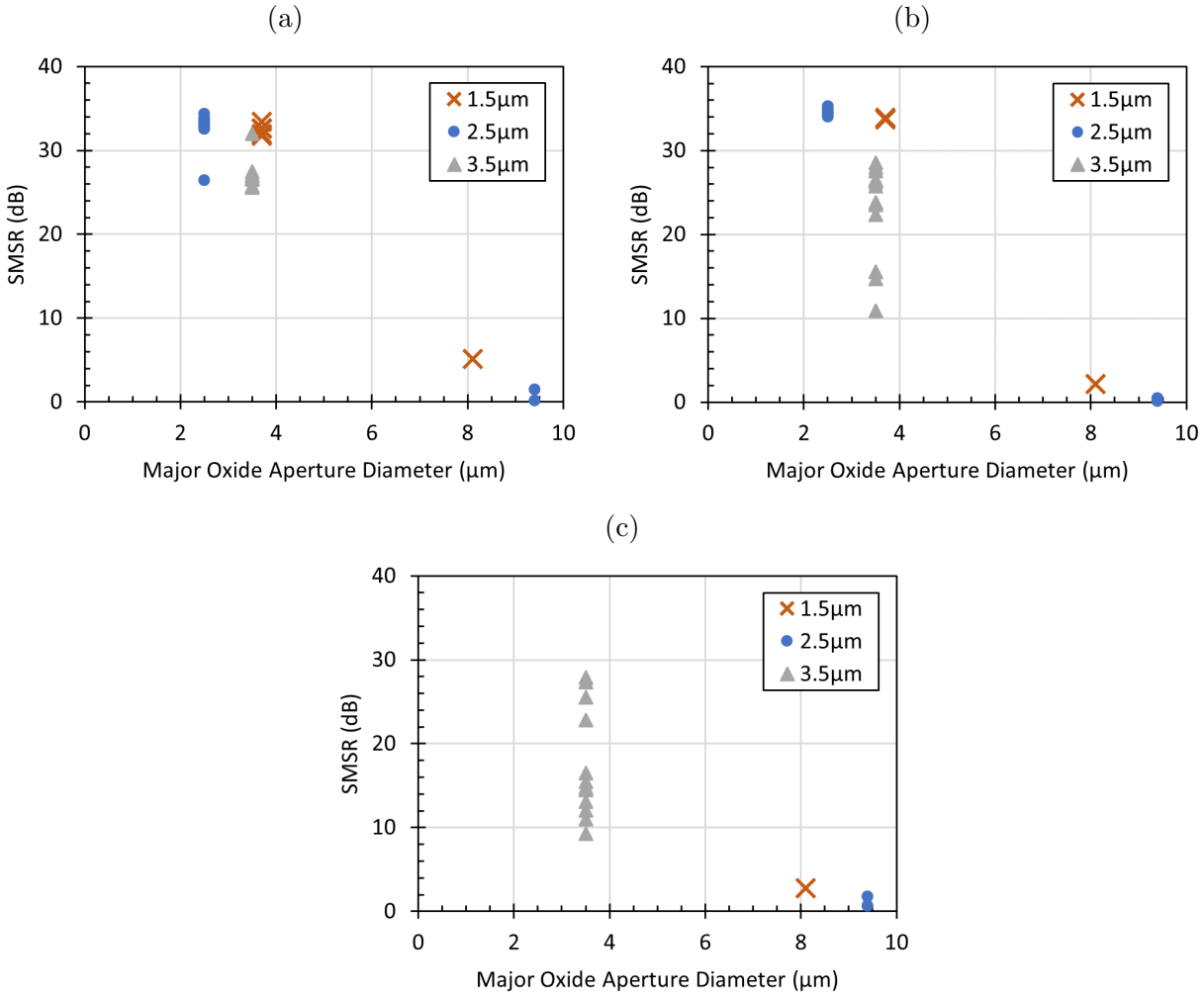

Figure 4.16: Side-mode suppression ratio (SMSR) as a function of major oxide aperture diameter for optical output powers of (a) 0.2mW, (b) 0.5mW, and (c) 1.0mW. Devices had minor oxide aperture diameters of 1.5 µm (orange cross), 2.5 µm (blue circle), and 3.5 µm (grey triangle). As mentioned in section 3.3.4, the maximum measurable SMSR was limited to approximately 35 dB due to the noise level

and 3.5 µm diameter circular oxide aperture devices had an SMSR below the required 30 dB. At the target optical power of 0.5 mW, 2.5 µm diameter circular oxide aperture devices and 1.5×3.7 µm elliptical oxide aperture devices could achieve greater than 30 dB single-mode operation.

4.6 Beam Quality

Figures 4.17 a and b shows the measured divergence angle along the minor and major axis of the aperture respectively. From figure 4.17a, it can be seen that the divergence angle along the minor axis is mostly independent of the major axis diameter, although when the major axis is small, the minor axis divergence appears to increase slightly for the 1.5 µm and 2.5 µm minor oxide diameter devices. This might be a result of thermal lensing reducing the beamwidth of the mode slightly. The mean full-width divergence angle was 73 ± 3°, 47 ± 2°, and 33 ± 0.5° for 1.5 µm, 2.5 µm, and 3.5 µm minor diameter oxide apertures, respectively, and shows that the divergence angle decreases with increasing oxide aperture diameter.

Figure 4.17a shows the divergence angle along the major axis. The general trend is that the divergence angle decreases with increasing oxide diameter. However, once the apertures are large enough, the device will no longer be single mode, and higher order modes with non-Gaussian profiles will also be lasing, which will increase the beam divergence. Figure 4.18 shows the near-field of a 1.5×23.5 µm oxide aperture device at 0.2 mW. Multiple peaks are present along the major axis due to the lasing of higher order modes. Additionally, for oxide aperture diameters of around 10 µm and larger, the beam is cut off at the edge due to the 10 µm diameter apertures of the metal ring contacts and the divergence angle is further increased. None of the devices characterised here have the required divergence angle of below 25°. Assuming an ideal Gaussian beam profile, this would require a near-field beamwidth of 2.6 µm.

It can be seen from figure 4.19a that the minor axis beam propagation factor (BPF) appears to remain constant with a changing major axis diameter. For the 3.5 µm minor diameter

(a)

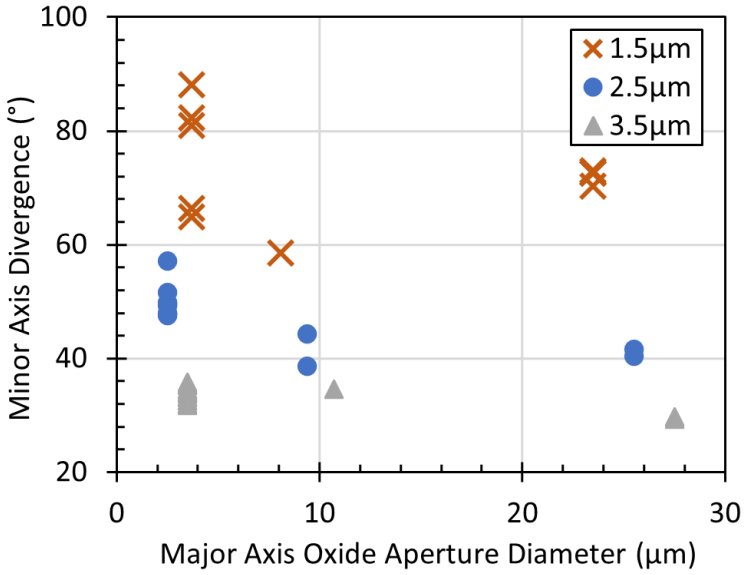

(b)

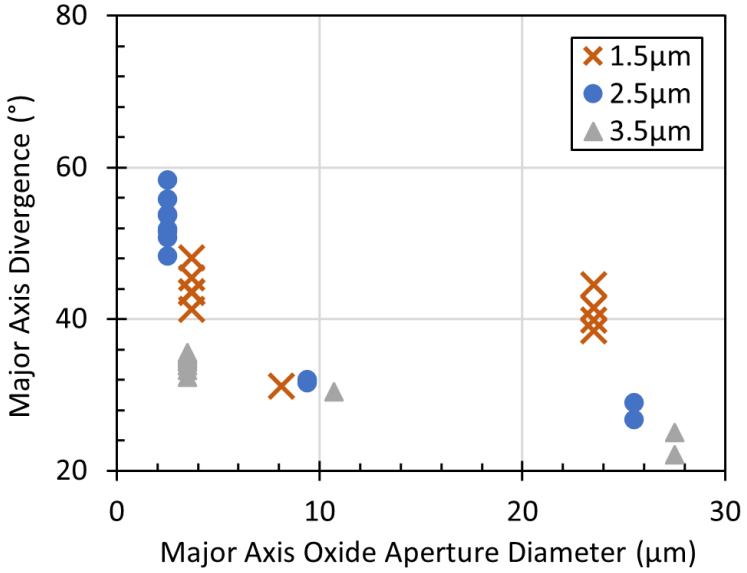

Figure 4.17: Measured divergence angle measured along the (a) minor and (b) major axis of the oxide aperture, for optical output powers of 0.2 mW. For circular oxide apertures, the minor and major axis was arbitrarily assigned. Devices had minor oxide aperture diameters of 1.5 µm (orange cross), 2.5 µm (blue circle), and 3.5 µm (grey triangle).

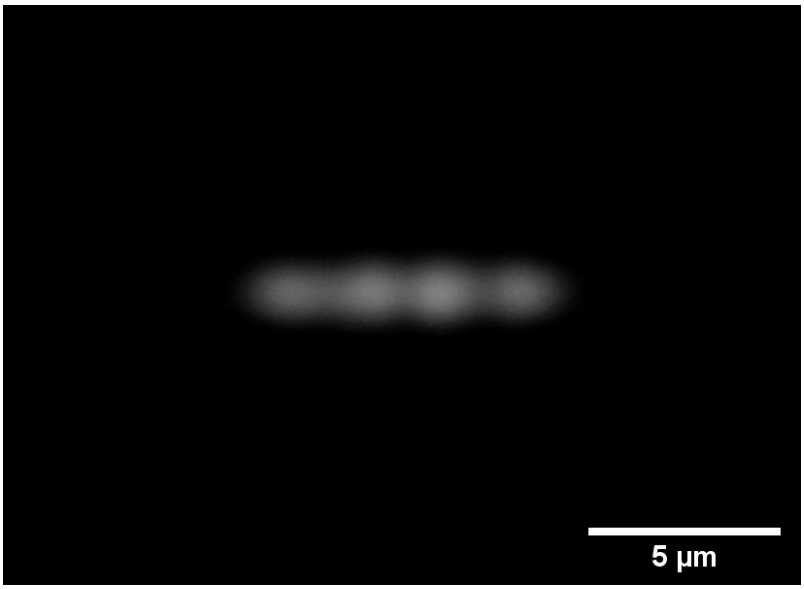

Figure 4.18: Near-field of a 22 µm minor diameter, elliptical mesa VCSEL device with an aspect ratio of 2. The oxide aperture dimensions are 1.5×23.5 µm

apertures, the mean measured BPF is 1.09 ± 0.02, and indicates it is close to an ideal Gaussian beam. The 2.5 µm and 1.5 µm minor diameter devices have a mean BPF of 1.35 ± 0.03 and 1.98 ± 0.08, respectively. With decreasing minor oxide aperture diameter, the mode profile along the minor axis deviates from the ideal Gaussian profile.

From figure 4.19b it can be seen that the major axis BPF generally increases with increasing major oxide diameter due to the presence of higher order modes with non-Gaussian profiles. Single mode devices with major oxide aperture diameters below 4 µm have a BPF of around 1-1.5. The 1.5×8.1 µm device also has a comparatively low BPF of 1.5, as compared to the fundamental mode, the higher order mode with the next highest optical power is 10 times weaker, so the beam profile is still predominantly Gaussian. The 3.5×3.5 µm circular aperture devices have the lowest measured BPF with a mean value of 1.10 ± 0.02.

4.7 Polarisation

Figure 4.20 a and b shows the minimum and maximum orthogonal polarisation suppression ratio (OPSR) measured between optical output powers of 0.2 mW and 0.5 mW, or up to

(a)

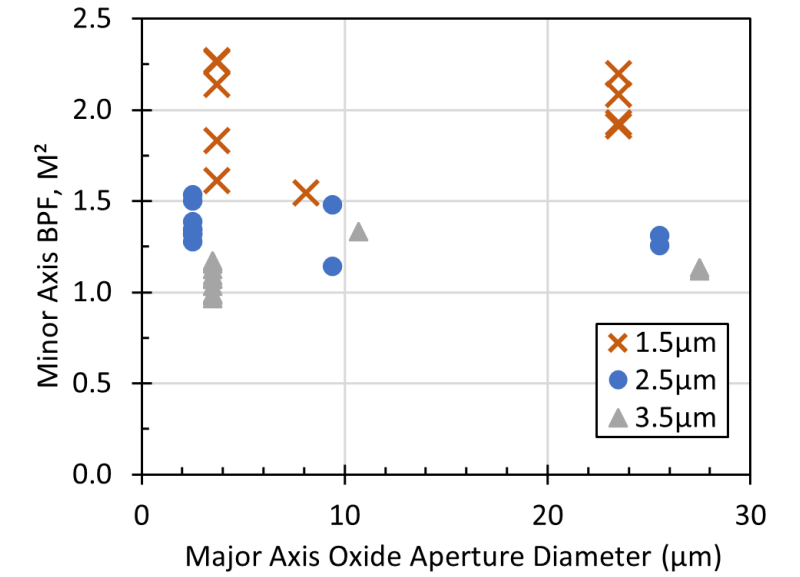

(b)

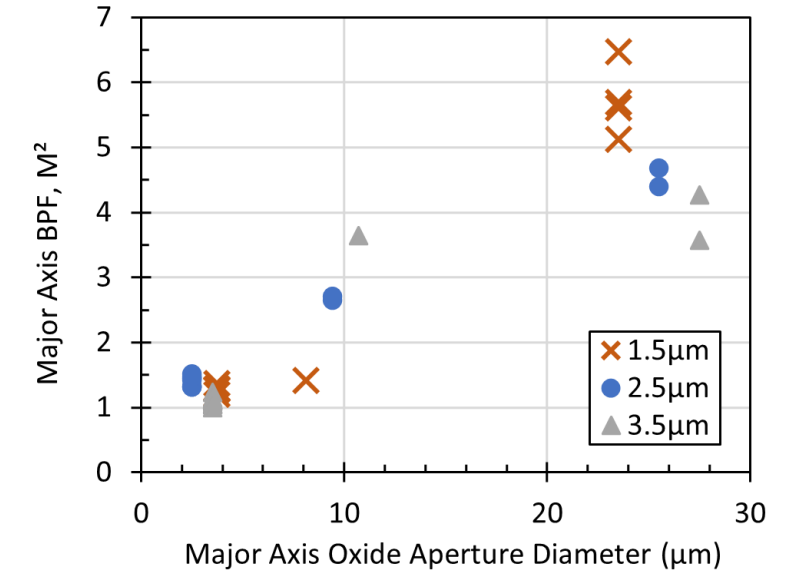

Figure 4.19: BPF or M^2 measured along the (a) major and (b) minor axis of the oxide aperture. For circular oxide apertures, the minor and major axis was arbitrarily assigned. Devices had minor oxide aperture diameters of 1.5 µm (orange cross), 2.5 µm (blue circle), and 3.5 µm (grey triangle).

(a)

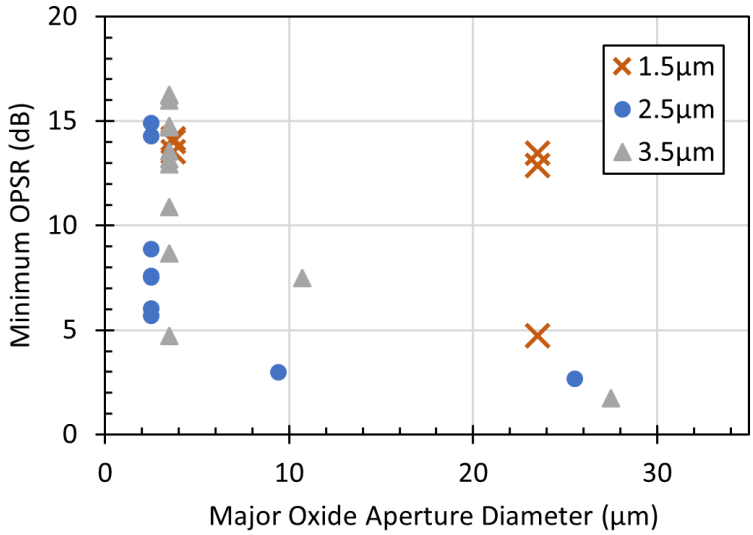

(b)

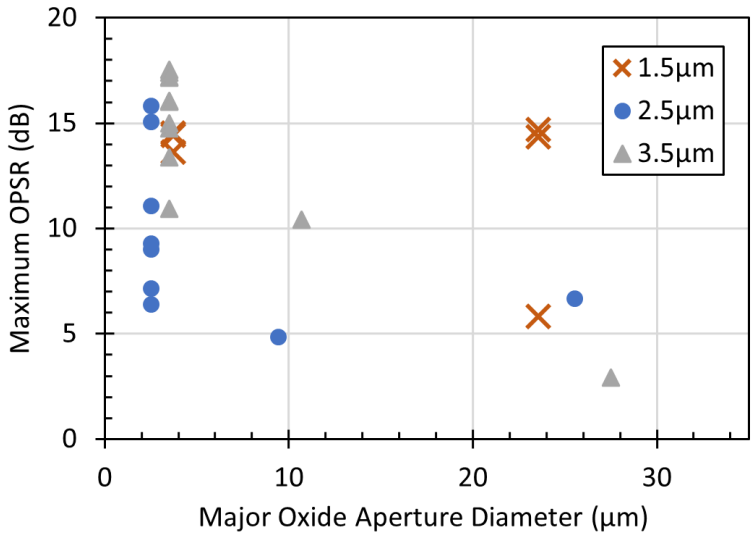

Figure 4.20: (a) Minimum and (b) maximum orthogonal polarisation suppression ratio (OPSR) as a function of the major oxide aperture diameter, between optical output powers of 0.2 mW and 0.5 mW. Devices had minor oxide aperture diameters of 1.5 µm (orange cross), 2.5 µm (blue circle), and 3.5 µm (grey triangle). For devices that could not output 0.5 mW, the OPSR was measured up to the rollover power

the thermal rollover power for devices that could not output 0.5 mW. Both the 2.5 µm and 3.5 µm circular aperture devices show a large variation in the measured OPSR which indicates some sensitivity to random variations. For the 2.5 µm circular aperture devices, the maximum measured OPSR varied between 6.4 ± 0.5 dB and 15.8 ± 0.5 dB with a mean value of 10.6 ± 1.4 dB, while for the 3.5 µm circular aperture devices, it varied between 10.9 ± 0.5 dB and 17.5 ± 0.5 dB with a mean value of 15.6 ± 0.6 dB. For the 2.5 µm circular diameter devices, the minimum measured OPSR was on average 1.3 dB lower than its maximum value. For the 3.5 µm diameter devices, the minimum OPSR was lower by around 2.7 dB on average, with some values lower by up to 6.2 dB due to appearance of higher order modes. For both the 2.5 µm and 3.5 µm minor diameters, when the major oxide diameter is increased, there is no obvious improvement in the maximum OPSR and instead appears to decrease.

For the 1.5 µm minor aperture diameter device, when the major aperture diameter is 3.7 µm, the maximum OPSR varied between 13.6 ± 0.5 dB and 14.5 ± 0.5 dB with a mean value of 14.2 ± 0.3 dB. The small variability would suggest this aperture dimension is tolerant to small variations. Additionally, the minimum OPSR differs from the maximum values by less than 0.4 dB for all the devices, indicating polarisation stability over this range. For a 23.5 µm major diameter, the maximum OPSR varied between 5.8 ± 0.5 dB and 14.7 ± 0.5 dB with a mean value of 11.6 ± 2.9 dB. Again, the overall OPSR seems to worsen when the major diameter becomes very large.

Increasing the oxide diameter along one dimension does not necessarily improve the OPSR. For many of the devices here, the major axis diameter is large enough that the devices become multi-mode, where some higher order modes, with an orthogonal polarisation, are preferable for lasing which complicates things. If the major axis is short enough that the device remains single mode it is likely to have a positive impact on the polarisation stability.

4.8 Optimum Oxide Aperture Geometry

For the epi-structure considered in this chapter, devices with 2.5 µm diameter oxide apertures met most of the requirements. The optimum circular oxide aperture diameter appears to be approximately 3 µm. From figure 4.6, a minimum threshold current of 0.12 ± 0.01 mW was measured for 2.5 µm and 3.5 µm circular oxide aperture diameter devices. To meet the minimum power requirement of 0.2 mW, figure 4.10 shows that an oxide aperture diameter of 2.0 ± 0.5 µm or larger is necessary. An empirical linear fit indicates that the optical output power for a 3 µm device will be 1.4 ± 0.3 mW. The application requires the power to be stable with current, at the operating point, and a maximum slope efficiency of 0.4 W/A is specified. Figure 4.11 shows that an oxide aperture diameter of approximately 3 µm and lower would give a slope efficiency that is less than 0.4 W/A. Figure 4.15 indicates that a 3 µm oxide aperture device might have a current tuning coefficient of approximately 0.6 nm/mA, which is the specified target value. Smaller oxide aperture diameters give larger current tuning coefficients due to greater self-heating. Figure 4.16 shows that devices with circular oxide aperture diameters of 3.5 µm and less are able to output the minimum required optical power of 0.2 mW, with single mode performance that's greater than 30 dB, although the single-mode yield of 3.5 µm diameter devices is low. At the target optical output power of 0.5 mW, the SMSR of 3.5 µm oxide aperture diameter devices becomes less than 30 dB. 2.5 µm oxide aperture diameter devices still have the required SMSR, but are unable to output optical powers of 1 mW. Devices with elliptical oxide aperture dimensions of 1.5×3.7 µm also exhibit greater than 30 dB single-mode performance up to 0.5 mW. Figure 4.17 shows that none of the measured devices have a beam divergence, along both the major and minor axis, that's lower than the maximum allowed value of 25° at 0.2 mW. Due to the lasing of higher order transverse modes, the divergence angle typically increases at higher optical powers. Devices with a 3.5×27.5 µm oxide aperture dimension had a mean divergence angle of 24 ± 2° along the major axis. For circular oxide aperture devices, the mean divergence angle was 34.1 ± 2° for a 3.5 µm diameter. The specification did not specify a minimum OPSR, but polarisation

stability is required. Figure 4.20 shows that for circular oxide apertures, devices with an OPSR greater than 15 dB were measured. However, there is a large variation in the measured OPSR between different devices, so a low yield would be expected. Devices with oxide aperture dimensions of 1.5×3.7 µm appear to have a high OPSR of approximately 14 dB, with little variation between devices.

4.9 Conclusion

In this chapter, the optical output power, emission spectra and beam profile of oxide confined VCSELs designed for MACs were characterised and compared to the specification. The dimensions of elliptical and circular oxide aperture were systematically varied to identify an optimum oxide aperture for the given epitaxial structure, and determine possible alterations to the epitaxial structure to improve performance.

It was found that the vertical cavity resonance wavelength of the VCSEL epitaxial structure was shorter than intended by 4-6 nm, and did not align with the gain-peak at the intended operating temperature close to 70 °C. Therefore, the devices considered in this chapter were characterised at room temperature. For circular oxide apertures, characterisation of 2.5 µm and 3.5 µm oxide aperture diameter devices indicate that (with small changes to the epitaxial structure so that the cavity resonance wavelength meets the specification) 2.5 µm oxide aperture diameter devices meet most of the requirements. However, the mean divergence angles of $51.6 \pm 0.8°$ and $34.1 \pm 0.2°$, for 2.5 µm and 3.5 µm oxide aperture diameters, respectively, are larger than the maximum allowed value of 25°. The small oxide aperture dimensions, required for single-mode emission, produce optical modes with narrow beamwidths that lead to large divergence angles. Additionally, for the small oxide aperture diameters required for single-mode operation, there is a large blue shift in the fundamental mode wavelength. The MAC application requires VCSELs with an emission wavelength that matches the atomic transition wavelength exactly, so this blueshift must be compensated for in the epitaxial structure.

For a 2.5 µm oxide aperture diameter there was an approximately 4 nm blueshift. The internal temperature is also higher for small oxide aperture devices due to increased self-heating. Usually this increased self-heating is detrimental to device performance, as thermal rollover occurs at lower currents, limiting the maximum optical power. However, this also provides a way to lock the VCSEL emission wavelength to the atomic transition, as the wavelength can be varied by modulating the current. Here, the temperature increase was 13.3 °C/mA for a 2.5 µm oxide aperture, which corresponds to a current tuning coefficient of 0.8 nm/mA.

To manufacture oxide-confined VCSEL devices that fully meet the requirements of the MAC application, further changes to the epitaxial structure are required. One possibility is to move the position of the high Al concentration AlGaAs layer to reduce the overlap of the longitudinal mode profile. This would reduce the guiding so that single-mode operation is possible with larger apertures, and it may be possible to obtain a narrower divergence angle. The sensitivity of the mode wavelength to the aperture size will also be reduced, and could potentially lead to yield improvements. In [17], a 3.5 µm active diameter, inverted grating, VCSEL device had a FWHM divergence angle of 9.6°, which corresponds to a full-width $1/e^2$ divergence angle of 16.3°. This is narrower than the mean divergence angle of 34.1 ± 0.2°, for the 3.5 µm diameter oxide aperture VCSELs in this work, and it may be due to a weaker waveguiding by the oxide aperture. Alternatively, surface reliefs could be used to obtain single-mode operation with larger oxide aperture devices. In [17], a 5 µm active diameter VCSEL, with a 3 µm diameter surface relief, had a Gaussian-like far-field profile with a full-width $1/e^2$ beam divergence of 17.6°.

VCSELs for MACs are required to have a stable, linear polarisation. For circular oxide aperture devices, there was a large variation in the measured OPSR which would mean a low yield. While surface gratings have been used to reliably control the polarisation of the MAC VCSEL emission, with OPSRs of up to 21 dB reported [21], they require additional processing steps and electron-beam lithography due to the small feature size. Elliptical oxide apertures can introduce an anisotropy [24][25][26], to ensure devices have a stable, linear polarisation, without

additional processing steps. Here, 1.5×3.7 µm oxide aperture devices appeared to show an OPSR greater than 10 dB, with little variation. In [28], an OPSR greater than 15 dB was obtained with an approximately 2.5×2 µm rhomboidal oxide aperture. This suggests that with further optimisation, a higher OPSR could be obtained. However, for larger elliptical oxide apertures, it was found that the OPSR reduced, despite higher aspect ratios. This is likely due to the lasing of higher order modes, which suggests that elliptical oxide apertures can be effective for polarisation control only when the VCSEL emission is single mode.

Chapter 5

Characterisation of VCSEL material using Segmented Contact Technique

5.1 Introduction

In chapter 4, it was shown that for the small oxide aperture diameters required for single-mode emission, self-heating can cause the internal temperature of a vertical-cavity surface-emitting laser (VCSEL) device to increase significantly, which can affect the alignment of the cavity-resonance wavelength with the gain-peak wavelength. This alignment is important as it affects the threshold current of the device, and also determine whether polarisation switching occurs. Additionally, the use of surface reliefs and gratings, to improve the single-mode performance and polarisation stability, can also increase the optical losses, and alter the gain requirement of the VCSEL. An understanding of how the gain profile varies with temperature and current would help determine how the active layers could be altered to improve the VCSEL efficiency and yield, reducing the time and cost of optimisation.

However, compared to edge-emitters, optical gain measurements are not as straightforward on VCSEL material. External efficiency measurements of VCSEL devices [34][35][36] and

in-plane stripe lasers fabricated from VCSEL material [41] have been used to determine the gain at a particular wavelength. The in-plane Hakki-Paoli method has also been applied to VCSEL material to measure the gain profile, but only up to the threshold current density of the in-plane stripe [42].

In this chapter, an alternative in-plane gain measurement technique, known as the segmented contact stripe-length method [89][90], is applied on VCSEL material to measure the optical gain spectra. Using a simple technique, whereby the top mirror reflectivity is reduced by altering the phase shift at the cap layer, lasing in the vertical direction is suppressed, and the gain profile is characterised at current densities comparable to the threshold current density of an actual VCSEL device. The electrical and optical characteristics of VCSEL segmented contact devices are presented, and their impact on the gain measurement is discussed. The modal gain of the transverse electric (TE) polarised index-guided in-plane mode is measured and converted to a material gain by calculating its confinement factor. This is then related to the VCSEL device performance.

5.2 Sample

Segmented contact stripes, which are described in section 3.2.4, were fabricated from two separate VCSEL epitaxial structures. Except for differences in the growth method and cap thickness, the epitaxial structure was nominally identical. One sample was grown by molecular beam epitaxy (MBE) and had a 124 nm cap layer, whilst the other sample was grown by metal organic vapour-phase epitaxy (MOVPE) and had a 62 nm cap layer. Both structures were grown on a GaAs substrate and had a 1-λ thick cavity, which contained three 6 nm $In_{0.06}Ga_{0.94}As$ quantum wells (QW) with a graded AlGaAs separate confinement heterostrure (SCH). The cavity was sandwiched between an upper p-doped and lower n-doped $Al_{0.12}Ga_{0.88}As/Al_{0.9}Ga_{0.1}As$ distributed Bragg reflectors (DBR) with graded interfaces. The substrate, cap, and DBR layers were doped with C and Si for the acceptor and donor, respectively.

5.3 I-V Characteristics

Figure 5.1a shows the raw I-V curves of segmented contact sections. Sections that weren't electrically pumped were grounded. Below the turn-on voltage of approximately 1.4 V, the current increases linearly with voltage indicating the presence of a resistive leakage path in parallel. The resistance of the leakage path (which is related to the inter-contact resistance) is measured to be 13.7 Ω, 15.3 Ω, and 8.4 Ω for section 1 and 2 (S1S2), section 1 (S1), and section 2 (S2) respectively. Due to current spreading in the highly doped DBR layers, the 8 µm gap between each section is not large enough to electrically isolate each section. The leakage resistance is close to half that of S1 and S1S2. In the case of S2, there were two leakage paths due to adjacent sections that were grounded, whereas for S1 and S1S2 there were only one leakage path.

Figure 5.1b shows the compensated current density – voltage curves of the segmented sections, where the leakage current was subtracted and the injection current converted to a current density using the contact area and a multiplicative current spreading factor(see section 5.4). S1 and S1S2 have similar curves, so for a given voltage the current density should be the same.

However, S2 has a voltage offset of $+0.08 \pm 0.01$ V compared to S1 and S1S2. Given that S1 and S1S2 have similar curves, this may be due to S2 having two adjacent sections that are grounded which can reduce the current density at the ends of the stripe.

5.4 Lateral Current Spreading

The current density of the pumped region below the contacts is reduced by lateral current spreading in the highly doped mirror layers. Therefore, a lateral current spreading factor of 0.73 ± 0.02 was applied to the current density determined, by dividing the injection current by the contact area. Figure 5.2a shows the vertical spontaneous emission profile of S1S2,

(a)

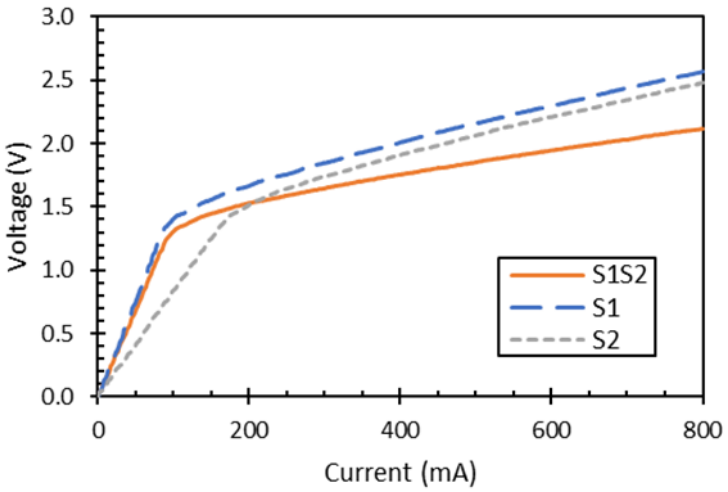

(b)

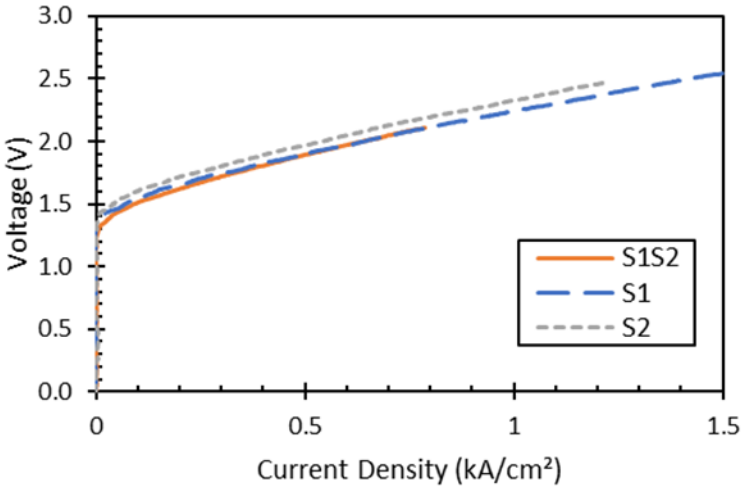

Figure 5.1: (a) The raw current-voltage curve, and (b) the compensated current density-voltage curve when section 1 and 2 (solid orange), section 1 (long dashed blue), and section 2 (short dashed grey) are electrically pumped.

(a)

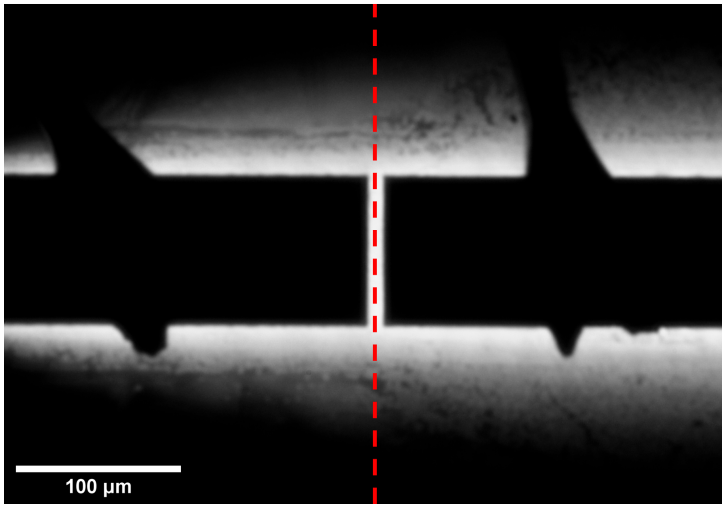

(b)

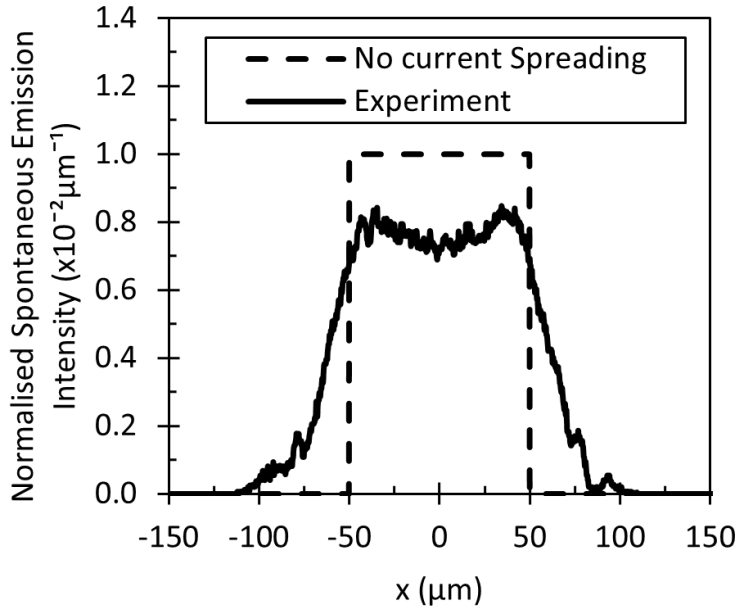

Figure 5.2: (a) Vertical emission from the top surface of segmented contact devices pumped at 0.29 kA/cm^2, imaged with a 4× microscope objective. (b) normalised measured intensity profile (solid black) of the vertical spontaneous emission from the gap between S1S2 (indicated by the red dashed line in a) and the normalised current density profile defined by the metal contacts assuming no lateral current spreading is present. Figure from [93].

imaged using a 4x microscope objective lens. The impact of lateral current spreading was estimated from figure 5.2b, which shows a line profile of the vertical spontaneous emission profile from the gap between S1S2. It was assumed the intensity is linearly proportional to the current density, so that figure 5.2b gives the lateral current density profile. When compared to a profile that assumes no lateral current spreading is present, the current density in a 20μm wide central portion is lower by 27 %.

5.5 Simulation of In-Plane Modes of a VCSEL Structure

The TE-polarised in-plane modes were calculated using a transfer matrix method, outlined in [43]. Refractive index values from [99], [100], [101], and [102] were used. Due to a lack of temperature dependent refractive index data for InGaAs, room temperature values were used for InGaAs at all temperatures. Additionally, refractive index values above the bandgap energy were not available, so the refractive index value at the bandgap energy was used instead. To simplify the calculation of the in-plane modes, only real refractive index values were used, so that the propagation constant to be determined would be a real value.

5.5.1 Index-guided In-Plane Modes

Figure 5.3a shows the squared magnitude of the transverse electric field profile of the fundamental TE-polarised mode, and the corresponding refractive index profile, at 30 °C at 886.5 nm (886.5 nm is the cavity resonance wavelength at 30 °C determined from figure 5.12). Only a single index-guided TE-polarised mode was found over the wavelength and temperature range of interest. This suggests that when the segmented contact technique is applied to this structure, the results won't be complicated by the collection of amplified spontaneous emission (ASE) coupled into several different modes with different modal gains. However, it's possible radiative modes with a complex propagation constant may also be present within the structure. It is expected that these modes will have a low overlap with the QW layers and a high overlap with the highly doped DBR layers, and so will have a net modal gain of below

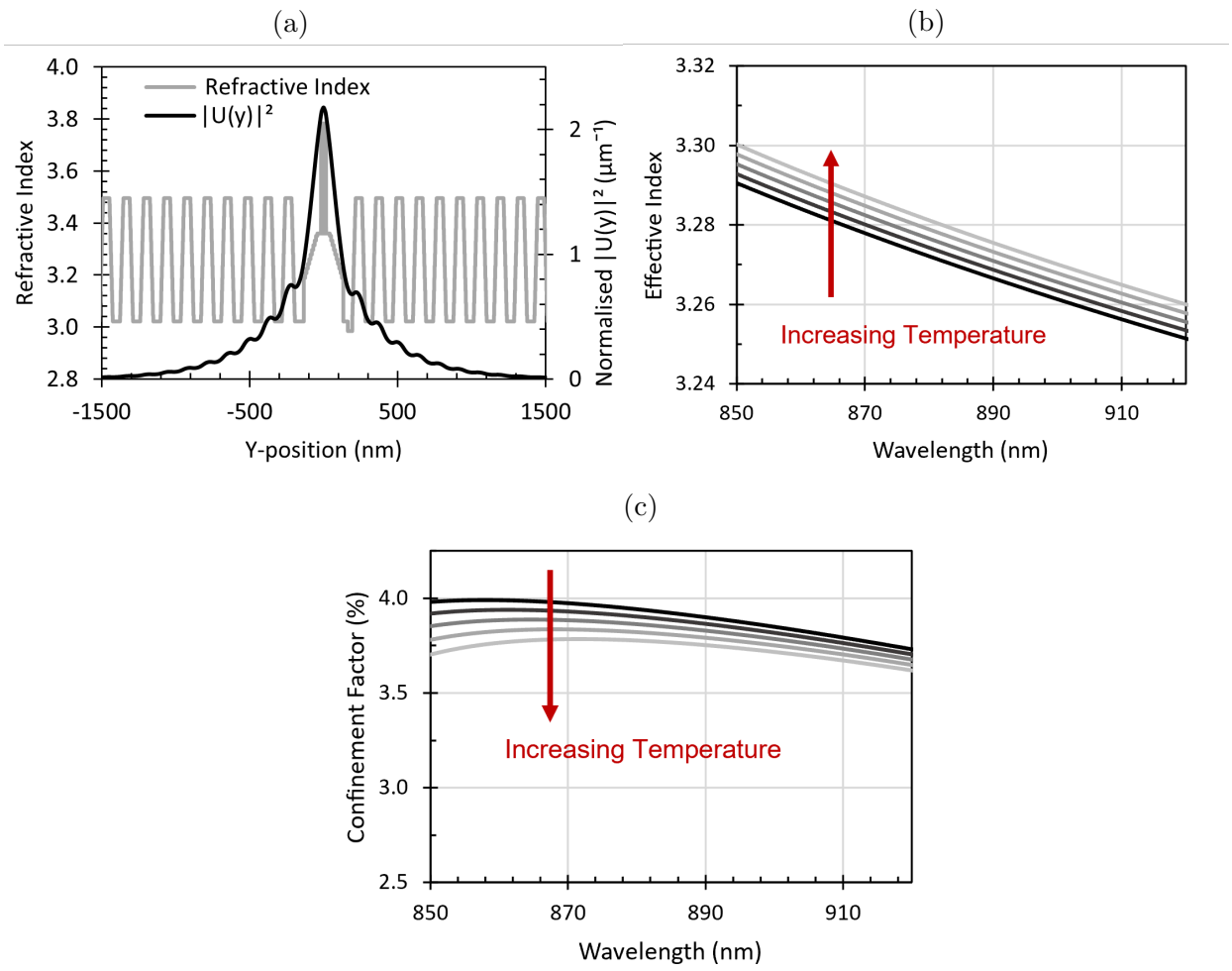

Figure 5.3: (a) Refractive index profile of a section of the VCSEL cavity (solid grey) and the calculated mode profile $|U(y)|^2$ (solid black) of the in-plane index-guided TE mode at the measured cavity resonance wavelength of 886.5 nm at 30 °C. (b) and (c) shows the calculated effective index and confinement factor respectively, over a wavelength range of 850-920 nm, for temperatures of 30-70 °C, varied in 10 °C steps.

zero. As such, at wavelengths close to the gain-peak where the index guided mode will have a positive net-modal gain, their contribution to the ASE spectra will be negligible. On the other hand, at the long and short wavelength tails, the collected ASE will be from regions originating close to the facets and may produce an offset which affects the measured gain.

From figure 5.3c, the confinement factor at 30 °C has a maximum value of 3.99% at 858 nm. Over the wavelength region of interest, the confinement factor does not appear to vary significantly with wavelength and temperature. At a wavelength of 886.5 nm, assuming a 1 % deviation in the InGaAs refractive index value, the confinement factor of the in-plane mode changes by approximately 10 %. This would correspond to a comparatively large error of 10 %, for the material gain values that are converted from the measured in-plane modal gain values using equation 2.21.

Figure 5.3b shows that the effective index of the TE mode decreases with wavelength. At 30 °C, the effective index is 3.290 at 850 nm and decreases to 3.251 at 920 nm. The effective index increases slightly with temperature and is 3.300 at 70 °C at 850 nm.

5.5.2 Slow light VCSEL Cavity In-Plane Modes

The VCSEL slow light [53][54] modes (see section 2.7.2) were calculated for a structure with a 124 nm thick cap in air so that the mirror reflectivity was high. A high mirror reflectivity means radiation losses are low, so that a real propagation constant could be used to find the mode. When the cap thickness is aligned to the anti-phase thickness, this reduces the reflectivity and increases the radiation loss of the slow light modes. It is assumed that this introduces an imaginary part to the propagation constant, while the real part of the propagation constant remains approximately the same (as the resonance wavelength is not significantly affected by the changing cap thickness and addition of metal layers). It is also assumed that the confinement factor is reduced, so that the confinement factor values given in figure 5.4c provide an upper limit to the confinement factor values in the anti-phase structure.

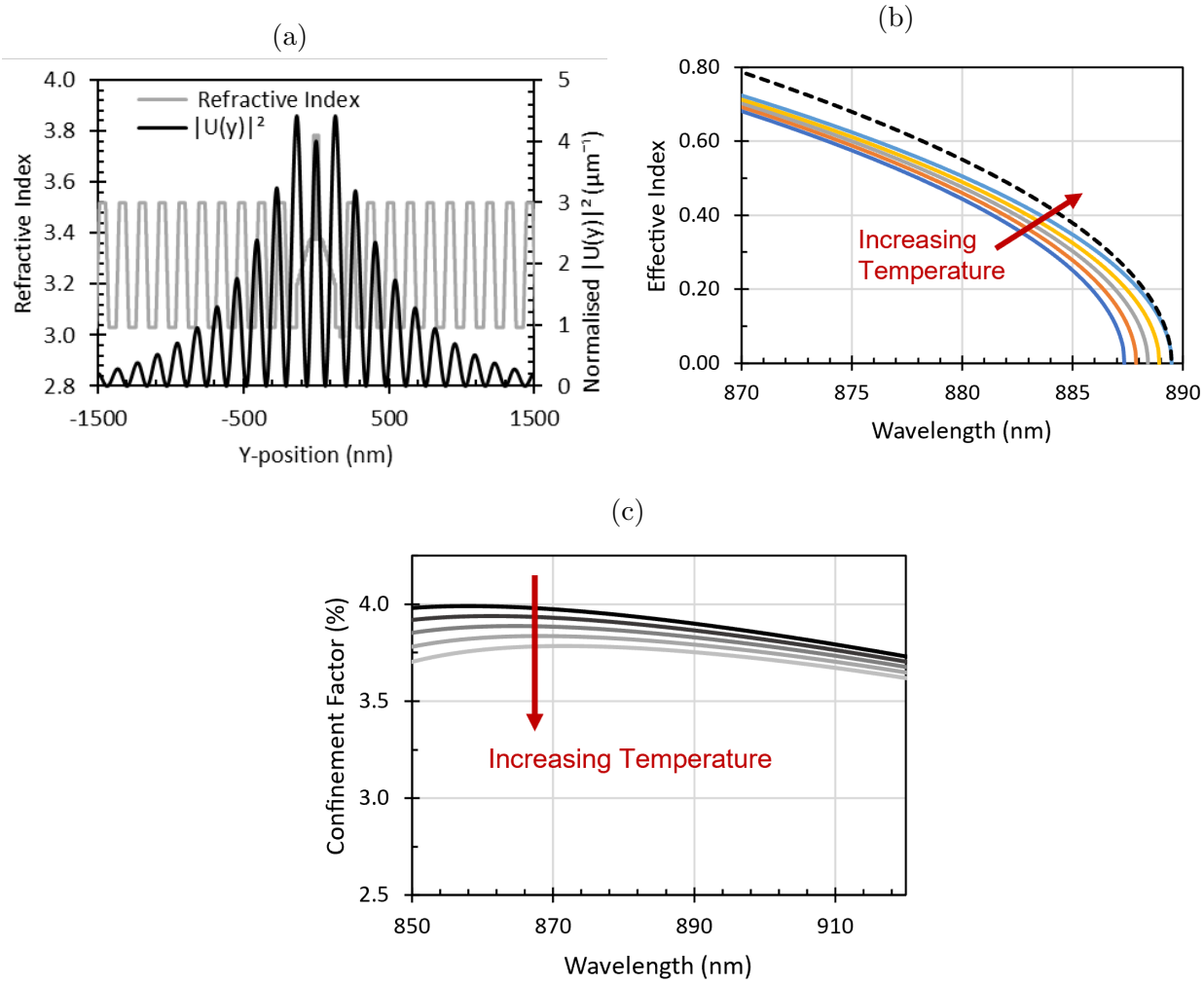

Figure 5.4: (a) shows the section of the refractive index profile (solid grey) and the calculated mode profile $|U(y)|^2$ (solid black) of the in-plane slow light TE mode at 860 nm at 30 °C. (b) and (c) shows the calculated effective index and confinement factor respectively, for temperatures of 30-70 °C in 10 °C steps.

Figure 5.4 shows the squared magnitude of the transverse electric field profile of the slow light mode, and the corresponding refractive index profile, at 860 nm at 30 °C. Compared to the index-guided mode, the mode extends further into the DBR layers, which suggests that internal optical losses due to free carrier absorption will be higher. Figure 5.4 shows that the effective index decreases with increasing wavelength, until it reaches the 1D vertical cavity resonance wavelength where $Re(n_{\text{eff}})$ goes to 0. For wavelengths longer than the vertical cavity resonance wavelength, the in-plane k-vector components of the slow light mode will be imaginary and won't propagate along the plane of the structure. With increasing temperature, the vertical cavity resonance wavelength redshifts, and slow light modes are present in the structure at longer wavelengths. The dashed line shows the effective index-wavelength dispersion curve at 70 °C, calculated using equation 2.17, so that the vertical component of the k-vector is constant (and corresponds to a vertical cavity resonance wavelength of 889.48 nm). At shorter wavelengths, this curve deviates from the simulated curve which includes material dispersion. When material dispersion is considered, the effective index at 870 nm is 0.787, which corresponds to a vertical cavity resonance wavelength of 886.38 nm.

As n_{eff} becomes small, there will be a strong enhancement to the per unit length modal gain. However, there will also be an enhancement to the optical loss. As will be discussed in section 5.7.1, the radiation loss can be increased by altering the thickness of the cap. Neglecting dispersion, the magnitude of the k-vector component along the vertical direction will be the same for all wavelengths. If the lasing of the vertical mode can be suppressed by increasing the mirror loss, this means that radiation losses of the slow light modes at other wavelengths will also be high, so that the net modal gain will be below zero. As mentioned above, when material dispersion is present, the vertical component of the k-vector will change, so that the mirror losses may not be as high. Additionally, the emission angle of the in-plane slow light modes at shorter wavelengths will be closer to the normal, and the angle may overlap with the index guided mode, affecting the measured ASE.

Figure 5.4 shows the calculated confinement factor. The confinement factor is 2.66 % at 850 nm

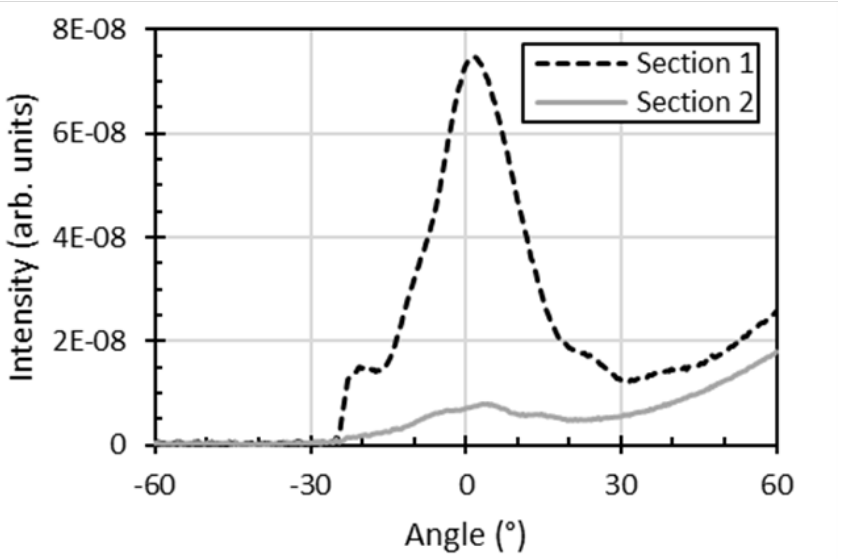

Figure 5.5: Far-field profile for the in-plane emission when section 1 (dashed black) and section 2 (solid grey) are pumped at a current density of 0.438 kA/cm^2 for the 124 nm cap device. Emission at 0° corresponds to light along the normal to the facet.

and decreases to 2.43 % at 887.3 nm. The confinement factor increases slightly with temperature, and at 70 °C, the value at 850 nm is 2.70 %. The confinement factor of the slow light mode is similar to that of the index guided mode, and a similar proportion of the spontaneous emission might be expected to be coupled into the modes. At wavelengths where the net-modal gain of the index-guided mode is negative, depending on the collection geometry, the measured ASE of the index-guided and slow light mode may be similar, and may cause an offset in the measured gain spectra.

5.6 Farfield

Figure 5.5 shows the in-plane farfield profile. The setup was aligned so that 0° corresponds to an angle close to the facet normal. The far-field profile for S1 shows a peak in the intensity close to 0° and is most likely that of the index guided mode. The FWHM width of the peak is 20.3 ± 0.3°. There appears to be ripples in the profile, which might be expected as ripples can be seen in the simulated mode profile (shown in figure 5.3), as the index-guided mode partially extends into the DBR layers with alternating high and low refractive indices. Initially,

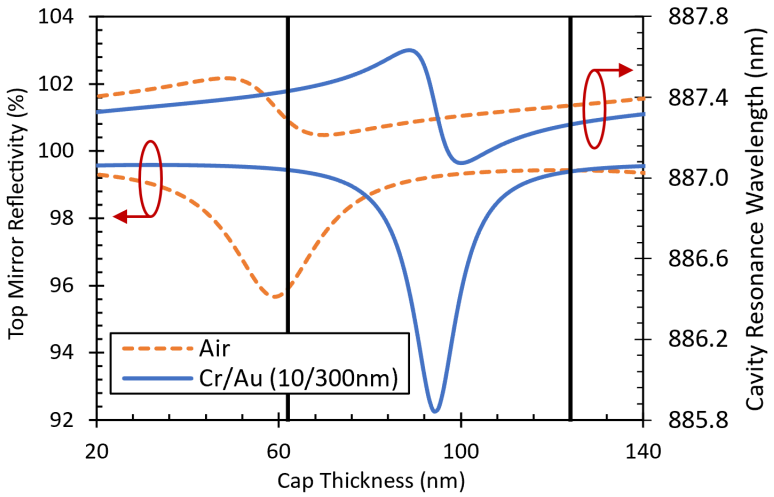

Figure 5.6: Simulated top mirror reflectivity (left axis) and the respective cavity resonance wavelength (right axis) as a function of cap thickness, when air is above the cap and when Cr/Au layers are deposited on top of the cap. The nominal cap thicknesses of the two structures are denoted by the vertical black lines. Figure from [93].

the intensity decreases at angles further away from the normal. However, beyond 30°, a continuous increase in the intensity can be observed. This is likely to be from light coupled into the slow light mode. Below -25°, the intensity approximately goes to zero as the emission is blocked by the copper mount and the TO-Header below the device. The same is observed for S2.

For S2, the intensity at 0° is approximately 10 times lower due to absorption by S1 which has been grounded. The high angle emission doesn't appear to change significantly compared to when S1 was pumped, which suggests that a significant proportion of the light originates from the top surface, as simulations indicate these modes will be lossy. By limiting the collection angle, and imaging the facet onto the spectrometer slits, it is possible to ensure only the ASE of the index guided mode is measured.

5.7 Suppression of Vertical Lasing

5.7.1 Effect of Cap on Mirror Losses

The dependence of the top mirror reflectivity on the cap thickness, due to changes in the phase of the reflected light, is shown in figure 5.6. The reflectivity was calculated using the transfer matrix method outlined in section 2.8.1. In air, a 124 nm thick cap is at an in-phase reflectivity maximum, while a 62 nm thick cap is aligned to an anti-phase reflectivity minimum. However, unlike a standard VCSEL structure, the segmented contact structures require a metal contact that covers the top cap. With the addition of Cr/Au layers on top of the cap, the reflectivity minimum shifts due to the complex refractive index of the metal [103]. Neither the 62 nm or 124 nm cap thickness is aligned to the anti-phase reflectivity minimum, which occurs at a cap thickness of approximately 93 nm instead.

Compared to the GaAs/Air interface, the addition of the Cr/Au layers enhances the in-phase and anti-phase reflectivity. When the reflection is in-phase, a reduced threshold gain would be expected. On the other hand, anti-phase reflections are expected to significantly increase the threshold gain required to lase in the vertical direction.

5.7.2 P-I Characteristics

Figure 5.7 shows the in-plane and vertical emission Power-current curves for both the 62 nm cap and 124 nm cap segmented-contact devices. To eliminate self-heating, the sections were pumped with an in-house pulsed current source, with a 1 µs pulse width and a 1 kHz repetition frequency. The same pulse settings were used for the gain measurements. For the vertical emission, figure 5.2a shows that some of the light emitted from regions below the contacts could be seen at the edge of the contacts, which was then measured with an integrating sphere.

In segmented contact devices fabricated from the sample with the 62 nm thick cap layer, the vertical emission P-I characteristics indicate vertical amplification and possibly lasing,

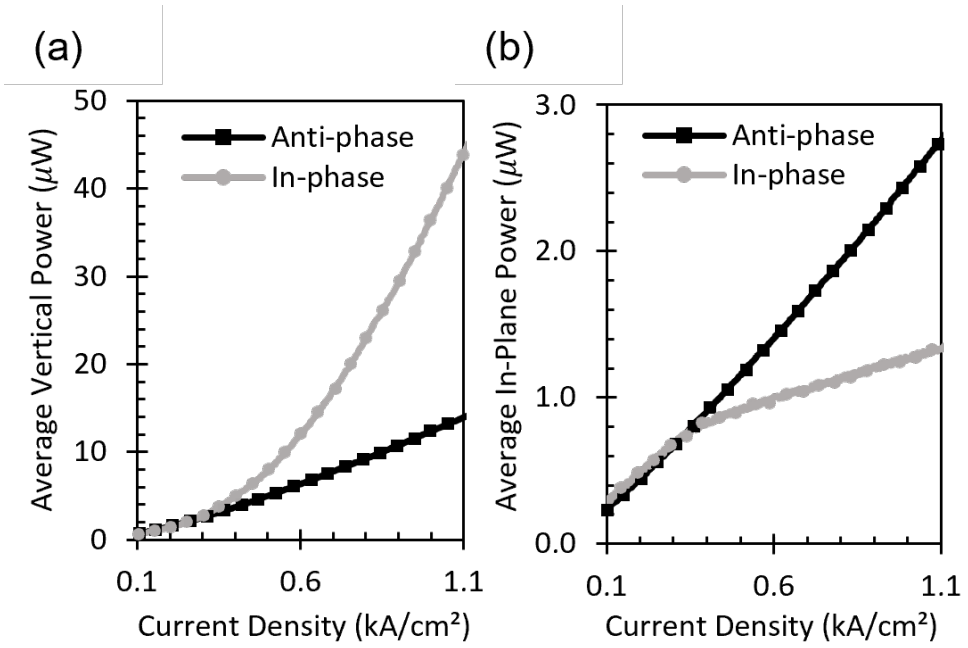

Figure 5.7: P-I curves of light emitted from section 2 in the (a) vertical and (b) in-plane direction for in-phase 62 nm (grey circle) and anti-phase 124 nm (black square) cap thicknesses. Figure from [93].

occurring above a current density of 0.4 kA/cm^2. The corresponding in-plane P-I curve, of the in-plane emission, shows that the slope of the curve reduces above a current density of 0.4 kA/cm^2, suggesting that the carrier density is clamping in certain areas of the active region, again indicative of amplification and possibly lasing in the vertical direction. However, this is not observed in the device with 124 nm thick cap layer. There is no apparent threshold in the vertical emission, nor clamping of the in-plane emission. Therefore, gain measurements are performed on the 124 nm thick cap device, as the gain vs current density relation will not be complicated by carrier pinning effects.

Previous work [104][105][106] has indicated that upon deposition, Cr diffuses into GaAs, and after annealing, Ga and As are expelled from the inter-mixed Cr-GaAs interface. This effectively reduces the optical thickness of the p-GaAs cap, and changes the in-phase and anti-phase condition. While this effect is unlikely to align the effective cap thickness, of the initially 124 nm thick cap, to the anti-phase cap thickness, a sufficient increase in the top mirror loss will still allow the optical gain to be characterised, at current densities close to

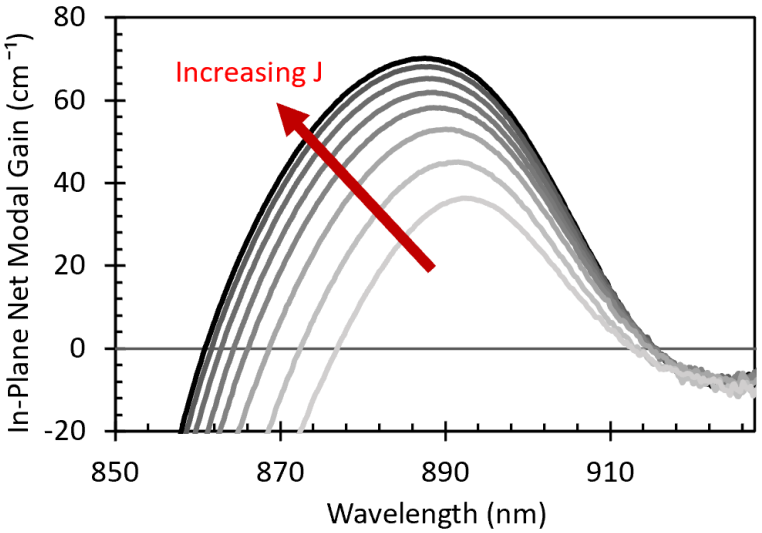

Figure 5.8: In-plane modal gain curves of the anti-phase device for a current density, J, range of 0.417-1.147 kA/cm^2 in 0.104 kA/cm^2 steps at a temperature of 30 °C. Figure from [93].

the threshold current density. As a result, samples with a 62 nm cap thickness are labelled as in-phase, and samples with a 124 nm cap thickness are labelled as anti-phase.

5.8 In-plane Gain Measurement on VCSEL Structure

5.8.1 124 nm Thick Cap Anti-Phase Device

Figure 5.8 shows the TE polarised in-plane modal gain at 30 °C, measured on the material with a 124 nm thick anti-phase cap, for injected current densities ranging from 0.417-1.147 kA/cm^2. At a current density of 0.417 kA/cm^2, the peak net-modal-gain is measured to be 36 ± 2 cm^{-1} at a wavelength of 892.6 ± 0.4 nm. At 1.147 kA/cm^2, the peak net-modal-gain increases to 70 ± 1 cm^{-1} and blueshifts to 887.4 ± 0.1 nm. The measured internal optical mode loss of 8.1 ± 0.7 cm^{-1} is determined by taking the mean value of the plateau region, over the wavelength range of 922.5-927.5 nm. The in-plane internal optical loss may be different to that experienced in the vertical direction, as the overlap of the mode with absorbing regions and scattering losses due to interface fluctuations will be different. However, it is important here as, before calculating the material and VCSEL modal gain, it must be used to correct

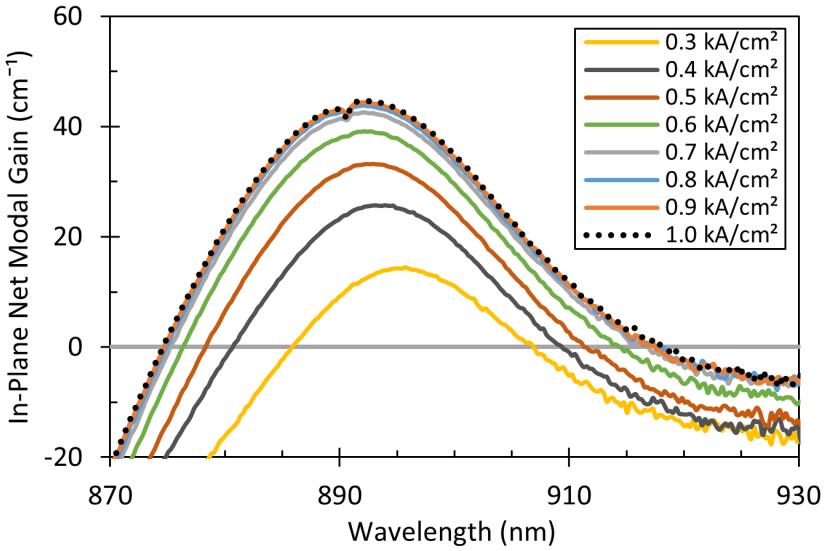

Figure 5.9: In-plane modal gain curves of the in-phase device at a temperature of 23 °C, for a current density range of 0.3-0.9 kA/cm^2 (solid lines) in 0.1 kA/cm^2 steps, and at a current density of 1.0 kA/cm^2 (black dashed line).

the net-modal-gain data to modal-gain.

5.8.2 62 nm Thick Cap In-Phase Device

Figure 5.9 shows the TE polarised in-plane modal gain at 20 °C, measured on the material with a 62 nm thick cap, for injected current densities ranging from 0.3-1.0 kA/cm^2. The gain increases with increasing current density, until it reaches a current density of 0.8 kA/cm^2. Apart from a small dip at 890.6 nm, which increases in size with increasing current density, the gain curve at a current density of 0.8 kA/cm^2 is identical to that at 1.0 kA/cm^2. The position of the dip corresponds to the resonance wavelength of the vertical cavity, and is due to scattered laser light being detected by the camera and causing an offset in the measured ASE. As shown in figure 5.10, for both S1 and S1S2, the measured ASE spectrum at 1.5 KA/cm^2 show a small peak at 890.6 nm. The amount of scattered light increases with current density, increasing the offset, and thus the dip gets larger. If the gain was actually reduced, a corresponding dip in the ASE spectrum would be expected.

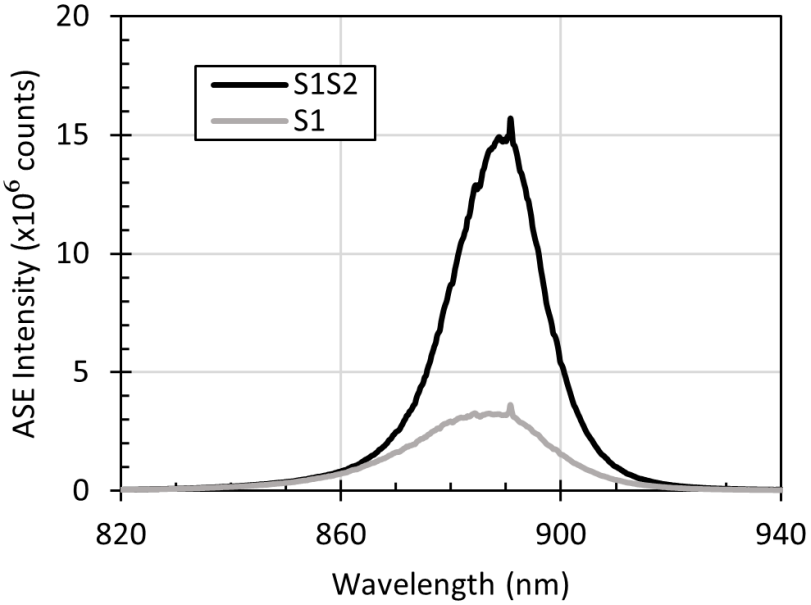

Figure 5.10: In-plane ASE spectrum from S1 (solid grey) and S1S2 (solid black), for the in-phase device at a temperature of 23 °C, and a current density of 1.5 kA/cm^2.

5.9 Impact on Device Performance

5.9.1 Device Operating Point

VCSEL devices were fabricated from the same wafer using a quick fabrication process [107], and the substrate was lapped to reduce self-heating. A large oxide aperture diameter of 13 ± 0.5 µm was utilised to reduce scattering losses by the oxide aperture. Figure 5.11 shows the mean threshold current density of fabricated VCSEL devices at different temperatures under pulsed operation, which indicates the threshold current density minima occurs below 30 °C. This is consistent with the optical gain and cavity resonance measurements shown in figures 5.8 and 5.12, which shows the gain peak wavelength at a longer wavelength than the cavity resonance wavelength, even for a current density of 1.147 kA/cm^2 which is above the measured threshold current density. Due to the higher thermal redshift of the gain-peak wavelength, this would indicate alignment of the gain-peak with the cavity resonance occurring at temperatures below 30 °C. This is discussed further in section 5.9.3

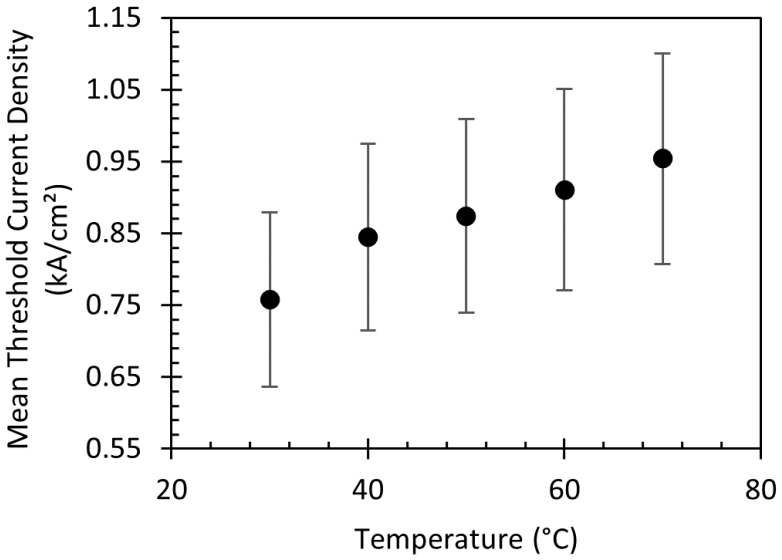

Figure 5.11: Mean threshold current density of VCSEL devices, with a nominal oxide aperture diameter of 13 µm, at different substrate temperatures under pulsed operation with a 10 µs pulse width and 1 kHz repetition frequency. Figure from [93].

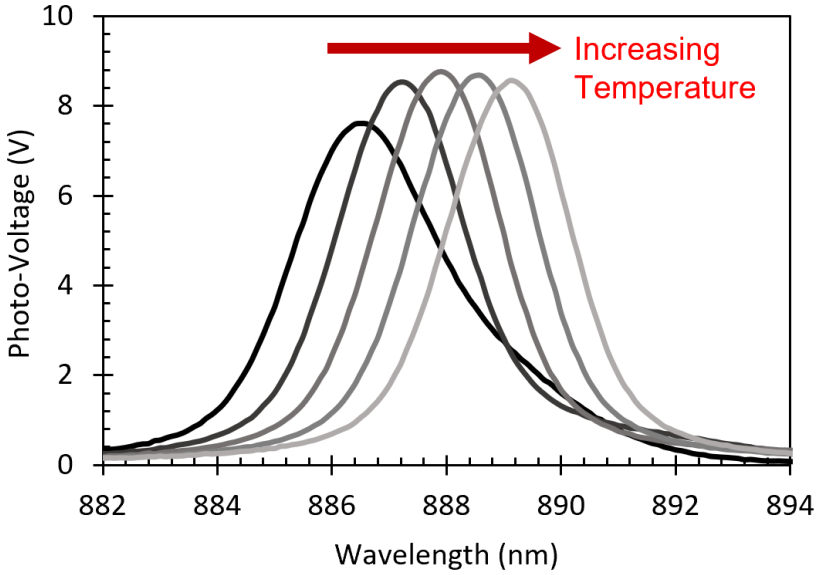

Figure 5.12: Photo-voltage spectra at temperatures of 30-70 °C in 10 °C steps. The cavity resonance wavelength was determined from the peak position. Data taken by Josie Travers-Nabialek. Figure from [93].

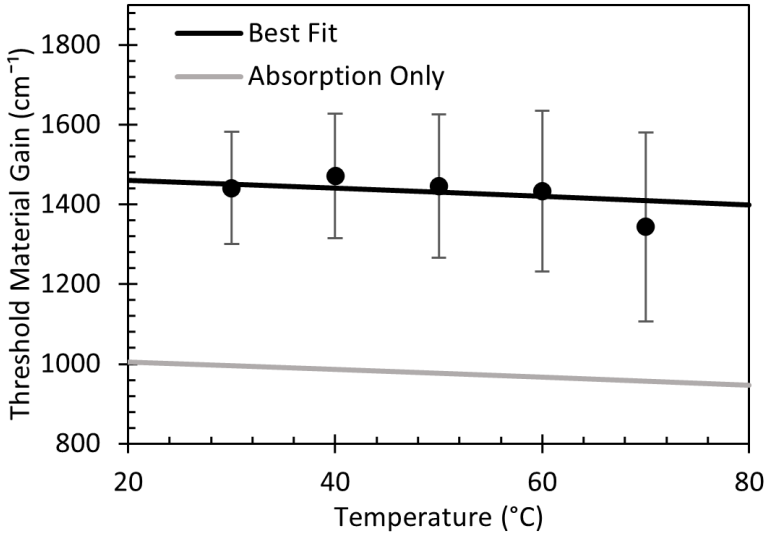

Figure 5.13: The lasing threshold gain calculated using equation 2.37. (solid lines) for the in-phase VCSEL device, and the experimentally obtained material gain at the lasing wavelength and threshold current density (black circles). Figure from [93].

Figure 5.12 shows the surface photo-voltage spectroscopy (SPVS) spectra obtained by Josie Travers-Nabialek, where the photo-voltage induced by light incident on the surface of the wafer is measured [108][109][110]. At the cavity resonance wavelength, there is a sharp peak in the photo-voltage due to a higher photon density within the vertical cavity increasing the number of electron-hole pairs generated in the active layers. The cavity resonance wavelength is measured to be 886.5 ± 0.1 nm at 30 °C and redshifts to 889.1 ± 0.1 nm at 70 °C. This gives a thermal tuning coefficient of 0.066 nm/K for the cavity resonance wavelength. There is an additional uncertainty due to the difference in location on the wafer from where the segmented contact and SPVS samples were taken and variations of approximately ±2 nm in the cavity resonance wavelength across the 4" wafer.

5.9.2 Threshold Material Gain

Figure 5.13 compares the lasing threshold material gain calculated from the experimentally obtained in-plane modal gain (evaluated at the cavity resonance wavelength at the relevant temperature and at the current densities corresponding to threshold in the VCSEL) with the lasing threshold material gain determined using equation 2.37. To convert the modal gain

into a material gain, the mode properties from figure 5.3 were used. For example, at 30 °C values of $n_{\text{eff}} = 3.268$ and $\Gamma = 0.0387$, evaluated at 886.5 nm, were used to convert the gain measured at 30 °C. The combined effect of these values on the converted material gain varied by 5 % over the temperature range of interest.

To determine the lasing threshold material gain for the vertical cavity resonance mode, values of $\Gamma_{\text{enh}} = 1.85$, $R_{\text{top}} = 99.42$ % , and $R_{\text{bot}} = 99.88$ % were used at 30 °C. Internal optical losses in the doped AlGaAs DBR layers (with C and Si as the acceptor and donor, respectively) were included using equation 2.25, by adding an imaginary term to the refractive index values according to the doping concentration. Absorption values for doped GaAs from [36] and [50] were used, due to a lack of doping-induced absorption data for AlGaAs. In n-GaAs, the doping-induced absorption shows a weak wavelength dependence, and values at 1000 nm were used [36]. On the other hand, the absorption in p-GaAs (doped with Zn) is shown to have a λ^3 dependence [36], and the absorption values were extrapolated to 890 nm. The structures given within this thesis used C as the acceptor. Measurements from [50] indicate that when a C acceptor is used, the p-GaAs absorption values are double those of when a Zn acceptor is used.

At 30 °C, the threshold gain value was measured to be 1440 ± 140 cm^{-1}. The uncertainty in the threshold gain values were dominated by the uncertainty in the threshold current density due to the oxide aperture diameter. When internal optical losses due to doping-induced absorption only are considered, the required threshold gain is calculated to be 1010 cm^{-1} at 30 °C, underestimating the threshold material gain by around 450 cm^{-1}. One possibility is that additional scattering losses are present in the n-DBR layers due to interface roughening, as reported in [111]. A best fit is obtained when the optical loss in the n-DBR layers is increased from 7 cm^{-1} to 40 cm^{-1}. This is of the same order as the estimate of the optical loss of 80 ± 20 cm^{-1} obtained by linear interpolation of the values in [111], for a MOCVD grown n-DBR with the same nominal doping concentration of 2×10^{18} cm^{-3}. However, due to differences in the operating wavelength, material composition, and growth method, a direct comparison is

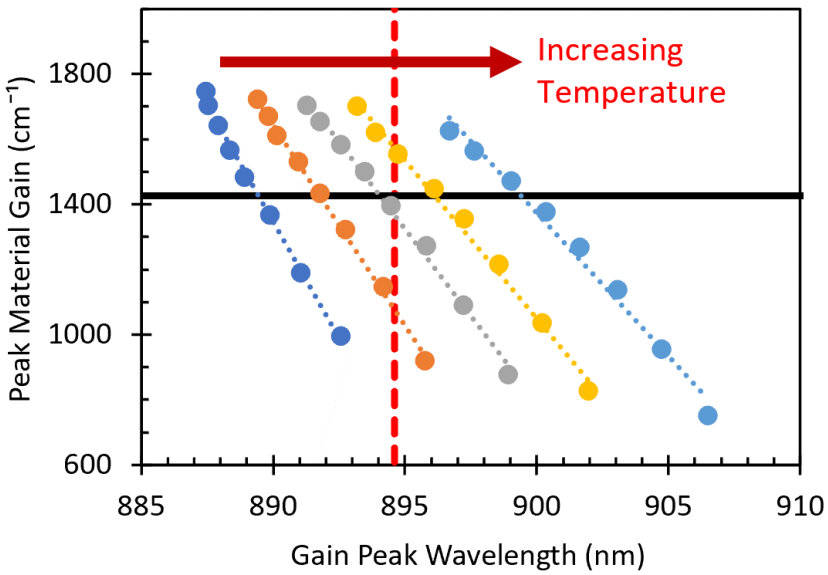

Figure 5.14: Experimentally obtained peak material gain values and the corresponding wavelength, with linear fits, at temperatures ranging from 30-70 °C in 10 °C steps. The horizontal solid dark line indicates the experimentally obtained threshold material gain value at 30 °C. The vertical dashed red line shows the target operating wavelength of 894.6 nm. Figure from [93].

difficult. Scattering losses may be present in the p-DBR, and there may be other loss mechanisms, such as increased absorption in the SCH at high current injection [36].

5.9.3 Gain Peak Optimisation

Figure 5.14 shows the measured peak material gain and wavelength. The dotted lines show linear fits to the data, applied for each temperature. The vertical dashed red line shows the target lasing wavelength of 894.6 nm, and the horizontal solid black line shows the mean measured threshold material gain of 1430 ± 20 cm^{-1}. Where the (vertical dashed red and horizontal solid black) lines cross correspond to the operating point of the intended VCSEL structure. The figure can be used to determine changes to the the active layer that would optimise it for a particular operating condition. For example, consider a 7 µm oxide aperture diameter VCSEL operating CW at a current of 2 mA and a heat-sink temperature of 60 °C. Figure 4.8 indicates that a 7 µm diameter oxide aperture VCSEL will have an optical loss similar to what is shown by the horizontal black line. If it is operating at a current of 2 mA,

figure 4.15 suggests that an internal temperature increase of 10 °C might be expected, so that the temperature of the active layers would be 70 °C. The gain peak aligns with the targeted emission wavelength of 894.6 nm at a temperature of approximately 55 °C, indicating that for the current active region, the ideal CW heat-sink temperature is 45 °C. However, for uncooled packaging, the VCSEL will likely operate at a higher temperature of 60 °C. To satisfy the requirement, the 70 °C material gain peak value-wavelength line would need to be translated by approximately 5 nm to ensure it crosses the operating point. Such a relatively simple change could be implemented in subsequent growths by calibrating to a 5 nm blueshift in the room temperature active region photoluminescence (PL) peak.

5.10 Conclusion

In this chapter, the optical gain was characterised on VCSEL material using the segmented contact method, at current densities comparable to the threshold current density of an actual VCSEL device. This information can then be used to inform changes to the active layers to improve the efficiency and yield of VCSELs, reducing the time and cost of the optimisation process.

Reflections from the cap layer - metal contact interface, which destructively interfered with the DBR reflections, were utilised to suppress lasing in the vertical direction. This was to ensure carrier pinning did not alter the gain-current relationship, so that the optical gain could be characterised at the threshold current density of an actual VCSEL device. It was found that after deposition of Cr/Au contacts on a p-GaAS cap, vertical lasing was observed with an initially anti-phase 62 nm thick cap, while lasing was suppressed with an initially in-phase 124 nm thick cap. Simulations of the top mirror reflectivity using literature values indicated that, assuming nominal thicknesses, both samples would have similar threshold gain values. This suggests the effective cap thickness was modified by the process steps, and must be taken into account when applying this technique to other VCSEL epitaxial materials.

The TE-polarised in-plane modal gain was measured on VCSEL epitaxial material, for two different samples; one sample where lasing in the vertical direction was present, and another sample where lasing in the vertical direction was suppressed using the aforementioned method. On the lasing sample, the gain spectrum did not change above a current density of 0.8 kA/cm^2 due to carrier pinning.

For the non-lasing sample, the measured modal gain was converted to a material gain, by calculating the confinement factor and effective index of the TE-polarised index guided mode. The material gain was evaluated at the cavity resonance wavelength and the threshold current density of 13 µm oxide aperture diameter VCSEL devices. This gave a threshold material gain of 1440 ± 140 cm^{-1} for this structure at 30 °C. Using the transfer matrix method, with doping induced absorption values from the literature, a threshold gain of 1010 cm^{-1} was determined from the lasing condition. This suggests the presence of a loss mechanism in addition to the doping induced absorption. Agreement was found by increasing the optical loss in the n-DBR layers from 7 cm^{-1} to 40 cm^{-1}, which is consistent with previous work with additional scattering losses due to interface roughening in the n-DBR layers [111]. However, this is not conclusive, and there may be additional scattering losses present in the p-DBR or other loss mechanisms, such as increased absorption in the SCH at high current injection [36].

Alterations that would optimise the active layers, for a reduced threshold current, were determined by plotting the experimentally obtained peak material gain as a function of the gain-peak wavelength, and comparing with the measured threshold material gain of the VCSEL epitaxial material and intended emission wavelength of 894.6 nm. Taking into account the internal temperature increase due to self-heating, it was shown that for a 7 µm oxide aperture diameter VCSEL device, a 5 nm blueshift in the active region PL peak would optimize the active layers for CW operation at 2 mA with a heat-sink temperature of 60 °C. This has the potential to allow more rapid optimization of the active region in VCSEL wafers, reducing the development time and cost required to manufacture VCSEL devices with low threshold current and high yields.

Chapter 6

Conclusion

6.1 Summary

In this work, the impact of the oxide aperture dimension on the performance of oxide-confined vertical-cavity surface-emitting laser (VCSEL) devices was investigated. The key aims were to determine an optimum oxide aperture dimension, for the given VCSEL epitaxial material which had been designed for use in miniaturised atomic clocks (MAC); and identify possible alterations to the epitaxial structure to improve performance. Additionally, to assist with the optimisation process, an in-plane gain measurement technique, known as the segmented contact method, was utilised. By applying this technique directly on VCSEL material, and carefully considering the reflections at the cap layer to suppress lasing in the vertical direction, the gain profile was measured at current densities comparable to the threshold current density of an actual VCSEL device.

The MAC application places strict requirements on the VCSEL characteristics - which are strongly affected by the dimensions of the oxide aperture. To determine an optimum oxide aperture diameter, circular oxide aperture VCSELs with a range of diameters were characterised. It was found that for the epitaxial structure considered in this thesis, 2.5 µm oxide aperture

diameter VCSELs were able to meet most of the specification. Devices with this oxide aperture diameter had a mean slope efficiency of 0.34 ± 0.7 W/A, which is slightly below the specified maximum slope efficiency of 0.4 W/A, and a current tuning coefficient of 0.8 nm/mA, which is slightly above the target current tuning coefficient of 0.6 nm/mA. They also showed greater than 30 dB side-mode suppression ratios (SMSR) for optical powers of 0.2-0.5 mW. However, it was found that they had a mean divergence angle of 51.6 ± 0.8° which is more than twice the maximum allowed value of 25°. A small oxide aperture is required to ensure the higher order modes aren't guided by the aperture, so that the VCSEL emission is single-mode. However, this also reduces the beamwidth which increases the divergence angle due to to its inverse relationship (shown by equation 2.48). Simple oxide-confined VCSEL devices that have 30 dB single-mode operation with a divergence angle below 25° cannot be obtained on this epitaxial material. To increase the oxide aperture size, while still ensuring the emission is single-mode, changes to the epitaxial structure to reduce the guiding by the oxide aperture or the use of surface reliefs are required [17], although both approaches can increase the optical losses. There was also no strong mechanism to control the polarisation due to the circular symmetry, so there was a large variation in the measured orthogonal polarisation suppression ratio (OPSR) and the yield of polarisation stable VCSELs was low.

Elliptical oxide apertures, as a method to ensure the VCSEL polarisation was linear and stable, were also investigated. While surface gratings have been successfully applied to produce MAC VCSELs that are polarisation-stable with OPSRs of up to 21 dB [21], additional processing steps and electron-beam lithography are required. In this work, devices with 1.5×3.7 µm oxide aperture dimensions had measured SMSRs that were greater than 30 dB up to optical powers of 0.5 mW. The maximum OPSR varied between 13.6 ± 0.5 dB and 14.2 ± 0.5 dB, at optical powers between 0.2-0.5 mW. The minimum measured OPSR, over the same range of optical powers, differed from the maximum by less than 0.4 dB for all the measured devices (3 devices), and suggests this aperture dimension has good polarisation stability that's tolerant to fabrication variations. However, due to the coarseness in the range of elliptical oxide aperture

dimensions, an optimum dimension could not be determined. An OPSR that was greater than 15 dB was reported in [28], for a 2×2.5 µm rhomboidal oxide aperture, and suggests further improvement may be possible. When the oxide aperture dimensions were large enough so that the emission was multi-mode, despite higher aspect ratios, the OPSR was lower. This suggests elliptical oxide apertures can be effective as a method for polarisation control, but only when the VCSEL emission is single-mode.

The MAC application require VCSEL devices with an exact emission wavelength to interrogate the atomic transition. It was shown that a number of factors related to the oxide aperture dimension can affect the emission wavelength; self-heating will cause the internal temperature of the VCSEL to rise and cause a red-shift with current, while guiding by the oxide aperture will cause a blue-shift. Both these effects are more significant for small oxide aperture diameters, such as those required for single-mode emission. To properly compensate for these effects in the epitaxial structure, the operating current, temperature, and oxide aperture geometry must be specified beforehand.

Compared to edge-emitters, optical gain characterisation is not as straight-forward for VCSEL structures. For VCSELs with long cavities, the Hakki-Paoli method [32] has been applied in the vertical direction [33], while for more typical VCSEL structures, external efficiency measurements can give an indication of the optical losses within the device [34][35][36]. In-plane techniques have also been applied on VCSEL material, such as the fabrication of in-plane stripe lasers [41] or the Hakki-Paoli method in the in-plane direction [42]. Here, the optical gain profile was measured directly on VCSEL material, using an alternative in-plane technique known as the segmented contact method [89][90]. Lasing in the vertical direction was suppressed in the VCSEL structure by utilising reflections from the cap layer/metal contact interface, so that it destructively interfered with the DBR reflection. This allowed the optical gain to be characterised at current densities comparable to the threshold current density of the vertical lasing mode. The measured TE-polarised modal gain of the in-plane index guided mode was converted into a material gain by calculating the confinement factor

and effective index of the mode. Large diameter oxide aperture VCSEL devices were fabricated, using a quick fabrication process [107], on the same material. The threshold current density of these devices were measured, so that the threshold material gain could be determined by evaluating the material gain at the threshold current density and cavity resonance wavelength. A value of 1440 ± 140 cm^{-1} was obtained for this structure at 30 °C. The transfer matrix method, with doping induced absorption values from the literature, was used to calculate a threshold gain of 1010 cm^{-1}. This suggests the presence of a loss mechanism in addition to the doping induced absorption. One possibility is scattering losses due to interface roughening in the n-DBR layers. Agreement was found by increasing the optical loss in the n-DBR layers from 7 cm^{-1} to 40 cm^{-1}, which is consistent with previous work [111]. Understanding the gain requirement of the VCSEL epitaxial material means the active region can be designed to achieve a particular gain, for given operating conditions, so that the VCSEL device can operate more efficiently.

The gain spectrum was measured as a function of current density and temperature, and it was demonstrated how this information could be used to optimise the active layers for a particular operating condition. By plotting the peak material gain as a function of the gain-peak wavelength, and comparing to the threshold material gain and intended emission wavelength, for a 7 µm oxide aperture diameter VCSEL device, it was determined that a 5 nm blueshift in the active region PL peak would optimize the active layers for CW operation at 2 mA with a heat-sink temperature of 60 °C.

6.2 Future Work

To ensure the VCSEL devices can operate efficiently at the desired operating temperature close to 70 °C, changes to the epi-structure should be made so that the gain peak wavelength and the cavity resonance wavelength coincide at the intended operating temperature, at 894.6 nm. In addition, a small aperture diameter will cause the wavelength to blueshift due to guiding,

which will need to be compensated for in the epitaxial structure. Due to the strict wavelength requirement of the VCSEL device, this may mean that the epitaxial structure should be designed for a particular oxide aperture diameter.

The position of the oxide layer within the VCSEL epitaxial structure could be altered to reduce its overlap with the longitudinal mode profile. This would reduce the guiding by the oxide aperture, so that single-mode operation can be achieved with a larger aperture, while also reducing the wavelength sensitivity to the oxide aperture dimension, potentially improving the yield. It would also increase the mode width and lead to a decreased divergence angle. However, this may also reduce the transverse confinement factor and increase diffraction losses, which would increase the threshold current and reduce the optical output power. The reduced guiding may also mean the device is more sensitive to effects such as thermal lensing.

The use of sub-micron surface gratings could improve the yield of devices that have a high OPSR [21]. This could be used in conjunction with surface reliefs [22] to improve the single-mode performance of larger oxide aperture diameters devices, which have reduced divergence angles. Due to the higher optical powers that can be reached, it would be possible to increase the number of top mirror pairs to reduce the linewidth, while still meeting the optical output power requirements.

Due to the coarseness of the elliptical oxide aperture dimensions, their impact on the polarisation characteristics of the VCSEL could not be investigated thoroughly, and an optimum dimension could not be determined. For future investigations, the major diameter of the elliptical mesa should be increased in 1 µm steps, so that it doesn't lead to highly elliptical oxide apertures which won't meet the specification.

In-plane gain measurement techniques have previously been applied on VCSEL material, and to validate the gain measurements performed using the segmented contact technique, the results could be compared with these alternative methods. For example different length stripe lasers could be fabricated as in [41], and the peak-gain values determined from external

efficiency measurements. Due to current spreading by the highly doped DBR layers, a deep etched stripe was used to ensure only the region directly below the contacts were pumped. However, this can increase the non-radiative recombination. Ion implantion or oxidation of the high Al concentration AlGaAs layer, to define a stripe, could reduce the transverse current spreading. The former could also be used to increase the inter-contact resistance between segmented contact sections.

Bibliography

[1] London Economics, "Economic impact to the uk of a disruption to gnss," London Economics, Tech. Rep., 06 2017. [Online]. Available: https://londoneconomics.co.uk/blog/publication/economic-impact-uk-disruption-gnss/

[2] J. Kitching, "Chip-scale atomic devices," *Appl. Phys. Rev.*, vol. 5, no. 3, p. 031302, 2018.

[3] R. Wynands and S. Weyers, "Atomic fountain clocks," *Metrologia*, vol. 42, no. 3, p. S64, 2005.

[4] V. Shah and J. Kitching, *Chapter 2 - Advances in Coherent Population Trapping for Atomic Clocks*, ser. Advances In Atomic, Molecular, and Optical Physics, E. Arimondo, P. Berman, and C. Lin, Eds. Academic Press, 2010, vol. 59.

[5] T. P. Heavner, E. A. Donley, F. Levi, G. Costanzo, T. E. Parker, J. H. Shirley, N. Ashby, S. Barlow, and S. R. Jefferts, "First accuracy evaluation of NIST-F2," *Metrologia*, vol. 51, no. 3, p. 174, 2014.

[6] A. D. Ludlow, M. M. Boyd, J. Ye, E. Peik, and P. O. Schmidt, "Optical atomic clocks," *Rev. Mod. Phys.*, vol. 87, pp. 637–701, 2015.

[7] P. L. Bender, E. C. Beaty, and A. R. Chi, "Optical detection of narrow Rb^{87} hyperfine absorption lines," *Phys. Rev. Lett.*, vol. 1, pp. 311–313, 1958.

[8] E. Arimondo, "V coherent population trapping in laser spectroscopy," ser. Progress in Optics, E. Wolf, Ed. Elsevier, 1996, vol. 35, pp. 257–354.

[9] D. K. Serkland, G. M. Peake, K. M. Geib, R. Lutwak, R. M. Garvey, M. Varghese, and M. Mescher, "VCSELs for atomic clocks," in *Vertical-Cavity Surface-Emitting Lasers X*, vol. 6132. SPIE, 2006, p. 613208.

[10] J. Vanier, A. Godone, F. Levi, and S. Micalizio, "Atomic clocks based on coherent population trapping: basic theoretical models and frequency stability," in *Proceedings of the IEEE International Frequency Control Symposium*, 2003, pp. 2–15.

[11] M. Stähler, R. Wynands, S. Knappe, J. Kitching, L. Hollberg, A. Taichenachev, and V. Yudin, "Coherent population trapping resonances in thermal ^{87}Rb vapor: D1 versus D2 line excitation," *Opt. Lett.*, vol. 27, no. 16, pp. 1472–1474, 2002.

[12] M. Dummer, K. Johnson, S. Rothwell, K. Tatah, and M. Hibbs-Brenner, "The role of VCSELs in 3D sensing and LiDAR," in *Optical Interconnects XXI*, vol. 11692. SPIE, 2021, p. 116920C.

[13] A. Liu, P. Wolf, J. A. Lott, and D. Bimberg, "Vertical-cavity surface-emitting lasers for data communication and sensing," *Photon. Res.*, vol. 7, no. 2, pp. 121–136, 2019.

[14] Z. Khan, J.-C. Shih, R.-L. Chao, T.-L. Tsai, H.-C. Wang, G.-W. Fan, Y.-C. Lin, and J.-W. Shi, "High-brightness and high-speed vertical-cavity surface-emitting laser arrays," *Optica*, vol. 7, no. 4, pp. 267–275, 2020.

[15] M. Huang, D. K. Serkland, and J. Camparo, "A narrow-linewidth three-mirror VCSEL for atomic devices," *Appl. Phys. Lett.*, vol. 121, no. 11, 2022, 114002.

[16] D. K. Serkland, K. M. Geib, G. M. Peake, R. Lutwak, A. Rashed, M. Varghese, G. Tepolt, and M. Prouty, "VCSELs for atomic sensors," in *Vertical-Cavity Surface-Emitting Lasers XI*, vol. 6484. SPIE, 2007, p. 648406.

[17] A. Al-Samaneh, "VCSELs for Cesium-based miniaturized atomic clocks," Ph.D. dissertation, Ulm University, 2014.

[18] J. Zhang, X. Zhang, H. Zhu, J. Zhang, Y. Ning, L. Qin, and L. Wang, "High-temperature operating 894.6nm-VCSELs with extremely low threshold for Cs-based chip scale atomic clocks," *Opt. Express*, vol. 23, no. 11, pp. 14 763–14 773, 2015.

[19] S. Knappe, "3.18 - mems atomic clocks," in *Comprehensive Microsystems*, Y. B. Gianchandani, O. Tabata, and H. Zappe, Eds. Oxford: Elsevier, 2008, pp. 571–612.

[20] R. Michalzik, *VCSELs: Fundamentals, Technology and Applications of Vertical-Cavity Surface-Emitting Lasers*. Springer, 2012.

[21] M. J. Miah, A. Al-Samaneh, A. Kern, D. Wahl, P. Debernardi, and R. Michalzik, "Fabrication and characterization of low-threshold polarization-stable VCSELs for Cs-based miniaturized atomic clocks," *IEEE J. Sel. Top. Quantum Electron.*, vol. 19, no. 4, pp. 1 701 410–1 701 410, 2013.

[22] A. Al-Samaneh, M. Bou Sanayeh, M. J. Miah, W. Schwarz, D. Wahl, A. Kern, and R. Michalzik, "Polarization-stable vertical-cavity surface-emitting lasers with inverted grating relief for use in microscale atomic clocks," *Appl. Phys. Lett.*, vol. 101, no. 17, p. 171104, 2012.

[23] A. Al-Samaneh, M. Bou Sanayeh, S. Renz, D. Wahl, and R. Michalzik, "Polarization control and dynamic properties of vcsels for mems atomic clock applications," *IEEE Photon. Technol. Lett.*, vol. 23, no. 15, pp. 1049–1051, 2011.

[24] B. Weigl, M. Grabherr, C. Jung, R. Jager, G. Reiner, R. Michalzik, D. Sowada, and K. J. Ebeling, "High-performance oxide-confined gaas vcsels," *IEEE J. Sel. Top. Quantum Electron.*, vol. 3, no. 2, pp. 409–415, 1997.

[25] K.-H. Ha, Y.-H. Lee, H.-K. Shin, K.-H. Lee, and S.-M. Whang, "Polarisation anisotropy in asymmetric oxide aperture VCSELs," *Electron. Lett.*, vol. 34, pp. 1401–1402, 1998.

[26] G. P. Bava, P. Debernardi, and L. Fratta, "Three-dimensional model for vectorial fields in vertical-cavity surface-emitting lasers," *Phys. Rev. A*, vol. 63, p. 023816, 2001.

[27] L. Xiang, X. Zhang, J.-W. Zhang, Y.-Q. Ning, W. Hofmann, and L.-J. Wang, "Stable single-mode operation of 894.6 nm VCSEL at high temperatures for Cs atomic sensing," *Chin. Phys. B*, vol. 26, no. 7, p. 074209, 2017.

[28] S. A. Blokhin, N. A. Maleev, M. A. Bobrov, A. G. Kuz'menkov, A. P. Vasil'ev, Y. M. Zadiranov, M. M. Kulagina, A. A. Blokhin, Y. A. Guseva, A. M. Ospennikov, M. V. Petrenko, A. G. Gladyshev, A. Y. Egorov, I. I. Novikov, L. Y. Karachinsky, D. V. Denisov, and V. M. Ustinov, "Vertical-cavity surface-emitting lasers with intracavity contacts and a rhomboidal current aperture for compact atomic clocks," *Quantum Electron.*, vol. 49, no. 2, p. 187, 2019.

[29] W. Pang, G. Pan, Q. Wang, L. Hu, Z. Zhao, and Y. Xie, "894.6nm VCSEL for Cs-based atomic clocks with triangular holey structure," in *2020 3rd International Conference on Electron Device and Mechanical Engineering (ICEDME)*, 2020, pp. 573–575.

[30] Vixar Inc., *V00140*, 2022. [Online]. Available: https://vixarinc.com/wp-content/uploads/2021/05/V00140.pdf

[31] A. O. Makarov, S. M. Ignatovich, V. I. Vishnyakov, I. S. Mesenzova, D. V. Brazhnikov, N. L. Kvashnin, and M. N. Skvortsov, "Investigation of commercial 894.6 nm vertical-cavity surface-emitting lasers for applications in quantum metrology," *AIP Conf. Proc.*, vol. 2098, no. 1, p. 020010, 2019.

[32] B. W. Hakki and T. L. Paoli, "Gain spectra in GaAs double-heterostructure injection lasers," *J. Appl. Phys.*, vol. 46, no. 3, pp. 1299–1306, 1975.

[33] T.-C. Lu, J.-T. Chu, S.-W. Chen, B.-S. Cheng, H.-C. Kuo, and S.-C. Wang, "Lasing behavior, gain property, and strong coupling effects in GaN-based vertical-cavity surface-emitting lasers," *Jpn. J. Appl. Phys.*, vol. 47, no. 8S1, p. 6655, 2008.

[34] D. V. Kuksenkov, H. Temkin, and S. Swirhun, "Measurement of internal quantum efficiency and losses in vertical cavity surface emitting lasers," *Appl. Phys. Lett.*, vol. 66, no. 14, pp. 1720–1722, 1995.

[35] B. J. Thibeault, T. A. Strand, T. Wipiejewski, M. G. Peters, D. B. Young, S. W. Corzine, L. A. Coldren, and J. W. Scott, "Evaluating the effects of optical and carrier losses in etched-post vertical cavity lasers," *J. Appl. Phys.*, vol. 78, no. 10, pp. 5871–5875, 1995.

[36] D. I. Babic, J. Piprek, K. Streubel, R. P. Mirin, N. M. Margalit, D. E. Mars, J. E. Bowers, and E. L. Hu, "Design and analysis of double-fused 1.55-μm vertical-cavity lasers," *IEEE J. Quantum Electron.*, vol. 33, no. 8, pp. 1369–1383, 1997.

[37] M. R. Hofmann, N. Gerhardt, A. M. Wagner, C. Ellmers, F. Hohnsdorf, J. Koch, W. Stolz, S. W. Koch, W. W. Ruhle, J. Hader, J. V. Moloney, E. P. O'Reilly, B. Borchert, A. Y. Egorov, H. Riechert, H. C. Schneider, and W. W. Chow, "Emission dynamics and optical gain of 1.3-μm (GaIn)(NAs)/GaAs lasers," *IEEE J. Quantum Electron.*, vol. 38, no. 2, pp. 213–221, 2002.

[38] A. B. Ikyo, I. P. Marko, K. Hild, A. R. Adams, S. Arafin, M.-C. Amann, and S. S. J., "Temperature stable mid-infrared GaInAsSb/GaSb vertical cavity surface emitting lasers (VCSELs)," *Sci. Rep.*, vol. 6, p. 19595, 2016.

[39] K. I. Y. Motegi, H. Soda, "Surface-emitting GaInAsP/InP injection laser with short cavity length," *Electron. Lett.*, vol. 18, pp. 461–463, 1982.

[40] N. N. Ledentsov, V. A. Shchukin, V. P. Kalosha, N. N. Ledentsov, J.-R. Kropp, M. Agustin, Ł. Chorchos, G. Stepniak, J. P. Turkiewicz, and J.-W. Shi, "Anti-

waveguiding vertical-cavity surface-emitting laser at 850 nm: From concept to advances in high-speed data transmission," *Opt. Express*, vol. 26, no. 1, pp. 445–453, 2018.

[41] R. S. Geels, S. W. Corzine, and L. A. Coldren, "InGaAs vertical-cavity surface-emitting lasers," *IEEE J. Quantum Electron.*, vol. 27, no. 6, pp. 1359–1367, 1991.

[42] M. Kajita, T. Kawakami, M. Nido, A. Kimura, T. Yoshikawa, K. Kurihara, Y. Sugimoto, and K. Kasahara, "Temperature characteristics of a vertical-cavity surface-emitting laser with a broad-gain bandwidth," *IEEE J. Sel. Top. Quantum Electron.*, vol. 1, no. 2, pp. 654–660, 1995.

[43] L. A. Coldren, S. W. Corzine, and M. L. Mašanović, *Diode lasers and Photonic Integrated Circuits*, 2nd ed. New Jersey: John Wiley & Sons, Inc., 2012.

[44] P. Blood, *Quantum Confined Laser Devices*, 1st ed. Oxford: Oxford University Press, 2015.

[45] W. Shockley and W. T. Read, "Statistics of the recombinations of holes and electrons," *Phys. Rev.*, vol. 87, pp. 835–842, 1952.

[46] R. N. Hall, "Electron-hole recombination in germanium," *Phys. Rev.*, vol. 87, pp. 387–387, 1952.

[47] Y. G. Chai, R. Chow, and C. E. C. Wood, "The effect of growth conditions on Si incorporation in molecular beam epitaxial gaas," *Appl. Phys. Lett.*, vol. 39, no. 10, pp. 800–803, 1981.

[48] K. A. Bulashevich, V. F. Mymrin, S. Y. Karpov, D. M. Demidov, and A. L. Ter-Martirosyan, "Effect of free-carrier absorption on performance of 808 nm AlGaAs-based high-power laser diodes," *Semicond. Sci. Technol.*, vol. 22, no. 5, p. 502, 2007.

[49] W. G. Spitzer and J. M. Whelan, "Infrared absorption and electron effective mass in n-type gallium arsenide," *Phys. Rev.*, vol. 114, pp. 59–63, 1959.

[50] K. Kiyota, T. Kageyama, H. Shimizu, and Y. Kawakita, "Measurement of absorption coefficient of carbon-doped GaAs," *Jpn. J. Appl. Phys.*, vol. 48, no. 11R, p. 111103, 2009.

[51] R. Braunstein, "Intervalence band transitions in gallium arsenide," *J. Phys. Chem. Solids*, vol. 8, pp. 280–282, 1959.

[52] T. D. Visser, H. Blok, B. Demeulenaere, and D. Lenstra, "Confinement factors and gain in optical amplifiers," *IEEE J. Quantum Electron.*, vol. 33, no. 10, pp. 1763–1766, 1997.

[53] X. Gu, T. Shimada, and F. Koyama, "Giant and high-resolution beam steering using slow-light waveguide amplifier," *Opt. Express*, vol. 19, no. 23, pp. 22 675–22 683, 2011.

[54] J. Hayakawa, A. Murakami, D. Tominaga, Y. Suzuki, Z. Ho, X. Gu, and F. Koyama, "Watt-class high-power and high-beam-quality VCSEL amplifiers," in *Vertical-Cavity Surface-Emitting Lasers XXIII*, vol. 10938. SPIE, 2019, p. 1093809.

[55] C. Z. Ning, "Semiconductor nanolasers," *Phys. Status Solidi B*, vol. 247, no. 4, pp. 774–788, 2010.

[56] I. Melngailis, "Longitudinal injection-plasma laser of InSb," *Appl. Phys. Lett.*, vol. 6, no. 59, 1965.

[57] K. Iga, "Forty years of vertical-cavity surface-emitting laser: Invention and innovation," *Jpn. J. Appl. Phys.*, vol. 57, no. 8S2, p. 08PA01, 2018.

[58] M. Ogura, T. Hata, N. J. Kawai, and T. Yao, "GaAs/$Al_xGa_{1-x}As$ multilayer reflector for surface emitting laser diode," *Jpn. J. Appl. Phys.*, vol. 22, p. L112, 1983.

[59] R. S. Geels and L. A. Coldren, "Low threshold, high power, vertical-cavity surface-emitting lasers," *Electron. Lett.*, vol. 27, pp. 1984–1985, 1991.

[60] M. Sugimoto, H. Kosaka, K. Kurihara, I. Ogura, T. Numai, and K. Kasahara, "Very low threshold current density in vertical-cavity surface-emitting laser diodes with periodically doped distributed Bragg reflectors," *Electron. Lett.*, vol. 28, pp. 385–387, 1992.

[61] D. L. Huffaker, D. G. Deppe, K. Kumar, and T. J. Rogers, "Native-oxide defined ring contact for low threshold vertical-cavity lasers," *Appl. Phys. Lett.*, vol. 65, no. 1, pp. 97–99, 1994.

[62] K. D. Choquette, R. P. Schneider, K. L. Lear, and K. M. Geib, "Low threshold voltage vertical-cavity lasers fabricated by selective oxidation," *Electron. Lett.*, vol. 30, pp. 2043–2044, 1994.

[63] K. J. Ebeling and L. A. Coldren, "Analysis of multielement semiconductor lasers," *J. Appl. Phys.*, vol. 54, no. 6, pp. 2962–2969, 1983.

[64] J. D. Jackson, *Classical Electrodynamics*, 3rd ed. New Jersey: John Wiley & Sons, Inc., 1999.

[65] P. M. Smowton and P. Blood, "On the determination of internal optical mode loss of semiconductor lasers," *Appl. Phys. Lett.*, vol. 70, no. 18, pp. 2365–2367, 1997.

[66] P. Bienstman, R. Baets, J. Vukusic, A. Larsson, M. J. Noble, M. Brunner, K. Gulden, P. Debernardi, L. Fratta, G. Bava, H. Wenzel, B. Klein, O. Conradi, R. Pregla, S. A. Riyopoulos, J.-F. P. Seurin, and S. L. Chuang, "Comparison of optical vcsel models on the simulation of oxide-confined devices," *IEEE J. Quantum Electron.*, vol. 37, no. 12, pp. 1618–1631, 2001.

[67] G. R. Hadley, "Effective index model for vertical-cavity surface-emitting lasers," *Opt. Lett.*, vol. 20, no. 13, pp. 1483–1485, 1995.

[68] D. K. Serkland, G. R. Hadley, K. D. Choquette, K. M. Geib, and A. A. Allerman, "Modal frequencies of vertical-cavity lasers determined by an effective-index model," *Appl. Phys. Lett.*, vol. 77, no. 1, pp. 22–24, 2000.

[69] R. Sarzała, T. Czyszanowski, M. Wasiak, M. Dems, Ł. Piskorski, W. Nakwaski, and K. Panajotov, "Numerical self-consistent analysis of vcsels," *Adv. Opt. Technol.*, p. 689519, 2012.

[70] A. W. Snyder and W. R. Young, "Modes of optical waveguides," *J. Opt. Soc. Am.*, vol. 68, no. 3, pp. 297–309, 1978.

[71] C. Jung, R. Jäger, M. Grabherr, P. Schnitzer, R. Michalzik, B. Weigl, S. Müller, and K. J. Ebeling, "4.8 mW singlemode oxide confined top-surface emitting vertical-cavity laser diodes," *Electron. Lett.*, vol. 33, pp. 1790–1791, 1997.

[72] D. K. Serkland, G. A. Keeler, K. M. Geib, and G. M. Peake, "Narrow linewidth VCSELs for high-resolution spectroscopy," in *Vertical-Cavity Surface-Emitting Lasers XIII*, vol. 7229. SPIE, 2009, p. 722907.

[73] H. Martinsson, J. A. Vukusic, M. Grabberr, R. Michalzik, R. Jager, K. J. Ebeling, and A. Larsson, "Transverse mode selection in large-area oxide-confined vertical-cavity surface-emitting lasers using a shallow surface relief," *IEEE Photon. Technol. Lett.*, vol. 11, no. 12, pp. 1536–1538, 1999.

[74] H. J. Unold, S. W. Z. Mahmoud, R. Jager, M. Grabherr, R. Michalzik, and K. J. Ebeling, "Large-area single-mode VCSELs and the self-aligned surface relief," *IEEE J. Sel. Top. Quantum Electron.*, vol. 7, no. 2, pp. 386–392, 2001.

[75] E. Haglund, M. Jahed, J. S. Gustavsson, A. Larsson, J. Goyvaerts, R. Baets, G. Roelkens, M. Rensing, and P. O'Brien, "High-power single transverse and polarization mode VCSEL for silicon photonics integration," *Opt. Express*, vol. 27, no. 13, pp. 18 892–18 899, 2019.

[76] A. K. Jansen van Doorn, M. P. van Exter, and J. P. Woerdman, "Elasto-optic anisotropy and polarization orientation of vertical-cavity surface-emitting semiconductor lasers," *Appl. Phys. Lett.*, vol. 69, no. 8, pp. 1041–1043, 1996.

[77] C. J. Chang-Hasnain, J. P. Harbison, G. Hasnain, A. C. Von Lehmen, L. T. Florez, and N. G. Stoffel, "Dynamic, polarization, and transverse mode characteristics of vertical cavity surface emitting lasers," *IEEE J. Quantum Electron.*, vol. 27, no. 6, pp. 1402–1409, 1991.

[78] P. Debernardi, G. P. Bava, C. Degen, I. Fischer, and W. Elsasser, "Influence of anisotropies on transverse modes in oxide-confined VCSELs," *IEEE J. Quantum Electron.*, vol. 38, no. 1, pp. 73–84, 2002.

[79] K. D. Choquette and R. E. Leibenguth, "Control of vertical-cavity laser polarization with anisotropic transverse cavity geometries," *IEEE Photon. Technol. Lett.*, vol. 6, no. 1, pp. 40–42, 1994.

[80] D.-S. Song, Y.-J. Lee, H.-W. Choi, and Y.-H. Lee, "Polarization-controlled, single-transverse-mode, photonic-crystal, vertical-cavity, surface-emitting lasers," *Appl. Phys. Lett.*, vol. 82, no. 19, pp. 3182–3184, 2003.

[81] P. Debernardi, H. J. Unold, J. Maehnss, R. Michalzik, G. P. Bava, and K. J. Ebeling, "Single-mode, single-polarization VCSELs via elliptical surface etching:experiments and theory," *IEEE J. Sel. Top. Quantum Electron.*, vol. 9, no. 5, pp. 1394–1405, 2003.

[82] P. Debernardi and G. P. Bava, "Coupled mode theory: a powerful tool for analyzing complex vcsels and designing advanced device features," *IEEE J. Sel. Top. Quantum Electron.*, vol. 9, no. 3, pp. 905–917, 2003.

[83] P. Debernardi, J. M. Ostermann, M. Sondermann, T. Ackemann, G. P. Bava, and R. Michalzik, "Theoretical-experimental study of the vectorial modal properties of

polarization-stable multimode grating vcsels," *IEEE J. Sel. Top. Quantum Electron.*, vol. 13, no. 5, pp. 1340–1348, 2007.

[84] J. M. Ostermann, P. Debernardi, and R. Michalzik, "Optimized integrated surface grating design for polarization-stable VCSELs," *IEEE J. Quantum Electron.*, vol. 42, no. 7, pp. 690–698, 2006.

[85] Å. Haglund, S. J. Gustavsson, J. Vukušić, P. Jedrasik, and A. Larsson, "High-power fundamental-mode and polarisation stabilised VCSELs using sub-wavelength surface grating," *Electron. Lett.*, vol. 41, pp. 805–807, 2005.

[86] J. S. Gustavsson, Å. Haglund, J. A. Vukušić, J. Bengtsson, P. Jedrasik, and A. Larsson, "Efficient and individually controllable mechanisms for mode and polarization selection in VCSELs, based on a common, localized, sub-wavelength surface grating," *Opt. Express*, vol. 13, no. 17, pp. 6626–6634, 2005.

[87] A. E. Siegman, "Defining, measuring, and optimizing laser beam quality," in *Laser Resonators and Coherent Optics: Modeling, Technology, and Applications*, vol. 1868. SPIE, 1993, pp. 2 – 12.

[88] M. W. Sasnett and T. J. Johnston, "Beam characterization and measurement of propagation attributes," in *Laser Beam Diagnostics*, vol. 1414. SPIE, 1991, pp. 21 – 32.

[89] J. D. Thomson, H. D. Summers, P. J. Hulyer, P. M. Smowton, and P. Blood, "Determination of single-pass optical gain and internal loss using a multisection device," *Appl. Phys. Lett.*, vol. 75, no. 17, pp. 2527–2529, 1999.

[90] P. Blood, G. M. Lewis, P. M. Smowton, H. Summers, J. Thomson, and J. Lutti, "Characterization of semiconductor laser gain media by the segmented contact method," *IEEE J. Sel. Top. Quantum Electron.*, vol. 9, no. 5, pp. 1275–1282, 2003.

[91] S. Shutts, "Monolithic dual-wavelength InP/AlGaInP quantum dot lasers," Ph.D. dissertation, Cardiff University, 2012.

[92] J. Lutti, "Optical properties of InP/AlGaInP quantum dot laser heterostructures," Ph.D. dissertation, Cardiff University, 2005.

[93] C. Hentschel, C. P. Allford, S.-J. Gillgrass, J. Travers-Nabialek, R. Forrest, J. Baker, J. Meiklejohn, D. Powell, W. Meredith, M. Haji, J. I. Davies, S. Shutts, and P. M. Smowton, "Gain measurements on VCSEL material using segmented contact technique," *Journal of Physics D: Applied Physics*, vol. 56, no. 7, p. 074003, 2023.

[94] S. R. G. Hall and S. D. Knox, "Traceable measurements for beam propagation ratio M^2," *J. Phys. Conf. Ser.*, vol. 85, no. 1, p. 012014, 2007.

[95] N. Heermeier, M. Gebski, N. Haghighi, P. Moser, P.-S. Wong, M. Riaziat, and J. A. Lott, "Comparison of 850 nm VCSEL oxide aperture designs," in *Vertical-Cavity Surface-Emitting Lasers XXIV*, vol. 11300. SPIE, 2020, p. 113000J.

[96] G. Lafleur, G. Almuneau, A. Arnoult, H. Camon, and S. Calvez, "Anisotropy in the wet thermal oxidation of AlGaAs: influence of process parameters," *Opt. Mater. Express*, vol. 8, no. 7, pp. 1788–1795, 2018.

[97] A. C. Alonzo, X. C. Cheng, and T. C. McGill, "Effect of cylindrical geometry on the wet thermal oxidation of AlAs," *J. Appl. Phys.*, vol. 84, no. 12, pp. 6901–6905, 1998.

[98] S. Nabanja, L. Kolodziejski, and G. Petrich, "Lateral oxidation of AlAs for circular and inverted mesa saturable bragg reflectors," *IEEE J. Quantum Electron.*, vol. 49, no. 9, pp. 731–738, 2013.

[99] M. S. Alam, M. S. Rahman, M. R. Islam, A. G. Bhuiyan, and M. Yamada, "Refractive index, absorption coefficient, and photoelastic constant: Key parameters of InGaAs

material relevant to InGaAs-based device performance," in *2007 IEEE 19th International Conference on Indium Phosphide & Related Materials*, 2007, pp. 343–346.

[100] S. Gehrsitz, F. K. Reinhart, C. Gourgon, N. Herres, A. Vonlanthen, and H. Sigg, "The refractive index of $Al_xGa_{1-x}As$ below the band gap: Accurate determination and empirical modeling," *J. Appl. Phys.*, vol. 87, no. 11, pp. 7825–7837, 2000.

[101] P. B. Johnson and R. W. Christy, "Optical constants of transition metals: Ti, V, Cr, Mn, Fe, Co, Ni, and Pd," *Phys. Rev. B*, vol. 9, pp. 5056–5070, 1974.

[102] ——, "Optical constants of the noble metals," *Phys. Rev. B*, vol. 6, pp. 4370–4379, 1972.

[103] G. A. Smolyakov and M. Osinski, "Analysis of lateral-mode confinement in vcsels with ring metal apertures," *J. Light. Technol.*, vol. 23, no. 12, pp. 4278–4286, 2005.

[104] J. H. Weaver, M. Grioni, and J. Joyce, "Critical development stages for the reactive Cr-GaAs(110) interface," *Phys. Rev. B*, vol. 31, pp. 5348–5354, 1985.

[105] F. Xu, Z. Lin, D. M. Hill, and J. H. Weaver, "Temperature-dependent interface evolution for Ti/GaAs(100) and Cr/GaAs(100)," *Phys. Rev. B*, vol. 36, pp. 6624–6630, 1987.

[106] D. M. Hill, F. Xu, Z. Lin, and J. H. Weaver, "Atomic distributions across metal–III-V-compound-semiconductor interfaces," *Phys. Rev. B*, vol. 38, pp. 1893–1900, 1988.

[107] J. Baker, S. Gillgrass, C. P. Allford, T. Peach, C. Hentschel, T. Sweet, J. I. Davies, S. Shutts, and P. M. Smowton, "VCSEL quick fabrication for assessment of large diameter epitaxial wafers," *IEEE Photon. J.*, vol. 14, no. 3, pp. 1–10, 2022.

[108] N. Ashkenasy, M. Leibovitch, Y. Rosenwaks, and Y. Shapira, "Characterization of quantum well structures using surface photovoltage spectroscopy," *Mater. Sci. Eng. B*, vol. 74, no. 1, pp. 125–132, 2000.

[109] J. S. Liang, Y. S. Huang, C. W. Tien, Y. M. Chang, C. W. Chen, N. Y. Li, P. W. Li, and F. H. Pollak, "Surface photovoltage spectroscopy characterization of a GaAs/GaAlAs vertical-cavity-surface-emitting-laser structure: Angle dependence," *Appl. Phys. Lett.*, vol. 79, no. 20, pp. 3227–3229, 2001.

[110] Y. S. Huang, L. Malikova, F. H. Pollak, J.-P. Debray, R. Hoffman, A. Amtout, and R. A. Stall, "Surface photovoltage spectroscopy and normal-incidence reflectivity characterization of a 1.3 μm InGaAlAs/InP vertical-cavity surface-emitting laser structure," *J. Appl. Phys.*, vol. 91, no. 9, pp. 6203–6205, 2002.

[111] C. Asplund, S. Mogg, G. Plaine, F. Salomonsson, N. Chitica, and M. Hammar, "Doping-induced losses in AlAs/GaAs distributed Bragg reflectors," *J. Appl. Phys.*, vol. 90, no. 2, pp. 794–800, 2001.